Title

Automated Computation of Hemodynamic Metrics Based on Non-invasive Electrophysiological and Biomechanical Features

Author

Baek, Christopher Inhwan

Publication Date

2022

Peer reviewed|Thesis/dissertation

UNIVERSITY OF CALIFORNIA

Los Angeles

Automated Computation of Hemodynamic Metrics Based on Non-invasive Electrophysiological and Biomechanical Features

A dissertation submitted in partial satisfaction
of the requirements for the degree
Doctor of Philosophy in Electrical and Computer Engineering

by

Christopher Inhwan Baek

2022

ABSTRACT OF THE DISSERTATION

Automated Computation of Hemodynamic Metrics Based on Non-invasive Electrophysiological and Biomechanical Features

by

Christopher Inhwan Baek
Doctor of Philosophy in Electrical and Computer Engineering
University of California, Los Angeles, 2022
Professor William J. Kaiser, Chair

Heart failure (HF) is a serious condition wherein the heart is unable to supply sufficient amount of blood into circulation to meet the body's demand. It has been recognized as an emerging epidemic, and its prevalence is growing. Therefore, an immense need for innovative approaches to prevent and treat HF has emerged. It is estimated that about 50% of HF patients have impaired ventricular relaxation. A critical metric to assess this condition is pulmonary capillary wedge pressure (PCWP). Another critical pressure metric is pulmonary artery pressure (PAP), which can be used to assess the risk of HF and further adverse events in patients who already have HF. The gold standard method to measure PCWP and PAP is right heart catheterization (RHC) wherein a catheter is inserted into a patient's vein and advanced into the heart and artery to measure the pressure metrics. It is highly invasive and requires expertise, limiting its utility for routine monitoring of PCWP and PAP.

Our objective is to develop a system that meets the urgent and critical need for highly available routine pressure monitoring. To achieve this, the system needs to be safe, easy to use, and capable of accurate measurement of the pressure metrics. We have developed a system that combines cardiac signals simultaneously recorded with non-invasive wearable sensors from electrophysiological and biomechanical sources. The system includes a number of signal processing methods to extract features that correlate with the pressure metrics and

accurately computes these metrics via machine learning algorithms. Thus, the system does not require expertise to operate and acquire accurate pressure measurements.

The signal processing methods include heartbeat segmentation, noise suppression, and extraction of signal characteristics as features to train the machine learning algorithms. We have developed a novel hierarchical algorithm consisting of several regression models to accurately compute PCWP and PAP values. In addition to noise suppression, we have developed signal quality assurance methods to reject low quality signals in order to maintain accurate computation of PCWP and PAP.

The system has been validated via leave-one-out analysis with clinical trial data acquired from a diverse patient population. During the trial, RHC was performed to establish the ground truth, and our system was applied immediately before or after to record signals. Bland-Altman analysis on the predicted PCWP and the ground truth PCWP yields a bias of 0 and 95% limits of agreement of ± 4.76 mmHg. The same analysis on PAP yields a bias of 0 and 95% limits of agreement of ± 11.88 mmHg.

As a potential expansion of the system, systolic time intervals (STI) have been explored. STI have been widely studied as an indirect measurement of ejection fraction, which is another important metric to assess HF, and are measured as the time intervals between electrical and mechanical cardiac events: the onset of ventricular depolarization and the aortic valve opening and closure events. We have developed a flexible algorithm to detect the onset of ventricular depolarization in challenging electrocardiography signals with various morphologies and noise levels. We have also developed a method to detect a surrogate feature for the aortic valve opening in low-frequency phonocardiography signals. Combining the onset of ventricular depolarization, the surrogate feature, and the onset of second heart sound as the aortic valve closure, we have derived STI that have shown strong correlation with ejection fraction.

The dissertation of Christopher Inhwan Baek is approved.

Alex Anh-Tuan Bui

Robert N. Candler

Chih-Kong Ken Yang

William J. Kaiser, Committee Chair

University of California, Los Angeles

2022

This dissertation is dedicated to my wife, Ellen,

and my daughter, Elouise.

TABLE OF CONTENTS

LIST OF FIGURES

LIST OF TABLES

ACKNOWLEDGMENTS

I would like to first and foremost thank my advisor, Professor William Kaiser, for his incredible support and guidance throughout my graduate studies. I have been immensely inspired by not only his unfathomable knowledge and insights but also his amazing leadership.

I must also thank the members of my committee, Professor Alex Bui, Professor Robert Candler, and Professor Chih-Kong Ken Yang, for their insightful advice that will have a lasting impact on my future work as a researcher.

I would like to thank my colleagues. My special thanks go to Henrik Borgstrom, Peter Borgstrom, Kanav Saraf, Michael Wasko, Xu Zhang, and Yi Zheng. I have been extremely fortunate to work with such knowledgeable, passionate, and supportive researchers and engineers.

Last but not least, I would like to thank my family for their immense support. Without it, this dissertation would have not been possible.

VITA

2014	B.S. in Electrical Engineering, UCLA
2016	M.S. in Electrical Engineering, UCLA.
2015	Teaching Assistant, Department of Engineering, UCLA.
2015–2016	Teaching Assistant, Department of Electrical Engineering, UCLA.
2015–2017	Graduate Student Researcher, Wireless Health Institute, UCLA.

CHAPTER 1

Introduction

Heart failure (HF) is a serious condition wherein the heart is unable to supply sufficient amount of blood into circulation to meet the body's demand. HF has been recognized as an emerging epidemic, and its prevalence is still growing today [48]. The number of deaths caused by HF increased by 38% from 2011 to 2017 [101]. In the United States, HF was mentioned in over 13% of death certificates in 2018 [115], and its cost of care in 2020 was estimated at 43.6 billion dollars [55]. Therefore, an immense need for innovative approaches to prevent and treat HF has emerged.

Traditionally, HF was regarded as a result of inability to supply adequate blood during contraction [80]. A measurement of this is ejection fraction (EF), which is the percentage of blood ejected from the heart during each contraction, and reduced EF is a major indicator of HF. However, not every HF patient exhibits reduced EF, which results from systolic dysfunction. This type of HF is called HF with preserved EF (HFpEF) or diastolic HF where the heart does not effectively relax, leading to reduced filling and hence total amount of blood in the heart. Approximately 50% of HF patients are diagnosed with diastolic HF [10]. These patients show symptoms similar to those with HF with reduced EF (HFrEF) or systolic HF [50]. As a result, diastolic HF is difficult to distinguish from systolic HF without Doppler echocardiography or invasive measurements [80].

Diastolic HF is characterized by impaired ventricular compliance and relaxation due to stiffening of the left ventricle, leading to increased end-diastolic pressure [50]. At the end of the diastole, or relaxation, the pressure in the left ventricle, or left ventricular end-diastolic pressure (LVEDP), is roughly equal to the left atrial pressure (LAP). LAP can be measured

with a catheter that is inserted into the right atrium and then pierced through the septum into the left atrium. As this risky procedure incurs damage to the heart, direct measurement of LAP is not usually performed. Instead, the pulmonary capillary wedge pressure (PCWP) is measured as an indirect estimate of the LAP. PCWP is used for evaluating not only HF but also mitral valve stenosis and pulmonary hypertension.

The gold standard method for PCWP measurement is right heart catheterization (RHC). In this procedure, a balloon-tipped catheter named Swan-Ganz catheter is inserted into a femoral or jugular vein. Subsequently, the catheter is guided through the vein into the right atrium of the heart and then advanced into the right ventricle, pulmonary artery, and then finally a branch of the pulmonary artery where the balloon is inflated to wedge the branch for PCWP measurement.

Another important metric that is measured during RHC is pulmonary artery pressure (PAP). It is the primary indicator of pulmonary hypertension. In pulmonary hypertension, the heart needs to work harder to force blood flow into the lungs, weakening the cardiac muscles and thereby potentially leading to HF as a long-term effect. Furthermore, it has been suggested that elevated PAP is associated with an increased risk of adverse events for patients with HF [60].

RHC is an invasive procedure that requires an expert to perform. As such, its utility for routine pressure monitoring is limited, and it is primarily performed on end-stage HF patients [60]. However, routine monitoring is needed for a larger population of HF patients given the prevalence of pulmonary hypertension among HF patients and the increased risk of adverse events [60]. It has been also suggested that elevation in LVEDP, or indirectly PCWP, precedes HF events by 1-2 weeks [7]. Thus, a method for non-invasive and highly available monitoring of cardiac pressures is critically in need.

In this dissertation, we present a fully automated system that integrates non-invasive electrophysiological and biomechanical signals from wearable sensors to measure PCWP and mean PAP (mPAP). The non-invasive measurement of PCWP and mPAP via such a system enables highly safe routine monitoring of the pressures. Enabled by sophisticated

signal processing methods and machine learning algorithms, it does not require expertise to perform, making it highly available. Such safe and readily available routine PCWP and mPAP monitoring would have a significant impact on diagnosis and prognosis of HF and pulmonary hypertension.

The proposed system utilizes simultaneously acquired bio-signals from two different sources. On one hand, a recording of electrical signals from the heart called electrocardiography (ECG) is used to capture electrophysiological cardiac events such as depolarization and repolarization. The most prominent feature in ECG signals is the QRS complex that corresponds to the ventricular depolarization. The QRS complex repeats every cardiac cycle, providing reliable reference for heartbeat segmentation.

On the other hand, a set of acoustic signals are simultaneously recorded at spatially separated locations. The acoustic signals reflect biomechanical cardiac events, and examination of such signals, or cardiac auscultation, has been a diagnostic tool for many cardiac conditions. Recording of acoustic signals generated by the heart is called phonocardiography (PCG), which has enabled application of signal processing methods that had not been possible with traditional cardiac auscultation.

The system consists of a set of wearable sensors to record synchronous ECG and PCG signals and a patient monitor that computes the PCWP and mPAP based on the characteristics in the recorded signals. To achieve such computation, a number of signal processing methods have been developed to process the raw signals and extract a set of features that correlate with the pressure metrics. Machine learning algorithms have been developed and trained with the features extracted from a set of clinical trial data.

To enable development and validation of the system, clinical trials have been conducted. A diverse population of patients who exhibit various cardiac conditions has been recruited to acquire datasets that include various signal characteristics. RHC was performed on each patient to establish the ground truth for PCWP and PAP. The recording of ECG and PCG signals with our system was performed immediately before or after each RHC.

In order to properly extract information about the cardiac state, it is important to first

accurately identify cardiac events in the signals where the signal characteristics are analyzed to derive features. The initial step for this is to identify each heartbeat. This is achieved by detecting the QRS complexes in ECG signals. As described above, the QRS complex is a highly periodic feature that reflects the ventricular depolarization in each cardiac cycle.

Subsequently, the biomechanical events in PCG signals are analyzed. PCG signals reflect the biomechanical events as audible sounds including the heart sounds and, in certain unhealthy subjects, murmurs. We have investigated the characteristics of PCG signals during such events not only in the audible range, which has been the primary interest of the conventional PCG analysis, but also in the low-frequency range including the infrasonic components.

PCG signals are susceptible to noise from various sources. In order to accurately compute PCWP and mPAP, noise in PCG signals must be minimal. For this, noise reduction methods have been developed. We have observed that PCG signal quality varies in different frequency ranges. For the audible range, an existing noise subtraction method originally developed for speech signal enhancement is used. The low-frequency components of PCG signals have shown to be highly periodic. Thus, ensemble averaging of several per-beat segments is performed to retain periodic features while suppressing aperiodic noise-induced features. To perform accurate ensemble averaging, the per-beat segments must be precisely synchronized in time. In heart rate variability, per-beat segments have various durations, and thereby flexible time alignment must be performed to achieve precise synchronization.

PCWP and mPAP cannot be directly inferred from the processed PCG signals described above. Thus, features reflecting signal characteristics that correlate with PCWP and PAP must be used to compute the pressures. We have developed a set of features that are based on the amplitude, spectral characteristics, morphology, power, and harmonicity of PCG signals during different phases of the cardiac cycle.

We developed machine learning algorithms that utilize the PCG signal features to compute the PCWP and mPAP. The algorithm consists of hierarchical levels of multiple linear models for enhanced prediction accuracy. The upper-level model makes rough estimates of

the pressure metric covering the whole range of pressures. The rough estimates are used to classify each subject into one of three subranges each covering the low, mid, or high pressure range. The lower-level models provide more accurate prediction per subrange. Misclassification at the upper level may introduce a large error at the lower level. As such, an additional level named the bridge level is developed to mitigate misclassification by improving the prediction accuracy for subjects near the boundaries between subranges. The predicted PCWP and PAP values have been compared with those measured with the gold standard RHC. The predicted and gold standard values show high correlation.

As addressed above, PCG signals are susceptible to noise. In presence of high level of noise, the signal quality after application of the noise reduction methods may remain low. Thus, we have developed signal assurance methods. Just as the PCG signals, ECG signals are also susceptible to noise, and thus, an ECG signal quality assurance method was also developed. As for the ECG signal quality assurance, a set of features that correlate with the signal quality have been developed, and a support vector machine (SVM) classifier is trained to predict the signal quality. As for the PCG signal quality, we have developed two methods. Firstly, a set of features and an SVM-based classifier have been developed to predict the PCG signal quality in the audible range. Secondly, we have developed a metric that quantifies the periodicity of low-frequency PCG signals to assess their signal quality as high quality signals are characterized by high periodicity.

Our system has potentials for expansions as its synchronous ECG and PCG signals can be used for other applications. We have demonstrated effective detection of aortic stenosis using features in PCG signals recorded with our system [95]. In this dissertation, we present another potential application of our system to measure systolic time intervals (STI), which have been widely studied as a non-invasive measure of EF. STI consists of pre-ejection time (PEP) and left ventricle ejection time (LVET), which are defined as the time interval between the onset of ventricular depolarization and aortic valve opening and the time interval between the aortic valve opening and closure. To measure STI, we have developed a method to detect the onset of ventricular depolarization in diverse ECG signals [16]. The aortic valve closure

is estimated by the onset of the second heart sound during each cardiac cycle. The aortic valve opening, however, is considered difficult to detect in conventional PCG signals. We have investigated low-frequency PCG signals for a feature that could be used as a substitute for the aortic valve opening.

1.1 Prior Work

This section describes prior work on non-invasive measurement of PCWP and mPAP. The studied methods are based on echocardiography, which requires expensive equipment and a professionally trained sonographer. Thus, these methods do not meet our objective of developing a readily available non-invasive system for routine monitoring of PCWP and mPAP. However, it is valuable to review the prior studies on PCWP and mPAP measurement.

PCWP measurement via echocardiography is proposed in [81] wherein the relation of the ratio between transmitral inflow velocity and early diastolic velocity of the mitral annulus (E/e' ratio) to PCWP is investigated. In this study, the E/e' ratio is measured with Doppler tissue imaging (TDI) technique from N=60 subjects with RHC PCWP values. The measured E/e' ratio and the RHC PCWP values yield correlation, r, of 0.87. The difference between the estimated PCWP values using the E/e' ratio and the RHC PCWP values yields a bias of 0.1 mmHg and standard deviation of 3.8 mmHg.

In [22], a newer technique called speckle tracking echocardiography (STE) is investigated for estimation of PCWP. In this approach, peak atrial longitudinal strain (PALS) measured with STE has been suggested to correlate with PCWP. In this study, the PALS and RHC PCWP values are measured on N=36 subjects. The correlation between the PALS and RHC PCWP is observed to be -0.81. The Bland-Altman analysis [19] of the estimated PCWP values using the PALS and the RHC PCWP values yields a bias of 0.1 mmHg and 95% limits of agreements of -8.0 and 8.0 mmHg.

A different approach that uses STE for PCWP estimation is investigated in [63]. In this study, an index defined as $log_{10}\frac{\text{active left atrial ejection fraction}}{\text{minimum left atrial volume index}}$ is used to estimate PCWP.

The index and RHC PCWP are measured on N=58 subjects in mitral regurgitation. The correlation between the index and RHC PCWP is observed to be -0.68. The difference between the PCWP estimated by the index and the RHC PCWP yields a bias of 1.6 mmHg and standard deviation of 5.2 mmHg.

There have been proposed methods to measure mPAP with Doppler echocardiography. In [8], mPAP is estimated by adding right atrial pressure to the (right ventricular - right atrial) mean systolic gradient. This method has been evaluated with N=102 subjects. In the evaluation, the difference between the Doppler echocardiography mPAP and RHC mPAP yields a bias of -1.6 mmHg and standard deviation of 7.7 mmHg.

In [30], another mPAP measurement method via Doppler echocardiography has been evaluated. In such method, mPAP is computed as $0.6\text{sPAP} + 2$ where sPAP is systolic PAP measured by Doppler echocardiography. The method has been evaluated on N=152 subjects, yielding a bias of -0.5 mmHg and standard deviation of 9 mmHg when compared with RHC mPAP.

CHAPTER 2

Cardiac Anatomy and Physiology

The heart consists of four chambers: the left and right atria and the left and right ventricles as illustrated in Figure 2.1. The right atrium and ventricle form a pump called the right

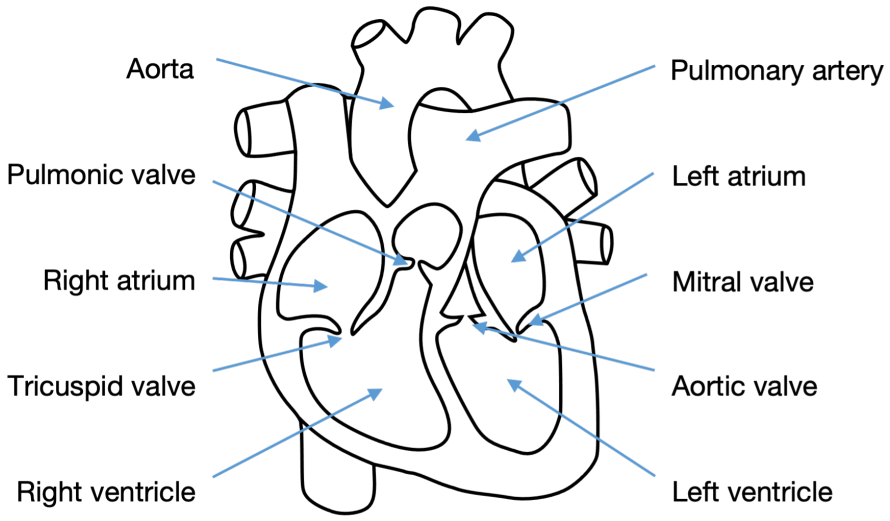

Figure 2.1: Cardiac anatomy

heart that receives deoxygenated blood from the body and pumps it to the lungs. Between these two chambers is the tricuspid valve, which controls the blood flow from the atrium to the ventricle. The right ventricle includes another valve called the pulmonic valve, which controls the blood flow from the ventricle to the lungs.

On the other side, the left atrium and the left ventricle form another pump called the left heart that receives oxygenated blood from the lungs and pumps it to the body. Similarly, the mitral valve between these chambers controls the blood flow from the atrium to the ventricle. The left ventricle also has another valve called the aortic valve, which controls the

blood flow from the ventricle to the body.

2.1 Cardiac Cycle

Deoxygenated blood from the body first enters the right atrium and then the right ventricle. The atrium contracts due to atrial depolarization and gives an extra push to fill the right ventricle with the blood. During this stage, the tricuspid valve is open while the pulmonic valve is closed. The atrial depolarization is followed by ventricular depolarization, which causes the ventricles to contract. Due to the contraction of the right ventricle, backflow of the blood in the ventricle towards the atrium causes the closure of the tricuspid valve. Pressure inside the right ventricle rises as it continues to contract, and the increased pressure causes the opening of the pulmonic valve. The phase between the tricuspid valve closure and pulmonic valve opening is called isovolumic contraction where the ventricular pressure rises while the volume inside the ventricle is constant.

The blood in the right ventricle is ejected to the lungs to be reoxygenated and then flows to the left atrium. The pulmonic valve closes at the end of the ejection as the ventricular pressure decreases. The ventricular pressure continues to decrease as the ventricle relaxes and eventually falls below the atrial pressure, leading to the opening of the tricuspid valve. The phase between the pulmonic valve closure and the tricuspid valve opening is called isovolumic relaxation where the ventricular pressure decreases while the volume is constant.

Subsequently, the blood fills the left heart to be pumped into the body. At the beginning of the next cardiac cycle, the contraction of the left atrium due to atrial depolarization further passes the reoxygenated blood to the left ventricle. During this stage, the mitral valve is open while the aortic valve is closed. The contraction of the left ventricle, due to the following ventricular depolarization, pushes the blood toward the atrium and closes the mitral valve as a result. The pressure in the left ventricle increases, leading to the opening of the aortic valve, through which the blood flows into the body. At the end of the ejection, the aortic valve closes as the ventricular pressure decreases. The ventricle relaxes and thereby

reducing the ventricular pressure and eventually leading to the opening of the mitral valve.

The contraction and relaxation of the left and right heart occur almost concurrently, with the left heart slightly preceding the right heart in normal individuals. The contraction phase is called systole. The atrial contraction phase is the atrial systole, and the ventricular contraction is the ventricular systole. In this dissertation, systole refers to the ventricular systole unless it is specified as atrial systole. At the beginning of systole, the rising ventricular pressure leads to the closure of both the mitral and tricuspid valves as described above. The relaxation phase is called diastole. This dissertation refers the ventricular diastole to as the diastole unless it is specified. At the beginning of diastole, the falling ventricular pressure leads to the closure of the aortic and pulmonic valves. These valve closures during the systole and diastole generate vibration that penetrates to the chest wall as an audible sound called the heart sound. These heart sounds include a large amount of information about the cardiac state. Therefore, examination of the heart sounds, or cardiac auscultation, enables diagnosis of several cardiac conditions.

The diastole can be divided into two sub-phases: the early diastole and late diastole. During the early diastole, the ventricles relax and cause blood flow from the atria to the ventricles. During the late diastole, the atria contract and provide what is called an atrial kick that pushes the blood from the atria to the ventricle. In summary, the blood flow from the atria to the ventricles occur during both the early and late diastole but by different mechanisms. From these, the stiffness of the ventricles referred to as diastolic dysfunction can be assessed.

CHAPTER 3

System Overview

The system, as shown in Figure 3.1, consists of multiple wearable sensors and a patient monitor with a Linux-based panel PC that hosts Python-based data acquisition, signal processing, and machine learning algorithms. The system simultaneously records data from

Figure 3.1: Hemodynamics monitoring system

multiple electrophysiological and biomechanical signal sources and computes the hemodynamic metrics in real time.

The sensors include three standard ECG sensor electrodes and four acoustic sensors. The ECG electrodes are connected to an ECG system that is installed inside the patient monitor. Several ECG lead systems are commonly used in hospitals such as the standard

12-lead system, 3-lead system, and 5-lead system [39]. Our system uses a single-channel 3-lead ECG system that is compact yet capable of capturing important electrophysiological events required for pressure metric computation. Following the Einthoven's triangle, the ECG electrodes are placed on the left side of the abdomen and the upper torso just below the left and right clavicles as shown in Figure 3.2a. The acquired data is the lead I channel data, which is the voltage difference between the left arm and the right arm electrodes.

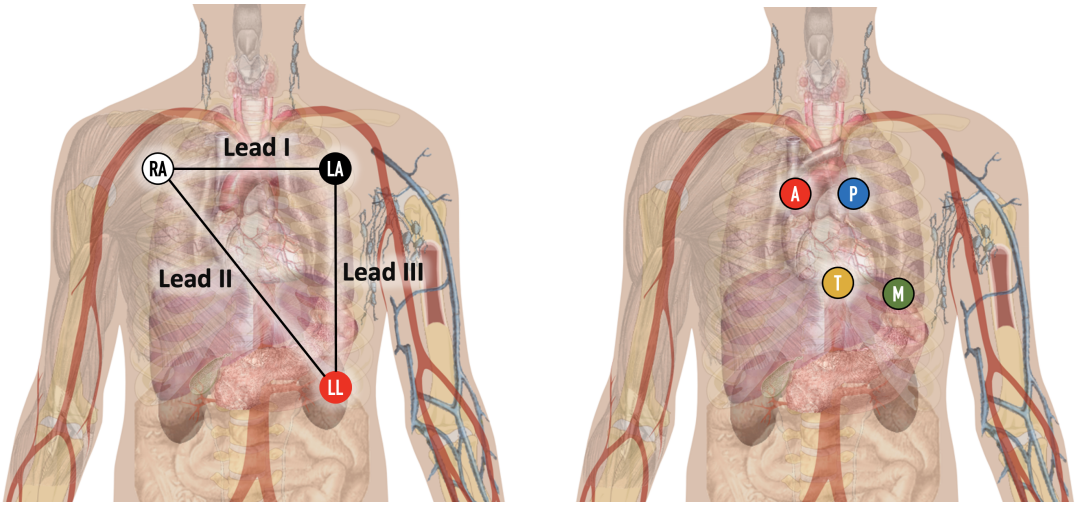

(a) ECG electrode placement (b) Auscultation sites

Figure 3.2: Sensor placement: ECG electrode placement (LA: left arm, RA: right arm, LL: left leg) and auscultation sites (A: aortic, P: pulmonic, T: tricuspid, and M: mitral)

The acoustic sensors are placed on the patient's chest at the standard four auscultation sites as shown in Figure 3.2b. Traditional auscultation involves a clinician examining the heart sounds and murmurs with a stethoscope. Instead, recording of these sounds with microphone transducers allows sophisticated signal processing methods and more consistent analysis. Furthermore, the acoustic sensors have been designed to capture broad frequency range of biomechanical signals including not only audible components that are consistent with heart sounds and murmurs but also infrasonic components that correspond to the low-frequency chest wall vibration induced by cardiac activities.

The acoustic sensors include a dome-shaped medical grade ABS plastic housing. On the

base of the dome is a medical grade nitrile membrane that couples with the patient's chest wall to capture its vibration. The housing has a small vent to allow airflow. The vibrating sensor membrane induces pressure changes inside the sensor, and such changes are transduced into electrical signals by an electret microphone inside the sensor. The cross-sectional view of the acoustic sensor is illustrated in Figure 3.3.

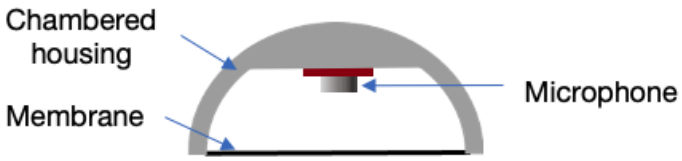

Figure 3.3: Cross-sectional view of acoustic sensors

A pair of elastic belts shown in Figure 3.4a are used to hold the acoustic sensors against the patient's skin to provide effective coupling. The belts are held together by a rigid bar with a semicircular indicator at its upper end to be placed at the suprasternal notch. The upper belt has two dots to indicate the aortic and pulmonic auscultation sites. The lower belt also has two dots to indicate the tricuspid and mitral sites. The sensors are placed between the patient's chest and the belts at the dot indicators. Figure 3.4b shows the sensors and the belts applied on a subject's torso.

The ECG electrodes and acoustic sensors are connected to the patient monitor that includes data acquisition modules. The PCG data acquisition module is built with a 4-channel analog-to-digital converter that simultaneously samples acoustic data from the four sensors at 512 Hz. As for the ECG data acquisition module, EG01000 from Medlab is used to sample the Lead I ECG signal at 300 Hz [1]. These modules transmit data to the Linux-based panel PC via RS-232 serial communication. In order to integrate ECG and PCG signals, accurate time synchronization of these signals is required. Firstly, the time offset between the ECG module and the PCG data module is measured. In order to find the time offset, synchronous square wave signals were applied to the data acquisition modules, and their step responses were analyzed. Once the time offset is removed, the ECG signal is resampled

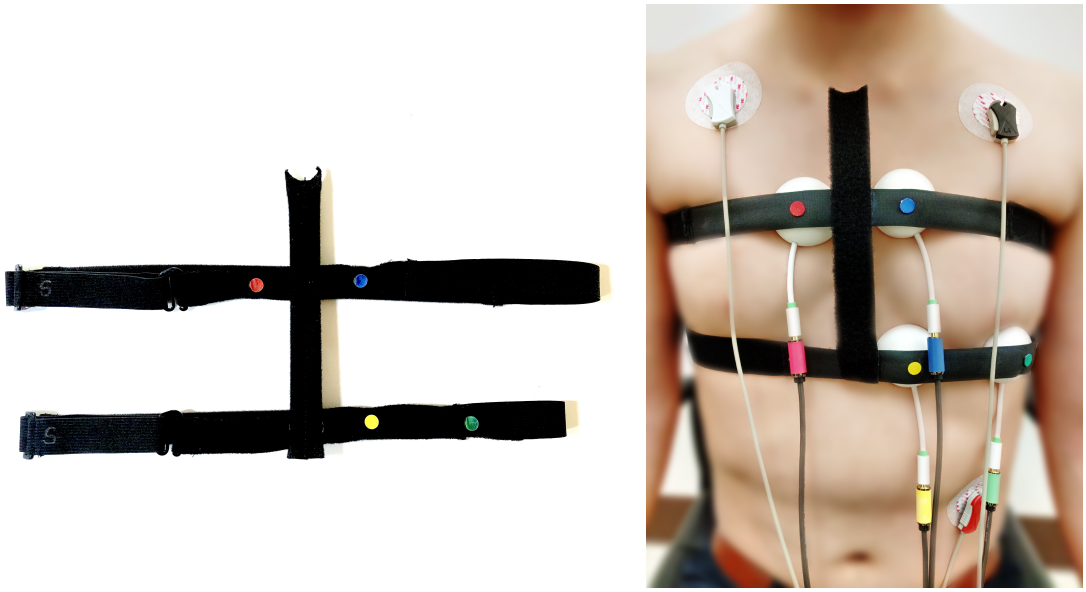

(a) Belt system for acoustic sensor application (b) Sensors and belts on torso

Figure 3.4: Sensor application

to 512 Hz to match the sampling rate of the PCG signals.

CHAPTER 4

Clinical Trials and Datasets

The development and validation of the hemodynamic monitoring system was enabled by data that had been acquired with trials conducted in real clinical environments at hospitals. During each trial session, the system was applied to a subject to record simultaneous ECG and PCG data following the protocol described in Section 4.1. During the same session, the gold standard method for hemodynamic assessment, RHC for the pressures or echocardiography for EF, was performed. The time elapsed between the ECG and PCG recording procedure and the gold standard procedure is minimized for consistency.

4.1 Trial Location, Subject Demographics, and Protocol

Two sets of clinical trials were conducted at two different locations: Oregon Hospital & Science University (OHSU) in Portland, Oregon and the Ronald Reagan Medical Center at the University of California Los Angeles (UCLA). At OHSU, RHC was performed to measure the pressures. The data from this set of trials has been used for the development of features for pressure metric computation. At UCLA, echocardiography was performed by expert sonographers to compute the ejection fraction. The data from this set of trials has been used for the development of the systolic time interval methods described in Chapter 10 and, in combination with the OHSU trial data, signal processing methods.

Both sets of trials include diverse population of subjects of both sexes with wide range of ages, weights, and heights. The PCWP values of the OHSU trial subjects as measured with RHC range from 4.5 to 35 mmHg. The mPAP values range from 13 to 62 mmHg. The EF values of the UCLA trial subjects as measured with echocardiography range from 20% to

80%. These subjects exhibit one or more cardiac conditions. The demographics information is summarized in the following table.

	OHSU	UCLA
# of subjects	68	110
Age	65 ± 15 years	57 ± 16 years
Sex	M: 43, F: 25	M: 77, F: 33
Weight	81 ± 17 kg	81 ± 19 kg
Average # of conditions	4	5
PCWP	15.8 ± 7.2 mmHg [4.5, 35]	N/A
mPAP	28.9 ± 12.2 mmHg, [13, 62]	N/A
EF	N/A	49 ± 11.7% [20, 80]

Table 4.1: Clinical trial demographics

The trial protocol is as follows. During a trial session at OHSU, the cardiac pressures including PCWP and PAP of a subject were measured with RHC. The measured metric values as well as the pressure waveforms are provided on a report. The ground truth for PCWP and PAP was derived from the pressure waveforms. The method for this is discussed in Section 4.2. During a trial session at UCLA, echocardiography was performed instead to measure the EF. ECG and PCG recording was proceeded immediately prior to or following the RHC or echocardiography procedure.

The steps for ECG and PCG recording during each trial session are as follows. The belt system for the sensor application is applied to the subject. Subsequently, the acoustic sensors are placed on the subject's chest under the belt system, matching the color-coded sensor location indicators. The acoustic sensors are lifted and released to ensure they are flush against the skin for good sensor coupling. Then, ECG electrodes are applied following the Einthoven's triangle. The cables are connected to the patient monitor and then to the sensors and electrodes. Since the cable movement may disturb the sensors and result in noise, the cables are secured to minimize their movement during the recording. The subject

is then positioned semi-supine and asked to remain still and silent throughout the remaining procedure. Once the system is applied and the subject is ready for recording, the patient monitor is powered on, and the signal quality is monitored. The sensors are adjusted if the signal quality is deficient. Then, a simultaneous recording of ECG and PCG signals is performed for 5 minutes.

4.2 Pressure Metrics Ground Truth Establishment

The RHC reports include pressure waveforms as well as computed pressure metric values. Such metrics include mean PCWP (mPCWP), A-wave PCWP, and V-wave PCWP for the PCWP assessment and mean PAP (mPAP), diastolic PAP (dPAP), and systolic PAP (sPAP) for the PAP assessment.

While the mean values are generally good approximation of the pressures, it is known that the mean pressure values become inaccurate in the presence of respiration because the intrathoracic pressure varies with respiration and affects the pulmonary pressures [67]. To minimize the respiration effect, it is recommended to measure PCWP and PAP at the end of expiration since the intrathoracic pressure is closest to the atmospheric pressure [26][91]. Figure 4.1 demonstrates the respiration effect on the pulmonary pressures. As demonstrated in the examples, PAP and PCWP decrease with inspiration. Thus, the mPAP and mPCWP values, that are computed by averaging of the pressure values, underestimate the pressures.

Under supervision of an expert, the pressure waveforms were carefully inspected to derive end-expiratory pressure values. For PAP, manual computation of end-expiratory value was not reliable. Thus, waveforms with substantial respiration effect were instead marked as unreliable and removed from the dataset, and the mPAPs of the remaining waveforms were used. On the other hand, the end-expiratory PCWP was acquired as the value of the PCWP waveform where the TP segment in the ECG signal and end-expiration indicated by the respiration trace overlap excluding the A and V waves.

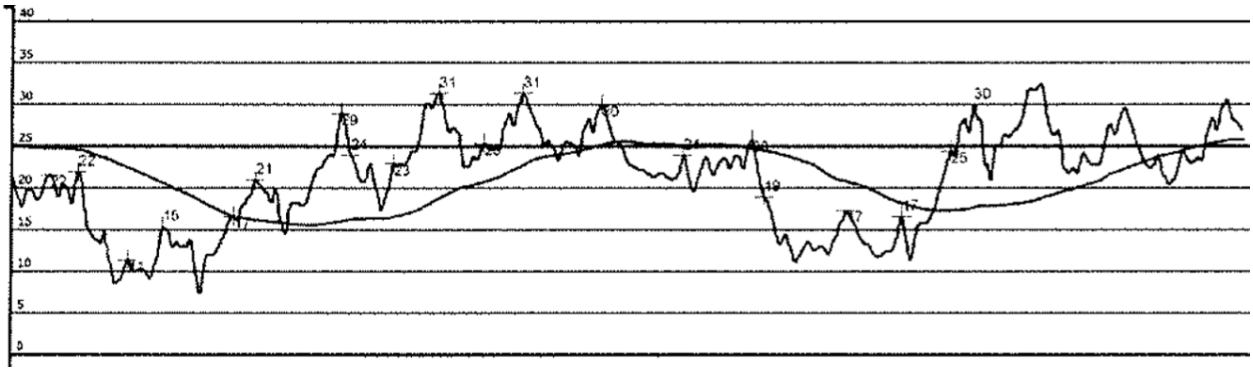

(a) PCWP waveform

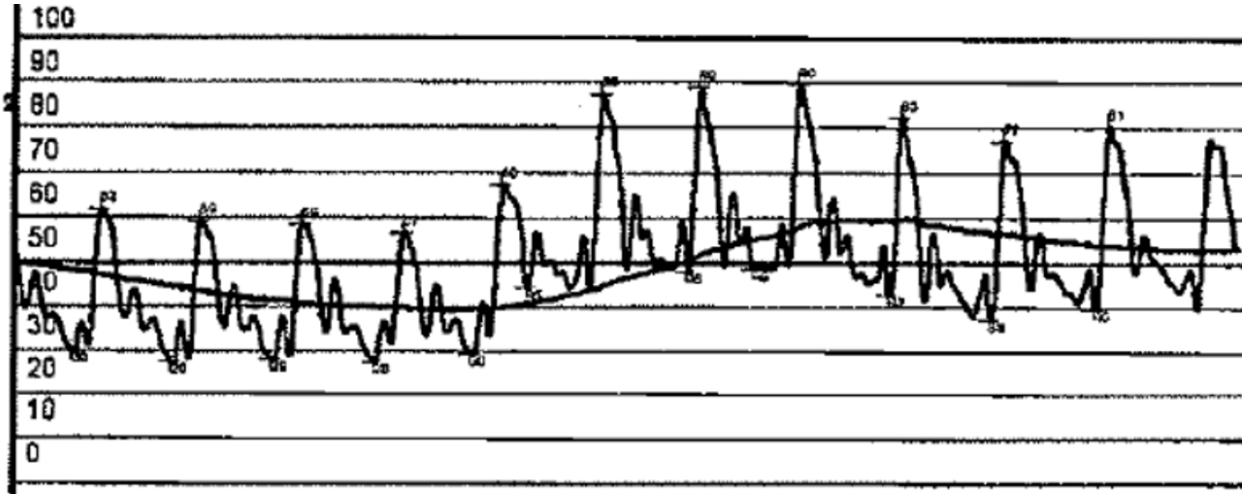

(b) PAP waveform

Figure 4.1: Pulmonary pressures in the presence of respiration effect. The smooth traces superimposed on the pressure waveforms represent the respiration. The end of expiration is at the peak or on the plateau of the respiration trace.

CHAPTER 5

Electrocardiography (ECG) Signal Processing

The PCWP and mPAP computation relies on synchronous ECG and PCG signals, which reflect cardiac events. It is important to identify such events where signal characteristics are analyzed for accurate computation of PCWP and PAP. The first step for this is to segment the signals into each cardiac cycle. In particular, electrophysiological events in ECG signals can be used to accurately partition the simultaneously acquired acoustic signals into segments each consisting of a single cardiac cycle, or simply hereinafter heartbeat segments. This chapter presents fully automated signal processing methods for the detection of such electrophysiological events and subsequent heartbeat segmentation.

ECG is recording of electrical activity of the heart by measuring the voltage across each pair of electrodes, which forms a lead. The voltage across a lead changes as a result of depolarization and repolarization of the cardiac muscles whose cells undergo changes in membrane potential. Such electrical cardiac events within each heartbeat segment are manifested in ECG signals as a series of deflections called waves as shown in Figure 5.1. The

Figure 5.1: ECG waveform during a cardiac cycle

P wave corresponds to atrial depolarization. The Q, R, and S waves altogether are known

as the QRS complex, which corresponds to ventricular depolarization. Lastly, the T wave corresponds to ventricular repolarization.

The most prominent feature in ECG signals is the QRS complex, which is often used as the reference feature in ECG. As such, reliable detection of the QRS complex is required for automated ECG signal analysis [38]. As a recurring event, the QRS complex can be also used to segment signals into individual heartbeats.

5.1 QRS Complex Detection

5.1.1 Introduction

Normally, the QRS complex is the most prominent in terms of the absolute amplitude. As such, it may seem feasible to simply detect the large positive wave as the R wave and the adjacent negative waves as the Q wave and the R wave. However, in clinical environment, ECG signals are often noisy and have various morphologies that are vastly different from a normal signal morphology from a healthy subject. For instance, the T wave in pathological signals can be significantly large in amplitude due to conditions such as hyperkalemia and ST-elevation myocardial infarction [103]. As a result, detection of the QRS complex becomes very challenging in real clinical ECG signals from afflicted subjects.

There has been ongoing research on accurate and robust QRS complex detection. Among several proposed methods is an approach where the derivative of the ECG signal is used to emphasize the QRS complexes [52][120][12]. The instantaneous rate of change during QRS complexes is generally much greater than those outside the QRS complexes. Thus, the derivative emphasizes the QRS complexes as they have high amplitudes.

Another popular approach for emphasizing the QRS complexes is based on the Shannon energy [75][126]. There have been proposed methods combining the derivative and Shannon energy approaches [75]. In such methods, the Shannon energy of the ECG signal's derivative is computed as the large amplitude of the resulting Shannon energy corresponds to the QRS complexes.

The prior studies utilized a widely used public ECG database called the MIT-BIH Arrhythmia Database [79]. Our method has been developed and validated with a larger dataset comprising the data acquired from the UCLA trials and the OHSU trials in addition to the MIT-BIH Arrhythmia Database. The dataset consists of a large number of highly noisy ECG signals with a variety of highly abnormal morphologies.

5.1.2 Methods

Inspired by the prior work, we have developed an automated QRS complex detection algorithm that operates by enhancing the QRS complex through a sequence of derivative and Shannon energy computations. In many cases, single computation of the Shannon energy of the signal's derivative as suggested by the prior studies is sufficient for accurate detection of the QRS complex. However, such approach can falsely detect a very tall T wave as a QRS complex.

In our algorithm, such computation is performed twice to further emphasize the QRS complex. Figure 5.2 is an example of an ECG signal with tall T waves where derivative, Shannon energy, and combination of these falsely indicate the T waves as QRS complexes. Subfigure 5.2a is the raw ECG signal where the amplitude of the T waves exceeds that of the QRS complexes. As a result, the derivative of the signal at the QRS complexes and that at the T waves have comparable amplitude, leading to failure to distinguish the QRS complexes from the T waves as shown in Subfigure 5.2b. Similarly, the Shannon energy is large for both the QRS complexes and the T waves as shown in Subfigure 5.2c. Since the derivative signal at the QRS complexes and the T waves are sharp with similar amplitudes, the Shannon energy of the derivative fails to distinguish them as shown in Subfigure 5.2d. Despite the similar amplitudes, the Shannon energy of the derivative has higher frequency characteristics at the QRS complex than it does at the T wave. Based on such observation, it can be inferred that another sequence of the derivative and the Shannon energy further emphasizes the QRS complexes. As shown in Subfigure 5.2e, the large amplitude of the resulting signal after the double computation accurately indicates the QRS complexes.

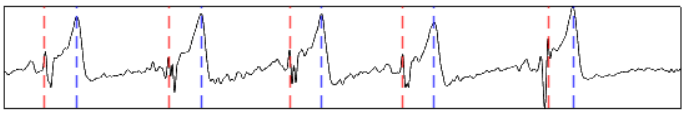

(a) Raw ECG signal

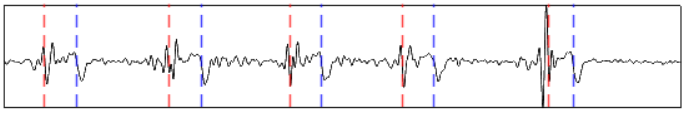

(b) Derivative of ECG signal

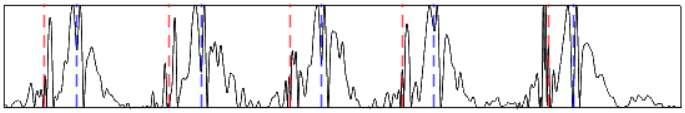

(c) Shannon energy of ECG signal

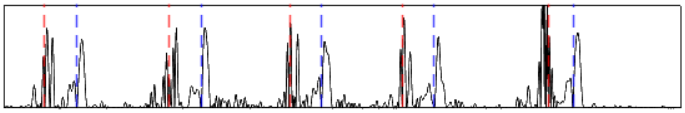

(d) Shannon energy of ECG signal's derivative

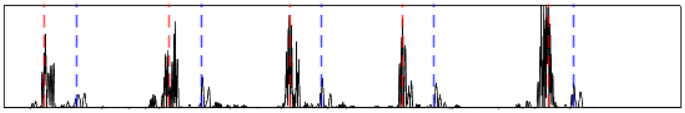

(e) Signal after double computation of derivative and Shannon energy

Figure 5.2: ECG derivative and Shannon energy. QRS complexes are marked by red vertical lines while T waves are marked by blue vertical lines.

The QRS complex detection is performed via steps illustrated in the block diagram in Figure 5.3. The first step is to filter the signal to remove potential noises. As ECG is a measurement of voltage difference between a pair of electrodes, it is susceptible to various types of electrical noises induced by motion, muscle activity, and powerline interference. Thus, the raw ECG signal must be filtered to remove potential noises before the following QRS complex emphasis is applied. A baseline wander is a commonly observed noise typically caused by respiration or other motion [44]. As the name suggests, it is a low frequency change of the ECG signal baseline. Muscle activities are measured as electromyographic (EMG)

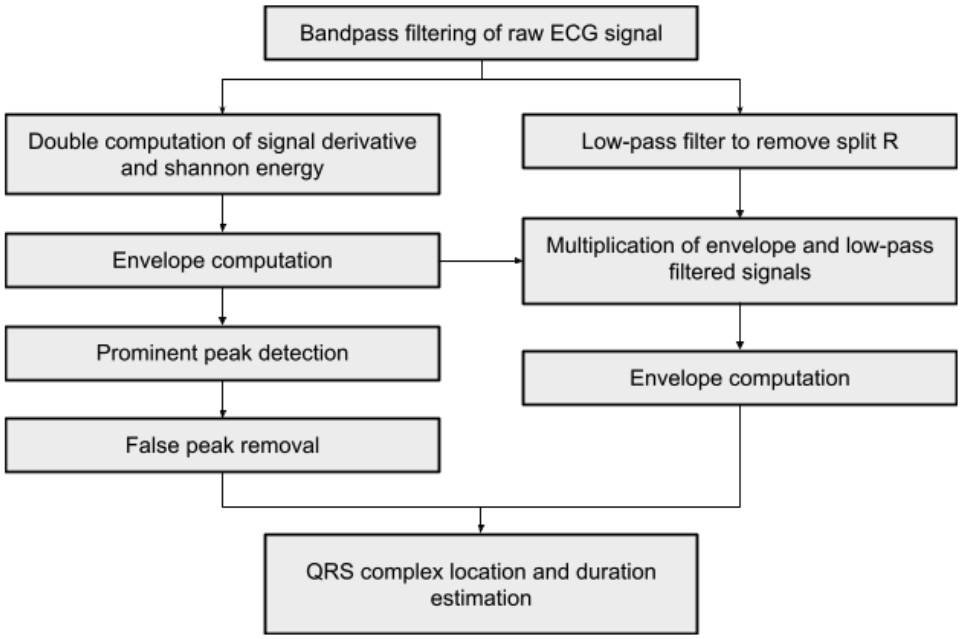

Figure 5.3: QRS complex detection algorithm block diagram

signals, which are often captured in ECG and vice versa. Powerline interference causes 50 Hz or 60 Hz sinusoidal noise in ECG signals. A zero-phase FIR bandpass filter with cut-off frequencies of 0.5 Hz and 40 Hz is applied to remove high frequency noises and baseline wander. Figure 5.4 shows examples where the filter effective removes baseline wander and high frequency noise due to powerline interference.

Then, the derivative of the bandpass-filtered signal is computed. Since the recorded ECG signal is discrete, first-order difference is computed instead as

$$d[n] = x[n+1] - x[n] \tag{5.1}$$

where $d[\cdot]$ is the derivative and $x[\cdot]$ is the bandpass-filtered ECG signal. Subsequently, the Shannon energy of the derivative is computed as

$$e[n] = \frac{d^2[n]}{\max_n d^2[n]} log(\frac{d^2[n]}{\max_n d^2[n]}) \tag{5.2}$$

where $e[\cdot]$ is the Shannon energy. For an atypical signal with prominent non-QRS peaks, such as the T waves in the provided example in Figure 5.2, these peaks may have elevated

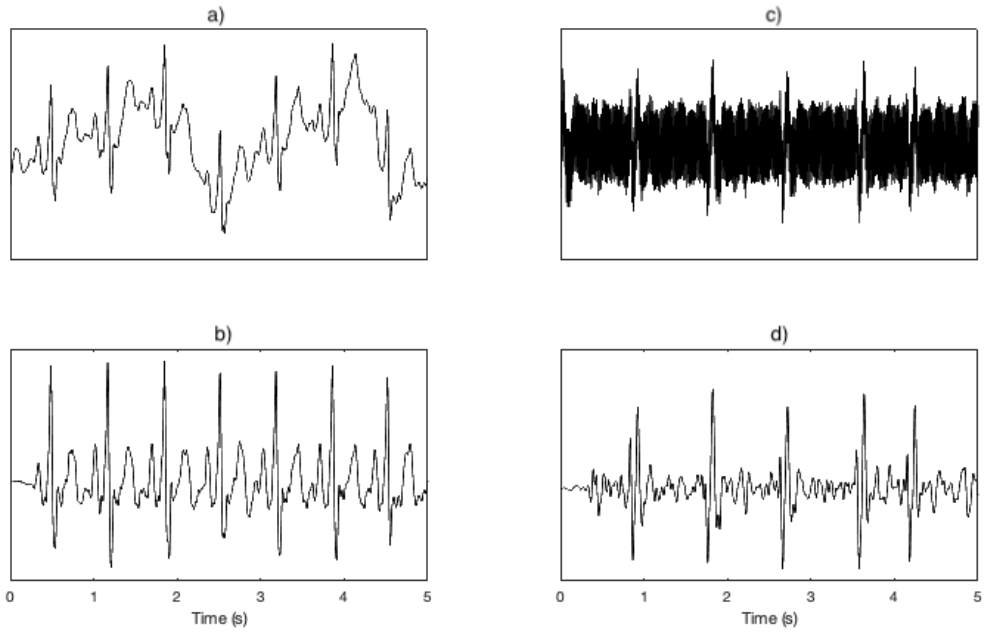

Figure 5.4: Noisy ECG signals and filtered signals. The left two plots are an example of baseline wander. The top plot a) shows a raw signal while the bottom plot b) shows the corresponding filtered signal. The right two plots are an example of signal filtering in powerline interference noise.

amplitude in the resulting Shannon energy and can be incorrectly identified as QRS complexes. In order to further emphasize the QRS complexes, another sequence of derivative and Shannon energy computation is applied to the resulting Shannon energy signal.

The envelope of the Shannon energy is computed for further processing of the ECG signal. Hilbert transform [40] is applied to the Shannon energy, and the absolute value of the resulting analytic signal is computed as the signal envelope. Then, the envelope is smoothed by filtering. The purpose of the smoothing is to merge a cluster of sharp peaks in the envelope signal into a single peak. A combination of a 51st-order 1-D median filter and a 6th-order Butterworth lowpass filter with cutoff frequency at 10 Hz is empirically selected for the filtering.

Each prominent peak in the smoothed envelope signal is likely to correspond to a QRS complex. In order to determine the prominent peaks, the amplitude of the smoothed envelope

signal is normalized. Then, a peak finding algorithm is used to detect peaks whose normalized amplitude exceeds 0.3. The threshold for the minimum amplitude of the detected peaks is set to be low enough to avoid false negatives as the amplitude of the peaks in the envelope can be occasionally reduced significantly by the smoothing. Such low threshold may allow many false positives. Thus, the amplitude of the normalized pre-smoothing Shannon energy in vicinity of each detected peak is used to remove false positives. If such amplitude is less than 0.6, the corresponding peak is removed. As an extra layer of false positive removal, a false peak detection method from [20] is used. In such method, peaks that are considerably larger or smaller than the median amplitude of the detected peaks are identified as false peaks due to sharp P or T waves or noise and thereby must be removed. Additionally, if two peaks are close to each other, the smaller one is considered to be a false peak and is therefore removed.

In addition to estimating the locations of the QRS complexes, our algorithm approximates their duration. To achieve this, the ECG signal is multiplied by the envelope to enhance the QRS complexes by suppressing the signal amplitude outside the QRS complexes. An envelope of this enhanced signal is obtained by computing the Hilbert transform and applying another combination of a median filter and a lowpass filter. For each prominent peak in the resulting envelope, its width and location are used to approximate the beginning and the end of the corresponding QRS complex. The width of the peak is determined as 1.3 multiplied by the distance between the upcrossing point and downcrossing point of the envelope at the half amplitude of the peak.

5.1.3 Results

The QRS detection method has been tested with a dataset comprising both the UCLA and OHSU trial data as well as the MIT-BIH Arrhythmia database. The method has demonstrated its effectiveness in both normal ECG signals and highly anomalous signals that are present in the diverse dataset. Figure 5.5 demonstrates the method in a generic ECG signal as an example. As shown in Subfigure 5.5a, the raw ECG signal has clear QRS complexes

and P and T waves. After bandpass filtering is applied, double computation of derivative and Shannon energy is performed to get the signal shown in Subfigure 5.5b. It is clearly shown that the resulting signal has significantly high amplitude during the segments where the QRS complexes are present in the raw ECG signal. Subfigure 5.5c shows the smoothed envelope of the resulting signal. The detected peaks marked by red circles indicate the estimated locations of the QRS complexes. In Subfigure 5.5d is the QRS-enhanced signal, which is acquired by multiplying the smoothed envelope and the filtered ECG signal. It is clearly shown that amplitude outside the QRS complexes is significantly suppressed. The width and location of each peak in the envelope of the QRS-enhanced signal determine approximate onset and end of each QRS complex as shown in Subfigure 5.5e.

The QRS detection method is also tested against ECG signals with abnormal waveform morphologies and high level of noise. In Subfigure 5.6a is an example of a signal with baseline wander. As indicated by the red vertical lines, the QRS complexes are accurately detected, and the onset and end of each detected QRS complex are well estimated. The following example as shown in Subfigure 5.6b is a signal with significant powerline interference noise. The next example shown in Subfigure 5.6c includes an irregular morphology pattern. The abnormally shaped QRS complex shown in the fifth heartbeat is caused by premature ventricular contraction (PVC), which occurs when a heartbeat is initiated by electrical pulses from the ventricles. A normal heartbeat is initiated by electrical pulses that are produced at the sinoatrial node and then travel from the atria to the ventricles. Such abnormal conduction leads to abnormal morphology as shown in the example. The method has shown to be effective in detecting this type of QRS complexes that are associated with PVC. The last example is a noisy ECG signal with tall T waves as shown in Subfigure 5.6d. In addition, the fourth heartbeat shows a notched R wave. The method accurately identifies all QRS complexes in this example.

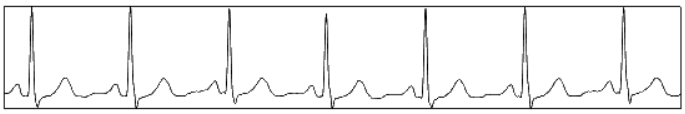

(a) Raw ECG signal

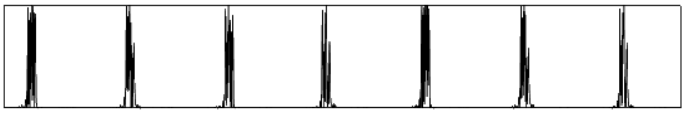

(b) Signal after double computation of derivative and Shannon energy

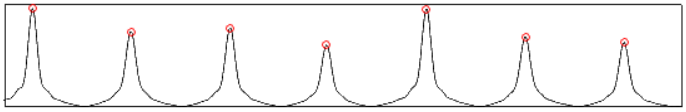

(c) Envelope of the signal shown in (b) and peaks marked by red circles

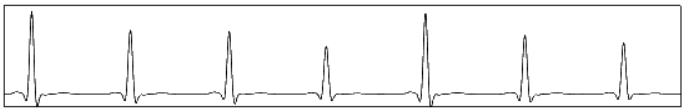

(d) QRS-enhanced signal

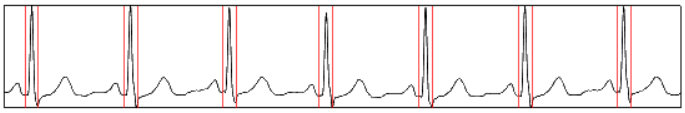

(e) Raw ECG signal with the onset and end of each detected QRS complex indicated by red vertical lines

Figure 5.5: Demonstration of QRS complex detection in a normal ECG signal

5.2 Heartbeat Segmentation

5.2.1 Introduction

As described above, the QRS complexes in ECG signals can be used to segment the signals into individual heartbeats. The estimated location of the QRS complexes as indicated by the Shannon energy envelope peak or the approximate onset of the QRS complex in the presented method above may provide sufficiently accurate reference for segmentation in many

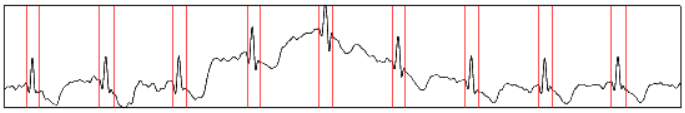

(a) ECG signal with baseline wander

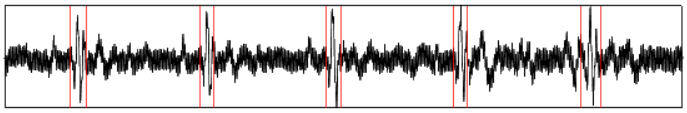

(b) Noisy ECG signal due to powerline interference

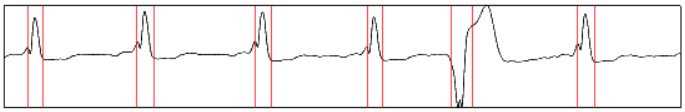

(c) ECG signal with PVC

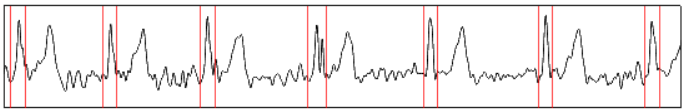

(d) Noisy ECG signal with tall T waves

Figure 5.6: QRS complex detection tested on challenging signals

applications. However, their relative timing is not sufficiently consistent to enable precise heartbeat segmentation that is required by the subsequent PCG signal processing methods described in the following chapter. This section presents a precise heartbeat segmentation method that expands the QRS detection method described above.

It may seem feasible to use R peaks as precise reference points. However, certain conditions may lead to various morphologies of the QRS complex and hence the R wave [69]. Furthermore, noise may distort the morphology, and even very slight distortion may potentially introduce a temporal shift of the R peak by a few milliseconds. In conclusion, R peaks cannot be used as reliable reference points for precise segmentation, and thus a more consistent feature is required as the reference point.

5.2.2 Methods

Several ECG signals with varying QRS complex morphology have been investigated. We have observed that the low-frequency components of signals below 10 Hz are significantly more repeatable than those above 10 Hz. Based on this finding, a precise heartbeat segmentation method has been developed as follows.

A baseline wander may significantly distort the signal morphology. Thus, a bandpass filter with cutoff frequencies at 0.5 Hz and 10 Hz is applied to raw ECG signals to extract the low-frequency components while removing a potential baseline wander. The resulting signals show strong periodicity, and the low-frequency components of QRS complexes remains as the most prominent features.

A highly repeatable feature within the QRS complex is detected as the reference point for segmentation. Using the QRS complex detection method described above, every QRS complex is detected, and within each QRS complex duration, the maximum absolute amplitude of the low-frequency signal is detected as the reference point. The absolute amplitude is considered due to a potential abnormal QRS complex that is characterized by suppressed R wave with deep Q and S waves, namely QS complex. In order to retain the whole QRS complex per segment, the signal is partitioned at 100 samples before each reference point detected from the low-frequency components.

5.2.3 Results

The method has been tested with the trial datasets and the MIT-BIH Arrhythmia database and demonstrated precise heartbeat segmentation in abnormal signals. Figure 5.7 shows an example of highly varying QRS complex morphology that demonstrates the effectiveness of the heartbeat segmentation based on the low-frequency components in comparison to heartbeat segmentation based on the R peaks. The plots on the left are heartbeat segments from a raw ECG signal with varying QRS complex morphology. The top five plots show individual heartbeat segments with the red dotted line indicating the detected R peak. As

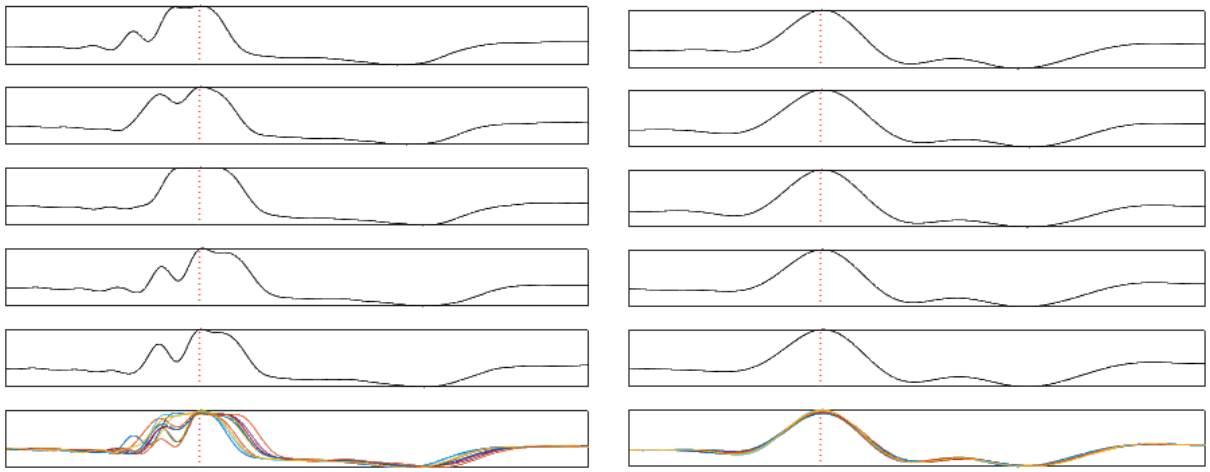

(a) Varying QRS complex morphology. The top five plots show individual heartbeat segments, and the bottom plot shows the superimposed segments.

(b) Low-frequency components of same ECG segments. The top five plots show individual heartbeat segments, and the bottom plot shows the superimposed segments.

Figure 5.7: ECG heartbeat segmentation

clearly shown, the locations of the Q waves and the inverted T waves are not consistent among the segments when synchronized with respect to the detected R peak locations. From this observation, it can be inferred that the R peaks as the reference points may not provide precise timing. The bottom plot shows superimposed segments that are time-synchronized using the R peaks. Such time-synchronization is not precise as indicated by the unmatching waveforms. On the other hand, the plots on the right are the waveforms of the low-frequency components of the identical ECG segments from the plots on the left. Here, the peak within the QRS complex is used as the reference point. According to the plot, these reference points provide accurate and precise timing. The superimposed segments shown in the bottom plot demonstrates that the low-frequency components are highly periodic and well-matching in time.

5.3 Summary

In this chapter, a robust QRS detection method and a precise heartbeat segmentation method are proposed. The proposed QRS detection method utilizes serial computation of the derivative and Shannon energy that are characterized by large amplitude during the QRS complex. The ECG signal is multiplied by the envelope of the signal after the serial computation. This multiplication enhances the QRS complexes while suppressing the P and T waves and other noisy deflections. From the resulting QRS-enhanced signal, the onset and the end of each QRS complex are estimated.

We have observed high periodicity of the low-frequency components of ECG signals. Based on this periodic characteristic, the maximum point of the low-frequency ECG signal within each QRS complex is detected and used for heartbeat segmentation. This approach demonstrates highly precise heartbeat segmentation in the presence of varying QRS complex morphology wherein commonly used heartbeat segmentation based on R peaks may result in inconsistent heartbeat segments.

CHAPTER 6

Phonocardiography (PCG) Signal Processing

6.1 Introduction

Cardiac auscultation has been a critical examination for diagnosis of many cardiac conditions. Traditional cardiac auscultation involves a physician examining heart sounds and murmurs with a stethoscope to identify characteristics that are associated with physiology. It has been addressed that the information acquired via auscultation is often subjective and difficult to be duplicated by different examiners [109]. Phonocardiography, a technique of recording cardiac sounds with a microphone, has emerged and enabled more objective and consistent heart sound analysis. Furthermore, digital PCG has opened possibilities for application of sophisticated signal processing methods for further interpretation [109][6].

A typical PCG signal is illustrated in Figure 6.1, in which heart sounds from two heartbeats are shown. In healthy adults, PCG signals have two heart sounds, namely the first

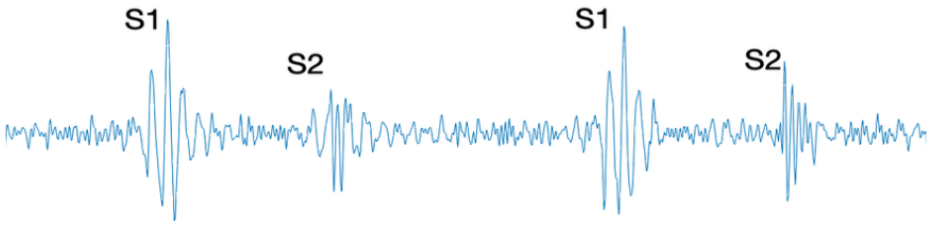

Figure 6.1: Heart sounds in PCG signal

heart sound (S1) and second heart sound (S2), per heartbeat. The S1 is generated by the closure of the mitral and tricuspid valves as the ventricles start to contract. The S2 is generated by the closure of the aortic and pulmonic valves when the ventricular pressure decreases

and falls below the atrial pressure. In unhealthy adults, extra heart sounds, S3 and S4, or murmurs may be observed. The murmurs are produced by turbulent blood flow possibly caused by valve disorders that is strong enough to be audible.

The acoustic properties of these heart sounds and murmurs include valuable information about physiology and cardiac conditions. As such, analysis of the heart sounds and murmurs in PCG signals has been proposed for diagnosis of several cardiac diseases. [116], [110], and [95] have presented signal processing methods on PCG for diagnosis of aortic stenosis. [17] has presented an artificial neural network approach to diagnose other cardiac valve disorders including mitral regurgitation, mitral valve prolapse, and mitral stenosis.

In the prior studies on PCG-based diagnosis and analysis, audible heart sounds and murmurs have been primary interest. However, in a broad sense, PCG signals may also include infrasonic components that correspond to the low-frequency precordial vibrations [90][74]. The traditional definition of PCG as recording of heart sounds and murmurs not only fails to accurately reflect all aspects of PCG but also limits its potentials to audible sounds. To reflect the broad frequency range of PCG, the traditional definition is gradually being replaced by a new definition: recording of complex waves representing chest wall vibration [6]. Our acoustic sensors are capable of capturing broad frequency range of signals. The broad frequency range can be divided into the audible range and the infrasonic range for comprehensive analysis of biomechanical events from both sonic and low-frequency vibratory standpoints.

In this chapter, we describe signal processing methods for both audible and low-frequency components. In Section 6.2, multiple frequency bands of PCG signals are analyzed to demonstrate the characteristics of audible and low-frequency components. Furthermore, the potentials of these components are discussed. In Section 6.3, a popular technique for bio-signal analysis called the wavelet transform is described, and its applications for PCG signals are demonstrated. Section 6.4 present noise suppression methods for PCG signals.

6.2 Multi-frequency Band Analysis

6.2.1 PCG Signal in Various Frequency Bands

As described above, PCG signals include not only audible components which have been primary interest of the conventional PCG analysis but also low-frequency components that are associated with the low-frequency precordial vibrations. Thus, we investigate both the conventional audible range and low-frequency range of PCG signals for features that correlate with the hemodynamics. In this section, the PCG signals acquired by our acoustic sensors are analyzed in different frequency bands.

In order to determine the feasibility of extracting information from certain frequency bands in our PCG signal, it is important to assess the presence of different frequency components. For this, the power spectral densities (PSD) of several PCG signals have been analyzed. Figure 6.2 shows periodograms of clean PCG signals recorded at the four auscultation sites. The signal power is the largest in the low frequency range and gradually

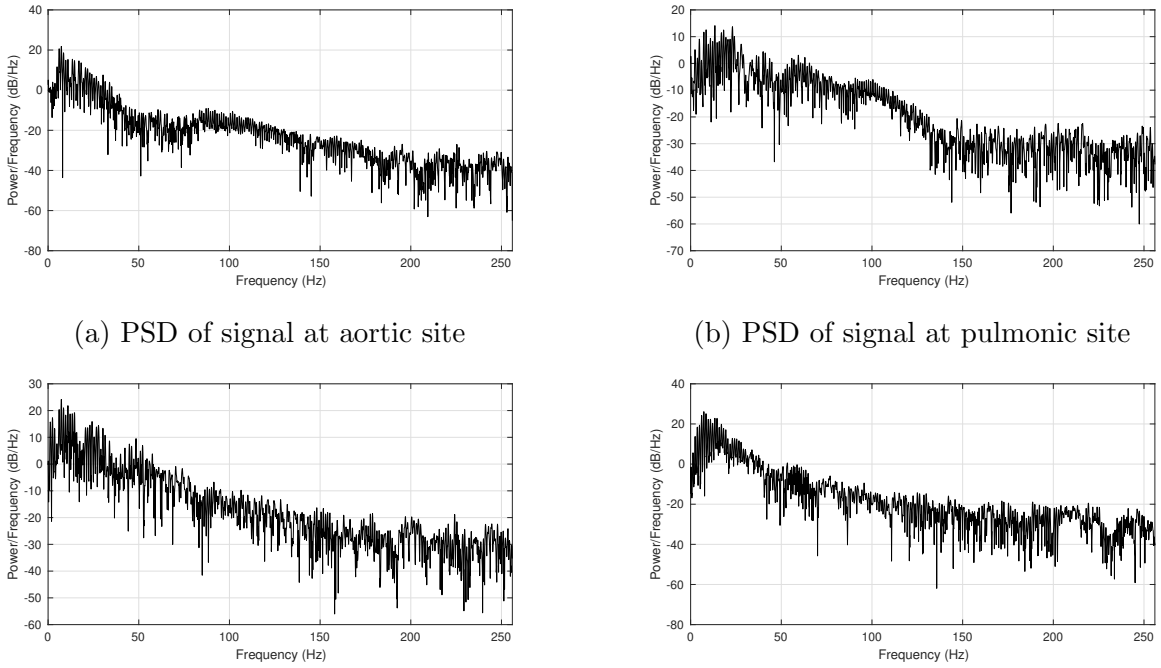

(a) PSD of signal at aortic site

(b) PSD of signal at pulmonic site

(c) PSD of signal at tricuspid site

(d) PSD of signal at mitral site

Figure 6.2: Periodogram of a clean PCG signal

attenuated as the frequency increases. Since the low-frequency range has significant power, this range is investigated further.

Let us first investigate the waveforms of PCG signals in different frequency bands. Figure 6.3 demonstrates four different frequency bands of a PCG signal. The ultra low frequency

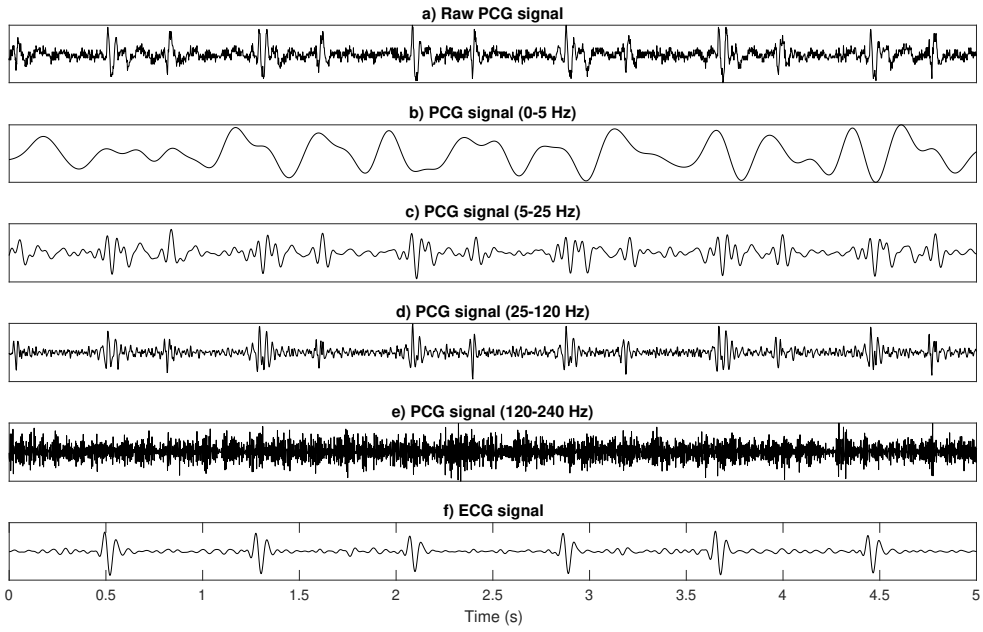

Figure 6.3: PCG signal waveforms in different frequency bands

band between 0 Hz and 5 Hz exhibits slightly periodic pattern with two large peaks recurring every heartbeat. The low frequency band between 5 Hz and 25 Hz clearly exhibits highly periodic pattern. The frequency band between 25 Hz and 120 Hz exhibits conventional PCG morphology with clear S1 and S2. The lower frequency components of this band are slightly periodic. The frequency band between 120 Hz and 240 Hz do not exhibit any periodic pattern. Moreover, the PSDs of our PCG signals indicate that the power in this band is substantially reduced in comparison to the lower frequency bands. Although this frequency band is a good area of recording with many other apparatuses for PCG [6], we will exclude this band from further investigation.

After analyzing the PCG signals from the UCLA and OHSU trial datasets, two frequency

bands have been empirically selected for the low frequency PCG analysis and conventional audible PCG analysis. Audible PCG signals are acquired by applying a bandpass filter with cutoff frequencies of 25 Hz and 100 Hz. For the low frequency analysis, the frequency band between 1 Hz and 45 Hz is selected. The frequency band below 1 Hz is excluded since it includes respiration. Based on observation, the PCG signal components roughly up to 45 Hz have shown highly periodic pattern. In order to demonstrate such periodicity, per-beat segments of a PCG signal are superimposed as shown in the examples in Figure 6.4. Such

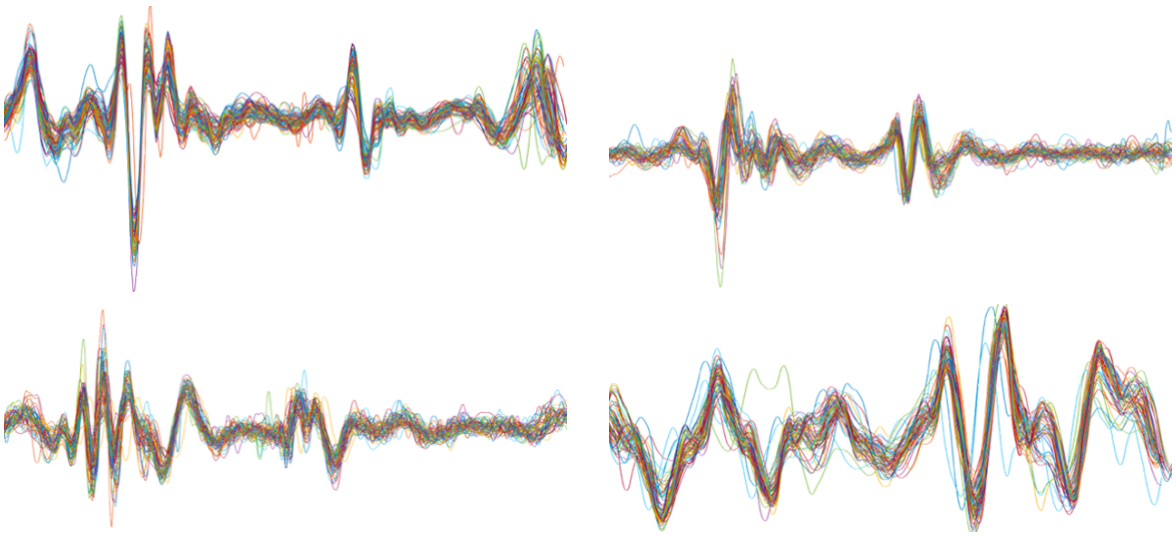

Figure 6.4: Highly periodic low-frequency PCG signals

periodicity indicates that the low-frequency PCG signal correspond to cardiac events rather than other non-cardiac motion. While we do not understand the origin of the low-frequency features, we hypothesize that there may be important information about cardiac activities in this frequency band that may correlate with hemodynamics.

6.2.2 Comparison with Seismocardiography

A popular noninvasive technique called seismocardiography (SCG) has been widely studied to analyze chest wall motions induced by cardiac activities. In this technique, an accelerometer is placed on a patient's thorax, most commonly sternum, to measure the acceleration of the chest wall motions. SCG was first introduced and popularized in clinical medicine in the early

90's [122][25]. Since then, its clinical potentials have been widely studied. In [121] and [29], simultaneous SCG and echocardiography recordings were analyzed to study the correlation between features in SCG signals and cardiac events observed in echocardiography. It is now well-known that SCG signals contain points that correspond to cardiac events. Figure 6.5 illustrates a typical SCG signal at the sternum with annotation of the cardiac events. SCG

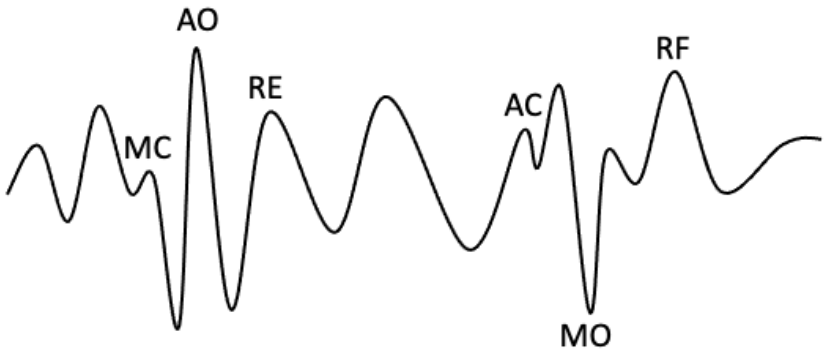

Figure 6.5: SCG signal with feature points that correspond to cardiac events: mitral valve closure (MC), aortic valve opening (AO), rapid ventricular ejection (RE), aortic valve closure (AC), mitral valve opening (MO), and rapid ventricular filling (RF)

has been proposed for assessment of myocardial contractility and hemodynamics [108][107]. Drawing inspirations from the prior work on SCG, we will further investigate and analyze the low-frequency PCG for hemodynamics assessment.

Although low-frequency PCG is not claimed to be identical to SCG, it is valuable to compare them and investigate whether low-frequency PCG includes any characteristics that are similar to those in SCG. An experiment was conducted to compare simultaneously recorded PCG and SCG signals from four subjects. For the acquisition of SCG signals, we have developed a wireless sensor device that can be attached to the belt system and stacked with the acoustic sensor as shown in Figure 6.6. The SCG sensor device consists of a computing module [3], an inertial measurement unit (IMU) [4], and a battery. A custom embedded Linux operating system and data acquisition software is installed on the computing module. Four SCG sensor devices are placed on the four acoustic sensors to record the low-frequency

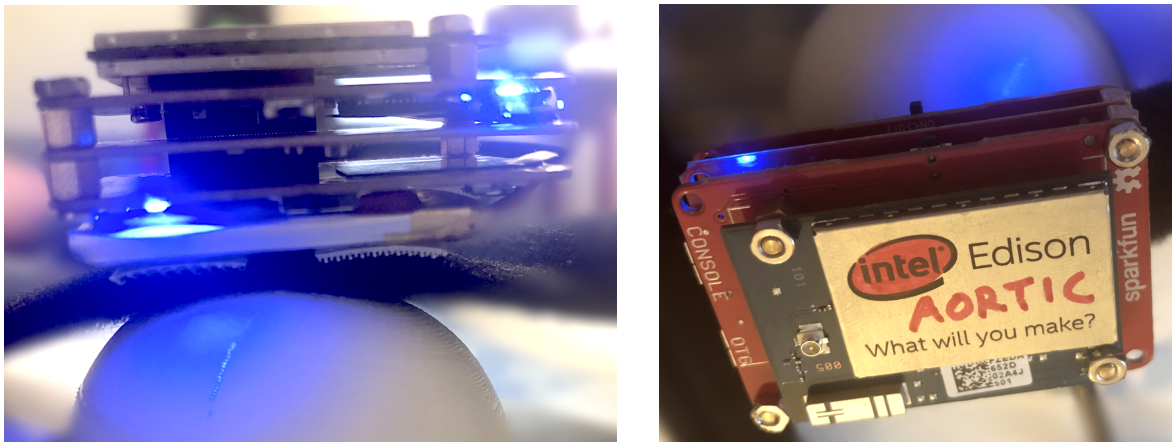

Figure 6.6: Stacked acoustic and SCG sensors

acceleration and PCG at each auscultation site. The patient monitor is configured as an access point, which the SCG sensor devices are connected to via Wi-Fi. These devices are time-synchronized using Network Time Protocol [78].

The simultaneously recorded acoustic and accelerometer signals are filtered with a lowpass filter. The resulting low-frequency PCG and SCG exhibit similar waveform morphology as shown in Figure 6.7.

6.3 Wavelet Analysis

Wavelets have been widely used in many signal processing applications. As the name suggests, a wavelet is a short wave or oscillation with its amplitude grows from zero and then attenuates to zero. A wavelet is shifted to describe the temporal information and scaled to describe the spectral information. A signal can be represented by a set of shifted and scaled wavelets that describe the temporal and spectral information of the signal.

Wavelets are often compared with sinusoids of Fourier analysis in which the sinusoids are only scaled and combined. For this reason, the wavelet transform has a critical advantage that it describes both the temporal and spectral information while Fourier transform only describes the spectral information. The wavelet transform is useful in analyzing non-stationary signals where the Fourier transform may fail [102]. As bio-signals such as PCG

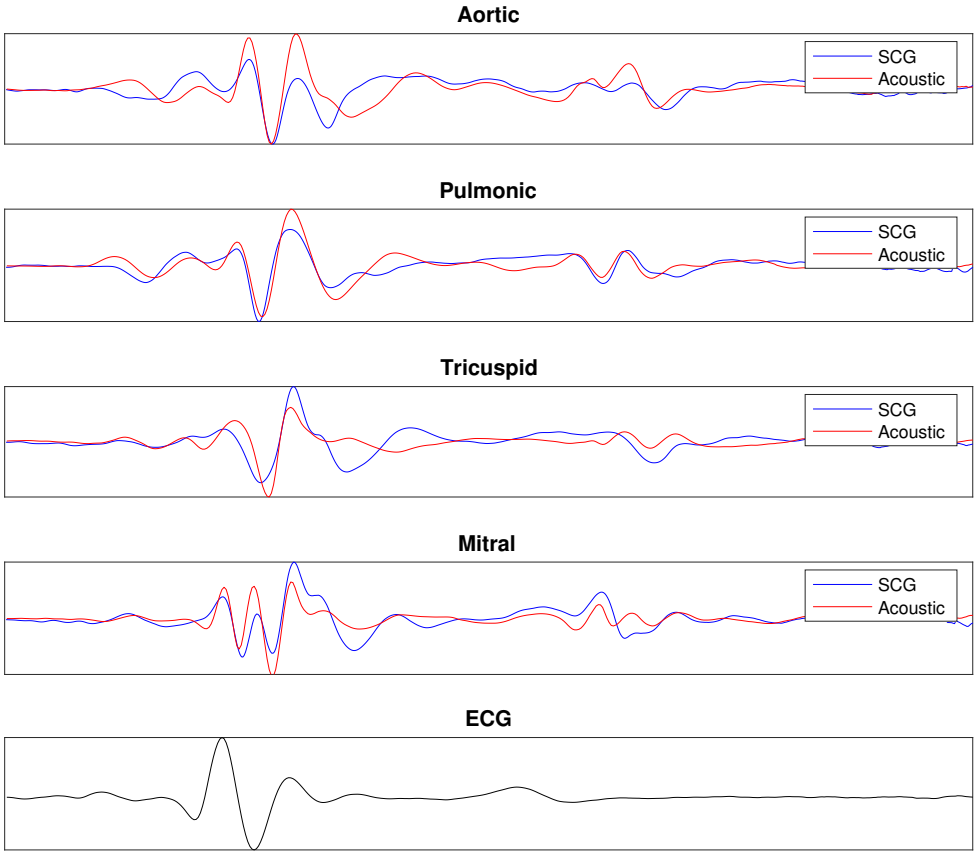

Figure 6.7: Low-frequency components of simultaneously recorded PCG and SCG signals

are non-stationary [42], the wavelet transform has been widely used to analyze bio-signals.

There are two wavelet transforms: continuous wavelet transform (CWT) and discrete wavelet transform (DWT). CWT is defined as

$$X(a,b) = \frac{1}{\sqrt{|a|}} \int_{-\infty}^{\infty} x(t)\psi^* \left(\frac{t-b}{a}\right) dt \tag{6.1}$$

where ψ^* is the conjugate of a function called the mother wavelet, a is the scale parameter, and b is the shifting parameter. In CWT, the scale and shifting parameters can vary continuously. DWT, on the other hand, has a coarsely discretized scale parameter such that the scales in the DWT are with a base equal to 2.

We apply CWT to PCG signals to analyze them in both time and frequency domains simultaneously. Such analysis is called the time-frequency analysis. The time-frequency representation of PCG signals may reveal more features that are not observable in the time-domain waveforms. For example, the valvular components during the heart sounds are not distinguishable in the waveform while they are separately detectable in the time-frequency representation of the PCG signal [33].

One of the most widely used techniques for time-frequency analysis is Short-Time Fourier Transform (STFT), which is defined as

$$X(\tau, \omega) = \int_{-\infty}^{\infty} x(t) w(t - \tau) e^{-i\omega t} \, dt \tag{6.2}$$

where $x(\cdot)$ is a time-domain signal; $w(\cdot)$ is a window function; τ and t are time; and ω is frequency. While STFT has been commonly used for PCG analysis, it has a well-known issue of a trade-off between time and frequency resolutions. That is, increase in the time resolution decreases the frequency resolution and vice versa. As a remedy to this issue, CWT can be used as an alternative to STFT. CWT provides good frequency resolution for low-frequency components and good time resolution of high-frequency components [82][127]. This property makes CWT a good candidate for time-frequency analysis of PCG signals, whose frequencies of interest are relatively low. Figure 6.8 illustrates the time-frequency representation of a raw PCG signal of two cardiac cycles as expressed by the magnitude of the CWT coefficients, in which bright yellow indicates large magnitude while dark blue indicates low magnitude. As annotated, S1 and S2 are visible as bright regions.

We have examined the characteristics of the CWT of PCG signals from subjects with high PCWP and those with low PCWP in the OHSU trial dataset. Higher magnitude was observed in the low frequency during diastole for high PCWP subjects in comparison to low PCWP subjects. Such characteristic is further analyzed and extracted as a feature as will be described in Chapter 7. Figure 6.9 compares the CWT of the PCG signal from a high PCWP subject and that from a low PCWP subject.

Wavelet transform is further applied to process the PCG signal. In order to extract the low-frequency components of the PCG signal, signal decomposition via DWT is performed.

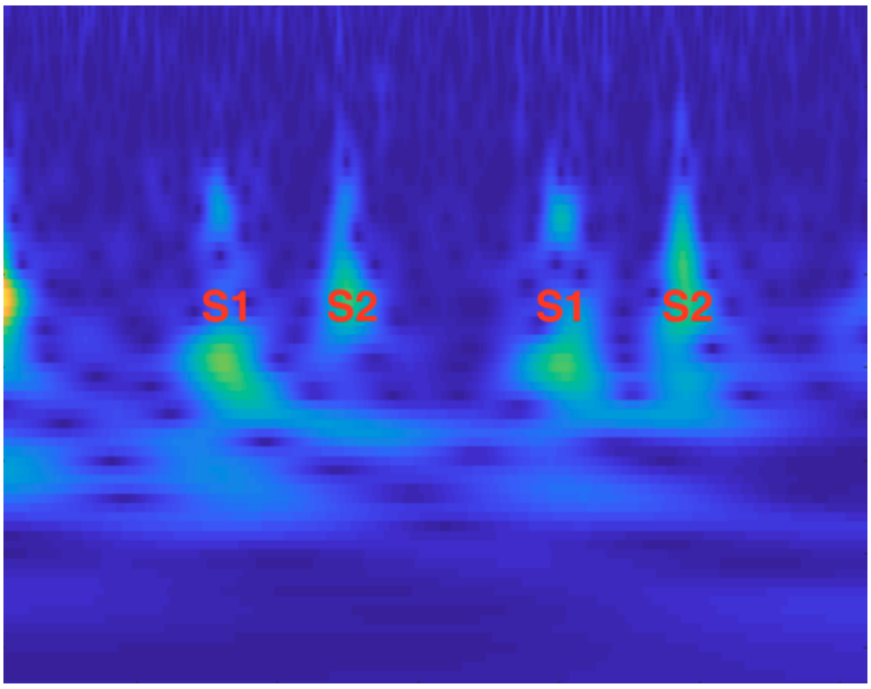

Figure 6.8: CWT image of PCG signal including two cardiac cycles

Then, the signal is reconstructed with the detail coefficients that have low-frequency components. Figure 6.10 shows an example of a raw PCG signal and a corresponding reconstructed low-frequency signal.

6.4 Noise Suppression

6.4.1 Introduction

One of the main problems with PCG signals is noise [77]. PCG signals are known to be sensitive to noise. Accurate measurement of signal characteristics may not be possible in noisy signals, leading to inaccurate computation of PCWP and mPAP. Thus, it is critical to minimize the noise in the signal.

There have been several proposed methods for PCG denoising. One of the most popular approaches is wavelet-based denoising as studied in [77] and [47]. In this approach, the PCG signal is decomposed via DWT. Among the decomposed wavelet detail coefficients, those

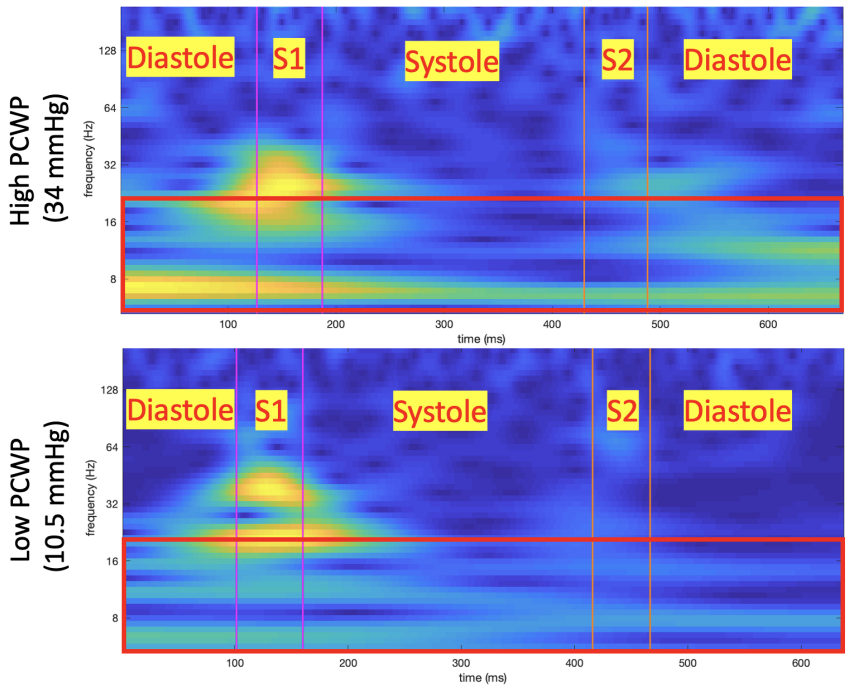

Figure 6.9: Time-frequency representation of PCG signals from a high PCWP subject and a low PCWP subject

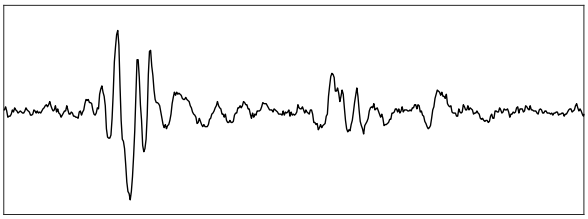

(a) Raw PCG signal

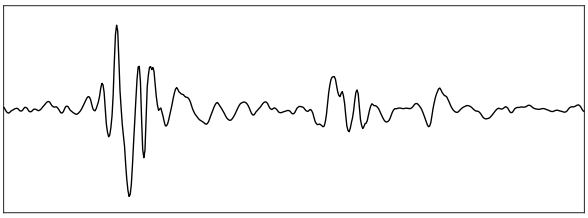

(b) Reconstructed low-frequency PCG signal

Figure 6.10: Demonstration of low-frequency PCG signal generated with DWT

below a certain threshold are removed or reduced to suppress noise. Subsequently, the signal is reconstructed from the resulting coefficients.

Another approach for noise removal is via adaptive filtering [35][34]. This technique involves an additional sensor to record only noise as the reference. The PCG sensor captures the primary cardiac signal and noise that is unrelated to the cardiac signal. The additional sensor captures reference noise that is related, but not identical, to the noise captured by the PCG sensor. An adaptive filter is applied to the reference noise to match the noise in the PCG signal. Then, the resulting filtered reference noise is subtracted from the PCG signal.

There has been adoption of a commonly used denoising algorithm in speech processing called spectral noise subtraction algorithm [114] for denoising heart sounds [87]. In our system, denoising of the audible PCG signal is performed via this approach using an algorithm implemented in [20]. The rest of this section will focus on noise reduction in low-frequency PCG signals.

Low-frequency PCG signals are characterized by their high periodicity. However, it is sensitive to motion artifacts like SCG signals are. A commonly used technique to reduce motion artifacts in SCG signals is ensemble average where several heartbeat segments are averaged to emphasize the common cardiac features while suppressing noise [99][43][73]. Ensemble averaging technique has been also used for artifact reduction in ECG signals [24]. Similarly, ensemble average technique can be applied to low-frequency PCG signals to reduce potential motion artifacts.

Ensemble averaging requires the waveform features to be precisely aligned in time to result in constructive addition of the underlying periodic components. Enabled by our accurate and precise heartbeat segmentation algorithm presented in Chapter 5, low-frequency PCG signals can be accurately segmented and synchronized in time as shown in Figure 6.11. This assumption may remain true for normal signals. However, in the presence of heart rate variability, the relative locations of the waveform features are no longer consistent. Thus, the synchronization of the heartbeat segments may become gradually weaker towards the end of the segments as shown in Figure 6.12.

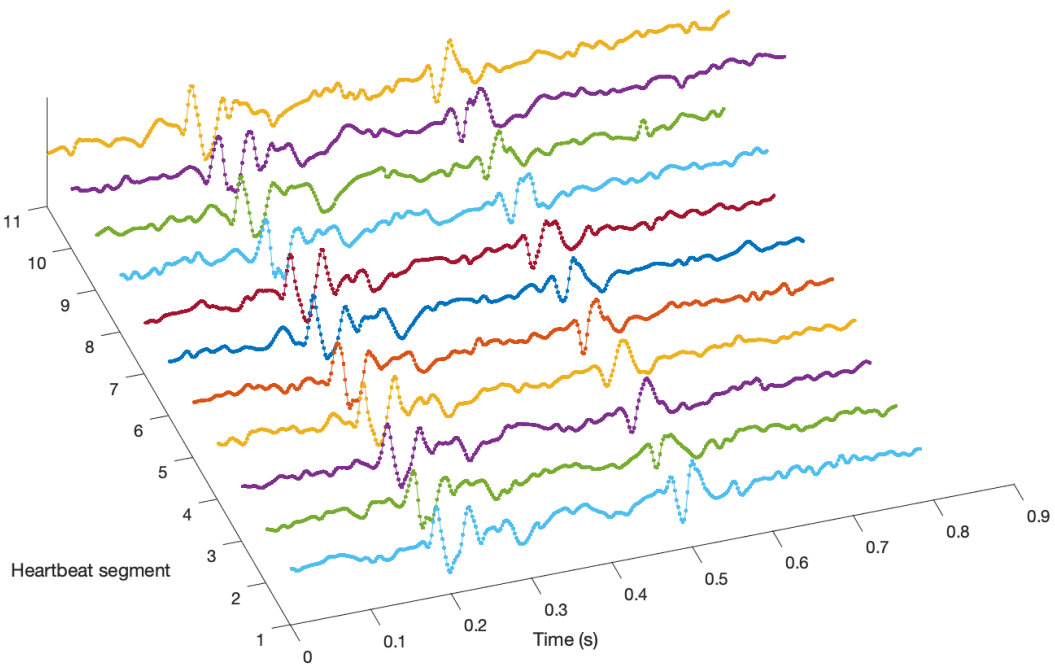

(a) Low-frequency heartbeat segments

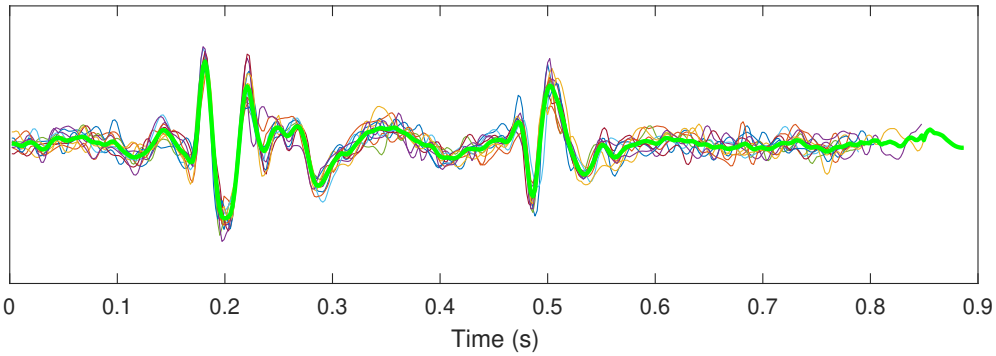

(b) Superimposed low-frequency segments and ensemble average in light green

Figure 6.11: Illustration of several consecutive heartbeat segments that exhibit periodic pattern with noise and ensemble average that suppresses noise

In order to accommodate heart rate variability, a flexible means to synchronize speed-varying heartbeat segments is needed. A well-known technique for matching time series signals with varying speed is Dynamic Time Warping (DTW), which was first introduced

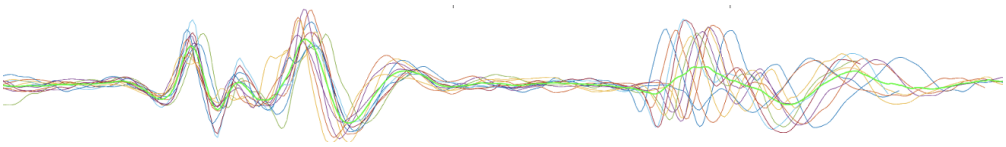

Figure 6.12: Superimposed heartbeat segments with varying duration

to handle various speaking speeds in speech recognition [94]. DTW exploits the distance between two signals to find a warping path that matches them. Suppose we have two signals X and Y as follows.

$$X = x_1, x_2, ..., x_i, ...x_m$$

$$Y = y_1, y_2, ..., y_j, ...y_n$$

From these signals, a $m \times n$ distance matrix D is generated where each element $D(i, j)$ of the matrix contains the accumulated distance between two points x_i and y_j. The accumulated distance is computed as follows.

$$D(i, j) = dist(x_i, y_j) + min[D(i-1, j-1), D(i-1, j), D(i, j-1)] \tag{6.3}$$

where $dist(x_i, y_j)$ is the distance, typically the Euclidean distance, between x_i and y_j. Once every element of the distance matrix is computed, the warping path can be trace from the top right element. The adjacent elements are compared, and the path continues to the element with the smallest value. This process continues until the path reaches the bottom left element.

Although time matching via DTW has been effective for many applications, it may not be robust for low-frequency PCG signals, which potentially exhibit amplitude variability. The DTW algorithm only depends on the pairwise distance between two signals without taking the morphological features into account. Thus, it is not very reliable if two signals have not only time variability but also amplitude variability as time is no longer the only factor when determining the distance. Figure 6.13 shows an example where the time warped signals not only fail to retain the morphological features of the original signals but also include several flat segments. For instance, the local maximum of signal 2 as marked by an arrow in the figure should match with the corresponding local maximum of signal 1 marked

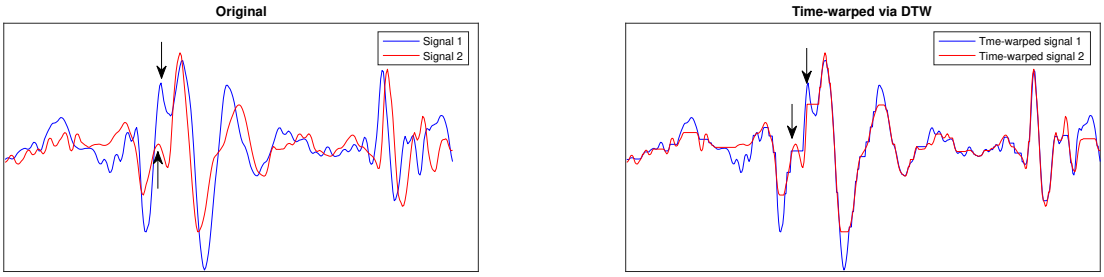

Figure 6.13: Application of classic DTW to low-frequency PCG signals

by another arrow. These peaks have considerable difference in the amplitude, leading to an error in DTW. As shown in the right plot, DTW matches it with a point on the positive slope before the corresponding local maximum of signal 1. Here, restriction on the warping path is configured such that the duration of straight-fit between signal 1 and signal 2 is less than 0.02 second. Without such restriction, the mismatching can be even more significant.

In order to mitigate the DTW's reduced performance for signals with varying amplitude, an extension to DTW named Derivative Dynamic Time Warping (DDTW) has been proposed wherein the derivative of the signals is used to compute the warping path instead [64]. Using the derivative, DTW matches the signal slope feature that is more descriptive of the signal morphology. In the same example in Figure 6.13, the local maximum of signal 2 and the matched point on the positive slope of signal 1 have similar amplitude but significantly different slope. Despite the significantly larger amplitude at the corresponding local maximum of signal 1, it has a matching slope and thereby is be matched by DDTW. Such correct matching is demonstrated in Figure 6.14, which shows the same example signals after applying DDTW.

DDTW has its own limitation. Even small amount of noise in the signal can result in unwanted peaks in the derivative. For instance, the second peak following the arrow-marked peak in signal 2 in Figure 6.13 has an inflection point on its positive slope. This inflection point results in a peak in the derivative. As shown in Figure 6.14, this inflection point is matched with a nearby local maximum of signal 1, which is extended to also match with the local maximum of signal 2's corresponding peak whose positive slope include the inflection

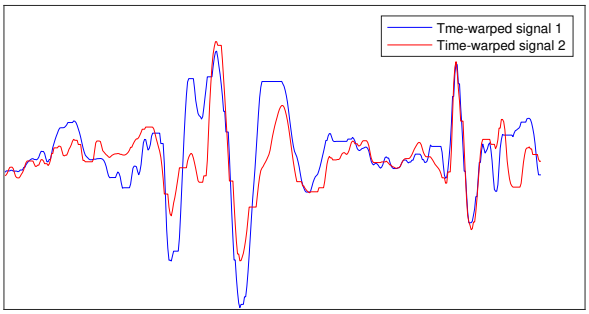

Figure 6.14: DDTW

point. Furthermore, high-frequency noises may result in large peaks in the derivative that cannot be distinguished from the actual prominent features.

The limitations of these methods are due to the fact that they only consider one type of signal characteristics. Instead, we explored an approach, which combines the amplitude and slope features and an additional feature, the second derivative, when computing the distance matrix for DTW. This is similar to a prior method wherein a weighted combination of DTW and DDTW is used to find the warping path [46]. In the approach we have explored, the 3-dimensional squared Euclidean distance is computed as follows.

$$distance_{ij} = \alpha(x_i - y_j)^2 + \beta(\dot{x}_i - \dot{y}_j)^2 + (\ddot{x}_i - \ddot{y}_j)^2 \tag{6.4}$$

where $\dot{x}_i$ and $\dot{y}_j$ denote the value of the derivative of X at i and the value of the derivative of Y at j while $\ddot{x}_i$ and $\ddot{y}_j$ denote the values of the second derivative. α and β are the weights on the original signal and the first derivative. The resulting distance is then used to compute the accumulated distance matrix D to find the warping path. Figure 6.15 demonstrates effective signal alignment using this approach. The aligned signals do not exhibit the problems we have observed in the examples with the classic DTW and DDTW.

Although the modified DTW method described above is effective in general, it can potentially distort signals to overfit especially in the presence of substantial noise. Thus, a simple yet robust alternative method has been explored. Cross-correlation is commonly used technique for matching heart sounds [45][18]. This heart sound matching is primarily based on

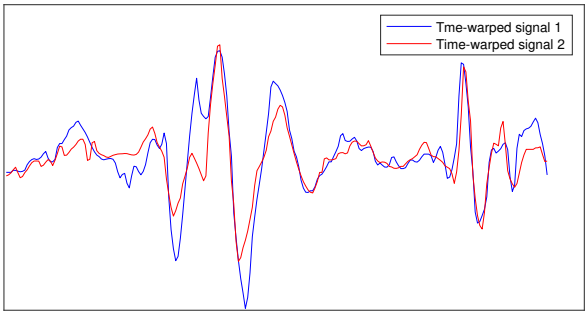

Figure 6.15: Signals aligned by modified DTW

temporal shifting of a heart sound segment to match another segment according to the delay computed with cross-correlation. As for time alignment of signals with heart rate variability, mere temporal shifting cannot match the whole heartbeat.

We have observed that S1 and S2 segments tend to have the best signal-to-noise ratio (SNR) and remain somewhat periodic in comparison to other segments even in the presence of substantial noise. Based on this observation, we have developed a robust time alignment method. The time delays between two signals at S1 and S2 are separately computed via cross-correlation. Subsequently, the systole and diastole segments are stretched or shortened according to the time delays to match the signals.

6.4.2 Method

As the first step of time alignment based on cross-correlation, S1 and S2 segments need to be identified. An existing heart sound detection algorithm presented in [20] is used to find the onset and end of S1 and S2. Then, cross-correlation is first computed to find the time delay between the S1 segment of the first heartbeat signal and the S1 segment of the second heartbeat signal. Subsequently, cross-correlation is computed to find the time delay between the S2 segments of the signals. Using these time delays, the systole and diastole segments of the second signal is stretched or shortened to match the first signal. Figure 6.16 demonstrates the time alignment based on cross-correlation. The signals are not as tightly

matched as those by the modified DTW. However, the signals are sufficiently aligned without significant morphological distortion to overfit.

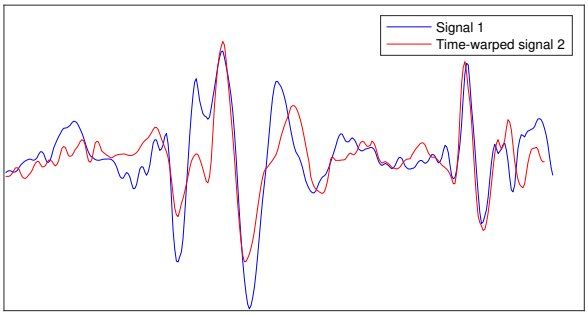

Figure 6.16: Signals aligned by the method based on cross-correlation

In order to use the time alignment method for ensemble averaging of several heartbeat segments, we need to select a heartbeat segment as the reference for the other heartbeat segments to match. The heartbeat segment that is the best representation of the overall signal morphology as measured by the median Pearson correlation coefficient is selected as the reference. The median Pearson correlation coefficient is computed as follows. For each heartbeat segment, time alignment is performed between it and other heartbeat segments within every 10-second signal. Then, the Pearson correlation coefficient is computed for each pair of the time aligned segments. The median of the coefficients is the median Pearson correlation coefficient for the particular heartbeat segment. Once this is computed for all segments, the one with the largest value is selected as the reference. Then, time alignment is applied to match all other heartbeats with the selected reference. Finally, the time-aligned heartbeat segments are ensemble averaged.

6.4.3 Result

The noise suppression method for low-frequency PCG signals has been tested with the UCLA and OSHU trial datasets and has shown to be effective as demonstrated by an example in Figure 6.17. As shown in (a), the heartbeat segments are not precisely aligned. The ensemble

average of the segments would yield a distorted waveform as shown in (c). The aligned segments using the presented cross-correlation method are shown in (b). The ensemble average after the alignment retains the waveform characteristics as shown in (d).

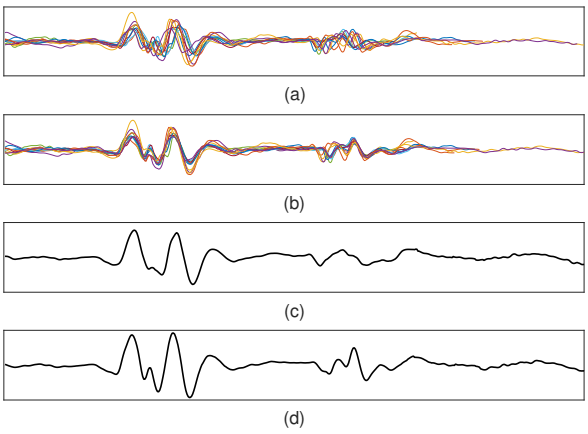

Figure 6.17: Demonstration of heartbeat synchronization and ensemble averaging. (a) Superimposed heartbeat segments, (b) Synchronized heartbeat segments, (c) Ensemble average without synchronization, (d) Ensemble average with synchronization

Figure 6.18 further demonstrates the method in noisy signals. The example on the left side shows moderately noisy signal segments that are not precisely aligned. Ensemble-averaging of these segments suppresses not only the noise but also the signal characteristics. The positive peak during S1 is not as sharp, and the preceding negative peak is suppressed. If the segments are time-aligned and ensemble averaged, the noise is minimized while the signal characteristics are retained. The example of the right side shows higher degree of noise and misalignment in the signal segments. The ensemble average without time alignment as shown in (c) fails to retain the signal morphology while ensemble average with time alignment in (d) effectively demonstrates noise suppression.

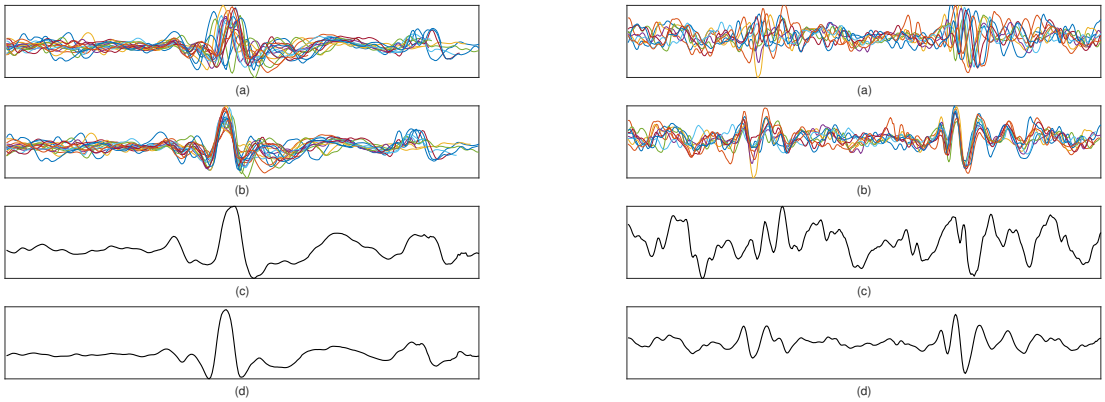

Figure 6.18: Noisy low-frequency PCG signals and demonstration of noise suppression

6.5 Summary

In this chapter, we have presented several analysis and processing methods for PCG signals. Various frequency bands of PCG signals have been examined. According to the PSD of the signals, the signal power is observed to be the largest in the low-frequency range. Thus, the low-frequency components is investigated further. The signal waveforms in different frequency ranges have been investigated, and those in the low-frequency range exhibit highly periodic patterns, suggesting that the low-frequency components correspond to cardiac activities.

We have further examined the low-frequency PCG by comparing with SCG. An experiment has been conducted wherein an accelerometer sensor device is attached to each acoustic sensor to simultaneously record acceleration and acoustic signals. The low-frequency PCG signal waveforms have been observed to have similar morphology to the SCG waveforms, further suggesting that low-frequency characteristics of the PCG signal contain information that can be used to predict PCWP and PAP.

Wavelet transform, a popular technique to analyze bio-signals, has been investigated. CWT is used to acquire a time-frequency representation of PCG signals. From the time-frequency representation, we have identified a low-frequency characteristics that correlate with PCWP. Another type of wavelet transform, DWT, is used to generate low-frequency

PCG signals by decomposing raw signals and reconstructing with coefficients that contain low-frequency components.

Finally, we have developed a noise suppression method for low-frequency PCG signals via ensemble averaging of several consecutive heartbeat segments. Such approach requires precise alignment of the segments, and presence of heart rate variability makes alignment impossible via mere shifting. Thus, we have investigated DTW methods and developed a robust time alignment method based on cross-correlation. The ensemble averaging in combination with signal alignment demonstrates effective noise suppression.

CHAPTER 7

Feature Extraction

7.1 Introduction

PCG signals reflect biomechanical cardiac activities and thereby include a large amount of information. From such information in PCG signals, cardiac states of an individual can be inferred. The information is extracted as a form of features, which are defined in machine learning as measurable properties of signals. The extracted features can be used to train machine learning algorithms to predict cardiac conditions. This chapter describes the method for extracting features that show high correlation with PCWP and mPAP.

There have been several studies in PCG features and their applications for cardiac state assessment. These include cardiac murmur detection and valve disorder diagnosis based on PCG signals. In [104], mel-frequency cepstral coefficients (MFCC) and DWT features in PCG signals are used to detect valve disorders. MFCC are commonly used for audio signal processing where sound is represented as a set of amplitudes of power spectrum on a frequency scale that is modeled after human pitch perception called mel-frequency scale. [14] is another work that also explores MFCC as features to detect ventricular septal defect and atrial septal defect. In addition to the MFCC features, one-dimensional local ternary patterns are also explored as features. Local ternary pattern is an extension of local binary pattern, a commonly used feature in computer vision [49]. [97] proposes a method for detecting coronary artery disease with spectral features such as instantaneous frequency and signal complexity features such as spectral entropy in PCG signals.

While not studied explicitly as features for machine learning algorithms, there are characteristics in PCG signals that have been studied for their relationship with hemodynamics.

In [100], the relationship between ventricular pressures and S1 components observed in both intracardiac and external PCG signals are investigated. The observation suggests that the first, second, and third components of S1 coincide with the rapid rise of the first derivative of left ventricular pressure (dP/dt), sudden change of course of dP/dt, and sudden increase of aortic wall tension respectively. In [93], the amplitude of S1 is investigated, and a linear relationship with dP/dt have been observed. In [11], spectral characteristics of heart sounds have been investigated and shown a relationship with physiological characteristics of subjects including hypertension.

7.2 Methods

While a model that links PCG signals and underlying physiology related to PCWP and PAP does not yet exist, our investigation of the PCG signals in the OHSU dataset, which covers wide ranges of PCWP and PAP, has led to potential features that correlate with the pressure metrics. The developed features are based on several signal characteristics including amplitude, spectral characteristics, waveform morphology, power, and harmonicity. The features are extracted from S1, S2, systole, early diastole, and late diastole of the PCG signals from the four sensors separately. PCG signals are segmented into these phases of the cardiac cycle according to the onset and end of S1 and S2 as determined by the algorithm presented in [20]. The systole is defined here as the duration between the end of S1 and the onset of the subsequent S2. The diastole is defined as the duration between the end of S2 and the onset of the subsequent S1. The early diastole and late diastole are defined as the first and second halves of the diastole respectively.

The amplitude of low-frequency PCG signals during different phases of the cardiac cycle has been examined. The investigated characteristics include root mean square (RMS) amplitude and peak amplitude. Both the low-frequency PCG signal and its envelope have been analyzed for these features. We have observed that the overall signal strength significantly affects the amplitude. Thus, relative amplitudes as expressed by the ratios of the amplitude during different phases are also considered. We have also considered the skewness

of the low-frequency PCG signal to measure the symmetry of the distribution of the signal amplitude.

The features based on the spectral characteristics include the spectral centroid and fundamental frequency. The spectral centroid is computed as

$$centroid = \frac{\sum_f f|X(f)|^2}{\sum_f |X(f)|^2} \tag{7.1}$$

where f and X denote the frequency and the discrete Fourier transform (DFT) of the PCG signal. The fundamental frequency is computed as the frequency at which the power spectral density of the PCG signal has the maximum amplitude. For the spectral centroid, the different phases in low-frequency PCG signals and the heart sounds in audible PCG signals are considered. As for the fundamental frequency, low-frequency PCG signals are considered as it corresponds to the natural frequency of the low-frequency chest wall vibration.

The morphology-based features include the peak width and slope. The peak width is measured as the distance between the upcrossing and downcrossing points at the mid-height of the peak. The peak width is computed from the envelope of low-frequency PCG signals. Combining with the peak amplitude feature, the peak height-to-width ratio is also computed as a feature. We have also considered the slope as features including the maximum and minimum of the derivative of low-frequency PCG signals.

We have investigated the power ratio between the systole and diastole. The power is defined here as $|w(a,b)|^2$ where $w(a,b)$ is the CWT coefficient for scale and shifting parameters a and b. As the first step to compute this feature, the CWT is computed for the raw PCG signal. Subsequently, the CWT coefficients that correspond to frequencies below 5 Hz and above 20 Hz are removed. The power for the remaining CWT coefficients is computed. The 20th percentile of the computed power is considered as the noise floor to subtract. Then, the average of the noise-floor-removed power during the systole and that during the diastole are computed. The ratio of the resulting average powers is the power ratio feature.

Finally, we have analyzed the harmonic ratio, which measures the PCG signal harmonicity, or the ratio between the energy in the harmonic components and the total energy. The

harmonic ratio is computed for low-frequency PCG signals during the early diastole according to the definition in [66].

Correlation between each feature and each pressure metric is analyzed to determine the candidate features. The candidate features are then organized into groups of related features. Once the candidate features are prepared, principal component analysis (PCA) is applied to each group of features to reduce the dimensionality. Figure 7.1 demonstrates the correlation between some of the resulting features and PCWP in the OHSU dataset.

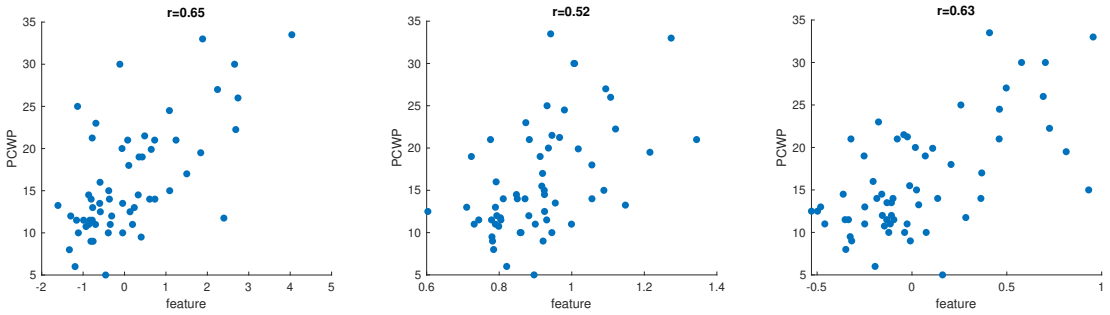

Figure 7.1: Features and their correlation with PCWP. (a) spectral centroid, (b) power ratio, (c) RMS

7.3 Summary

In this chapter, we have presented features from PCG signals that are correlated with PCWP and mPAP. Several types of features have been developed based on different characteristics of PCG signals including the amplitude, spectral characteristics, waveform morphology, power, and harmonicity. The correlation between each of the extracted features and each pressure metric has been analyzed to determine the candidate features. PCA is applied to groups of related features to reduce the dimensionality. The resulting features are then utilized by the machine learning algorithms to compute the PCWP and mPAP.

CHAPTER 8

PCWP and PAP Computation via Hierarchical Approach

8.1 Introduction

This chapter describes the method for pressure metric computation based on the developed PCG features. For this computation, we developed an algorithm based on machine learning. As the name suggests, machine learning is an approach wherein a machine automatically learns from data to build a model that makes decisions or predictions without being explicitly programmed. In general, there are three main categories of machine learning: supervised learning, unsupervised learning, and reinforcement learning. In supervised learning, data with a pre-assigned output label for each input is used to train a model that predicts an output based on a given input. In contrast, an unsupervised learning algorithm is trained with data that only contains inputs and is used to find patterns such as clusters in the data. A reinforcement learning algorithm involves an agent finding actions at given states in an environment to maximize accumulated rewards.

Supervised learning is a feasible approach to build a model for pressure metric computation. In this approach, the set of PCG features and the ground truth pressure metric values from the trial data are considered as the input and output for training. Supervised learning is typically used to perform classification or regression. In a classification problem, the output is a set of discrete categories. An example is classification of benign and malignant tumors where the output categories are "benign" and "malignant." On the other hand, in a regression problem, the output is a continuous numerical value. An example is house price

prediction where the house price is the continuous numerical output. As PCWP and mPAP are continuous numerical metrics, a regression method is developed to compute the pressure as its output given a set of PCG features as its input.

There are several choices of algorithms to perform regression. Ordinary Least Square (OLS) regression is a simple and commonly used algorithm to perform linear regression, which finds the linear relationship between the dependent variable (output) and independent variable (input). If there are more than one input, an extension of this algorithm called multiple linear regression is used. The simplicity of linear regression makes it easy to interpret and robust given a relatively small dataset size. However, an obvious limitation is that it cannot be used for nonlinear problems. If the relationship between the input and output is not linear, a special case of multiple linear regression called polynomial regression can be used instead. Other types of linear regression are Ridge regression and Lasso regression, which use L2 and L1 regularization technique to reduce complexity. Details of these regression techniques can be found in [58][113]. Other commonly used machine learning methods for regression include support vector regression, artificial neural network (ANN), and ensemble regression. The details of these algorithms are out of this dissertation's scope.

The pressure metric computation algorithm is designed with multiple linear regression due to its simplicity and robustness. Complex models would require a large amount of data for robust training. However, the available training data size is relatively small. Additionally, the developed PCG features have shown relatively linear correlation with the pressure metrics. Therefore, multiple linear regression is a feasible approach.

Linear regression has been favored due to its properties, but it is also known to be highly sensitive to outliers. Outliers may represent only a small fraction of the dataset, but they may have a significant impact on the slope of the regression hyperplane. Thus, the effect of the outliers must be minimized in order to train a linear regression model to capture the overall trend of the data points. As alternatives to linear regression, there are methods for fitting a robust line in the presence of outliers such as Theil-Sen estimator [112][98]. Another approach to handle outliers is to exclude them during training. It is important to

note that outliers are not excluded during validation unless it is certain that the outliers have deviated values due to noise in the measurement. If presence of noise in the measurement is uncertain, the outliers may be valid observations and thereby should not be removed from analysis because the deviation may be due to certain physiology rather than measurement error.

While an outlier does not have a universal definition and is often difficult to detect, there have been several proposed methods for outlier detection. A survey of these methods is presented in [57]. Despite the lack of a universally accepted specific definition of an outlier, outliers can be generally categorized into univariate and multivariate outliers. A univariate outlier is an observation whose single variable value deviates significantly from the other observations, whereas a multivariate outlier is an observation that deviates from other observations in multidimensional space. The mainly concerned outliers in our system are bivariate outliers given the two variables being the pressure metric and each of the features. In other words, observations that appear to be an outlier in the joint combination of the pressure metric and any feature are detected and removed during training. Subsection 8.2.1 further describes the bivariate outlier detection method we have developed.

In order to improve the prediction accuracy, we designed a hierarchical algorithm where multiple linear models are used to compute the pressure metric values at different hierarchical levels. The inspiration of the hierarchical approach was drawn from loosely related existing methods: hierarchical classification and hierarchical linear modeling. Hierarchical classification involves hierarchy of categories. At the upper level in the hierarchy, more general categories are classified, and as progressing down the hierarchy, more specific categories are classified. Each branch at each hierarchical level has a dedicated classifier. Hierarchical liner modeling involves a hierarchical form of OLS regression, which considers hierarchical levels of factors. In hierarchical linear modeling, a set of linear regression models are trained at each level whose regression parameters are obtained from the upper level. Further details of hierarchical linear modeling are out of dissertation's scope but can be found in [119].

8.2 Methods

The pressure metric value is organized as two hierarchical levels as shown in Figure 8.1. At

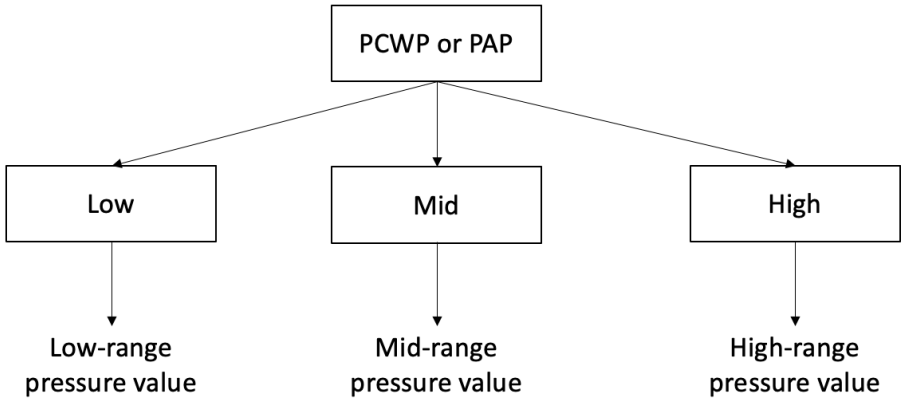

Figure 8.1: Hierarchical levels of pressure metrics

the upper level, the pressure values are divided into three categories: low, mid, and high pressure. The lower level involves the continuous pressure value within each of the upper-level categories. The upper-level linear model is trained with data covering the whole pressure range and produces a rough estimate of the pressure. This estimate is used to determine the category.

One problem of hierarchical classification is error propagation wherein an error at a level propagates to the lower levels. Similarly, the pressure metric computation algorithm may suffer from error propagation. Subjects with pressure values near the boundaries between categories are especially prone to misclassification. In order to mitigate this problem, a specially designed level of regression is added between the upper level and lower level. Instead of producing a more granular output as in a typical hierarchical design, this level is dedicated to the boundary cases and aims at improving the classification accuracy of them.

The lower level consists of three linear regression models for the low, mid, and high ranges of pressure. As another protection against error propagation, the final prediction of the pressure is computed as a weighted combination of the outputs of these models.

Following this hierarchical design, two separate pressure computation algorithms have been implemented and validated for PCWP and mPAP using the OHSU dataset. For simplicity, the subsections below generally refer to PCWP or mPAP as pressure metric in the description of the methods except for details that are specific to each of the PCWP and mPAP computation algorithms.

8.2.1 Outlier Removal

The regression models used in the algorithm are multiple linear regression models. As described above, these linear regression models are highly sensitive to outliers. Thus, outliers must be detected and removed from the training data so that the fitted hyperplane more accurately reflects the trend of the most observations. Here, an outlier is defined as a data point that deviates from the overall linear correlation between the pressure metric and any of the features. In order to detect such outliers, we have developed a bivariate outlier detection algorithm that is performed for every feature.

The outlier detection algorithm consists of two detection stages. At the first stage, bivariate outliers are preliminarily detected based on the distance between each data point and the data distribution. In multi-dimensional space, measure of such distance is given by the Mahalanobis distance, which is widely used for multivariate outlier detection [32]. The Mahalanobis distance d is defined as

$$d = \sqrt{(x-\mu)^T \Sigma^{-1} (x-\mu)} \tag{8.1}$$

where x, μ, and Σ are the data point, mean, and covariance matrix respectively. While the Mahalanobis distance well generalizes the measure of how many standard deviations a data point is away from the mean, it is known to be unreliable in the presence of outliers as the mean and covariance are both sensitive to outliers. Thus, robust estimates for the mean and covariance matrix that are less sensitive to outliers have been widely used instead in order to compute reliable Mahalanobis distance. In our algorithm, Olive-Hawkins estimate method [83] was used for computation of the robust estimates.

Mahalanobis distance assumes multivariate normal distribution. Thus, outlier detection based on this may result in false positives if the distribution is skewed. The PCWP and mPAP values in the dataset exhibit skewed distribution as shown Figure 8.2. As a result of

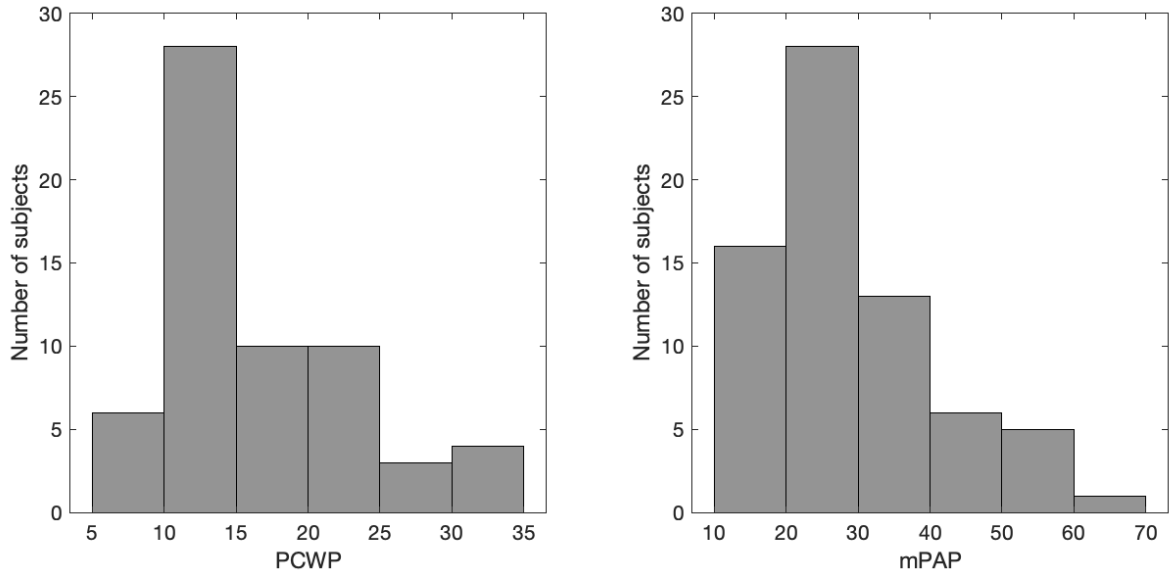

Figure 8.2: Distribution of PCWP and mPAP

the skewness, subjects with large pressure values may have large distance from the mean of the distribution and thereby be falsely detected as outliers as demonstrated in Figure 8.3a.

At the second stage, data points are re-evaluated to find the outliers based on the distance from the linear trend rather than the distribution mean. After removing the outliers detected at the first stage including the false positives, linear regression is performed on the remaining subjects. The importance of the first stage outlier detection is the removal of outliers that affect this regression at the second stage so that linear regression on the remaining data yields a regression line that generalizes the pattern of the whole dataset, making the second stage outlier detection more robust.

Following the linear regression, the standardized residual for each subject is computed to determine how far off each subject is from its expected value based on the linear trend. This approach of using standardized residual for outlier detection is a well-known traditional

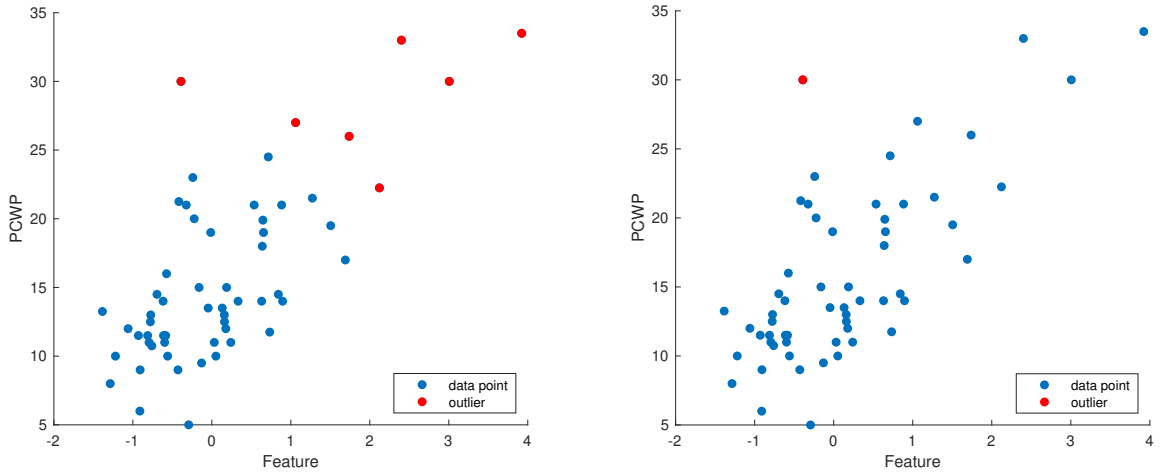

(a) Detected outliers at Stage 1

(b) Detected outliers at Stage 2

Figure 8.3: Demonstration of the outlier detection algorithm. The red points indicate detected outliers. In (a), several high PCWP subjects are falsely detected as outliers due to their large Mahalanobis distance. However, these false positives follow the linear trend between the feature and PCWP. In (b), the false positives are no longer detected as their standardized residuals are small.

method [92]. The standardized residual, r_i, for i^{th} subject is computed as

$$r_i = \frac{y_i - \hat{y}_i}{\sqrt{\frac{\sum_{j=1}^{n}(y_j - \hat{y}_j)}{n}(1 - h_{ii})}} \tag{8.2}$$

where

- y_i is the observed pressure value of the i^{th} subject;
- $\hat{y}_i$ is the predicted pressure value for the i^{th} subject;
- n is the number of subjects; and
- h_{ii} is the leverage of the i^{th} subject. The leverage is a measure of the distance between the independent variable, x, value of an observation and those of other observations, and is defined as $x_i(X^TX)^{-1}x_i^T$ [27].

Subsequently, subjects whose standardized residual exceeds 3 are considered outliers and thereby removed. Figure 8.3b demonstrates the outlier detection at the second stage. The falsely detected outliers from the first stage are no longer detected as outliers.

8.2.2 Upper-level Regression

The primary goal of the upper-level regression is to classify each subject into one of three subgroups for the lower-level models to accurately compute the pressure value. We define these subgroups for PCWP and mPAP as groups of subjects whose pressure values are in the ranges specified in Table 8.1. The upper level consists of one multiple linear regression

	PCWP	mPAP
Low	< 12 mmHg	< 20 mmHg
Mid	[12, 20] mmHg	[20, 30] mmHg
High	> 20 mmHg	> 30 mmHg

Table 8.1: PCWP and mPAP subgroups

model whose output roughly estimates the pressure metric values and is used to determine the subgroup of each subject.

It may be reasonable to assume that a classifier can be used instead of a regression model. Classification methods via a multi-class support vector machine (SVM) and a shallow neural network have been investigated. The overall classification accuracy of the shallow neural network method is marginally superior to the regression-based method. However, it is difficult to understand how likely a subject is correctly classified just based on the classifier output. Since the classes are divided subranges of a continuous pressure metric rather than discrete categories, the predicted value from the regression model can be used not only to classify each subject but also to determine how likely such classification is correct. For instance, the low-pressure subgroup includes both subjects with very low pressure and those with pressure just below the boundary with the mid pressure subgroup. Subjects near the subgroup boundaries are more likely to be misclassified.

8.2.3 Bridge-level Regression

Misclassified subjects may result in a large error if not handled properly. In order to reduce the misclassification rate, an intermediate level of regression called bridge-level regression is added between the upper level and lower level. The bridge-level consists of two multiple linear regression models that cover the boundaries as illustrated in Figure 8.4. The low-mid

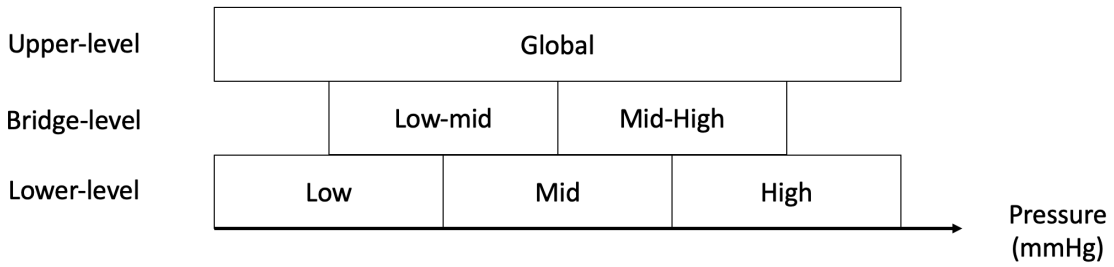

Figure 8.4: Ranges covered by the bridge-level regression models

range roughly covers the upper portion of the low subgroup and the lower portion of the mid subgroup, effectively covering the boundary between these subgroups. Similarly, the high-mid range roughly covers the upper portion of the mid subgroup and the lower portion of the high subgroup. The upper-level output that is either below the low-mid range or above the mid-high range bypasses the bridge-level as these extreme values are not likely to be misclassified.

If the error at the upper-level is substantial, it can lead to incorrect assignment of the bridge-level regression models. In order for each of the regression models to properly handle such cases, it is trained with data from an extended range. The ranges of the low-mid training data and mid-high training data include a large overlap. For example, let us suppose the upper-level regression output of a subject is in the mid-high range slightly above its boundary with the low-mid range while the ground truth value is in the low-mid range. This crossover can be properly handled by the mid-high pressure model since it has been trained with extended range of data covering the upper portion of the low-mid range.

8.2.4 Lower-level Regression

At the lower level, each subgroup has a dedicated multiple linear regression model for precise computation of the pressure metric. However, their precise computation assumes correct subgroup classification as addressed above. While the bridge level aims at reducing misclassification rate, it cannot completely prevent misclassification. In order to further handle misclassification, a strategy consisting of three techniques is implemented.

Firstly, the three regression models are trained with overlapping ranges as the bridge-level regression models are. The ranges of the training data are illustrated in Figure 8.5. The

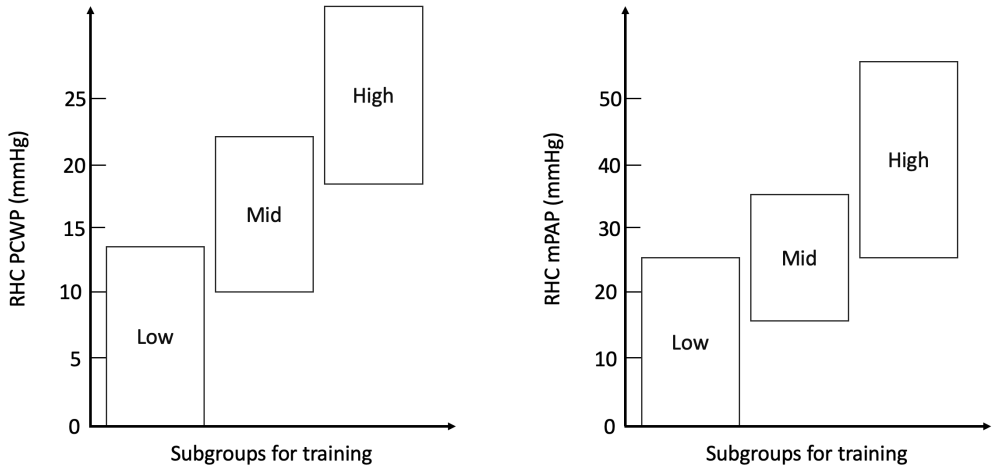

Figure 8.5: Pressure ranges of the training data for each subgroup

pressure metric for a subject near a boundary can be accurately computed by the regression models of both neighboring subgroups.

Secondly, the final predicted value is computed as a weighted combination of multiple model outputs. The weights on the lower-level model outputs are determined by the output from the previous level. For instance, the predicted pressure of a subject whose bridge-level output is at the boundary between the mid and high subgroups has equal contribution from the mid model output and the high model output. If the bridge-level output is slightly above the boundary, the weight on the high model output is increased. If the bridge-level output is substantially above the boundary, the weight on the high model is close to 100%. The

weights on the subgroup models are defined as follows.

- low-subgroup model weight

$$w_l(x) = \begin{cases} 1 & \text{if } x < A - \frac{\alpha}{2} \\ -\frac{x-A-\frac{\alpha}{2}}{\alpha} & \text{if } A - \frac{\alpha}{2} \leq x \leq A + \frac{\alpha}{2} \\ 0 & \text{otherwise} \end{cases} \tag{8.3}$$

- mid-subgroup model weight

$$w_m(x) = \begin{cases} 0 & x < A - \frac{\alpha}{2} \\ \frac{x-A+\frac{\alpha}{2}}{\alpha} & \text{if } A - \frac{\alpha}{2} \leq x \leq A + \frac{\alpha}{2} \\ 1 & \text{if } A + \frac{\alpha}{2} \leq x \leq B - \frac{\beta}{2} \\ -\frac{x-B-\frac{\beta}{2}}{\beta} & \text{if } B - \frac{\beta}{2} \leq x \leq B + \frac{\beta}{2} \\ 0 & \text{otherwise} \end{cases} \tag{8.4}$$

- high-subgroup model weight

$$w_h(x) = \begin{cases} 0 & \text{if } x < B - \frac{\beta}{2} \\ \frac{x-B+\frac{\beta}{2}}{\beta} & \text{if } B - \frac{\beta}{2} \leq x \leq B + \frac{\beta}{2} \\ 1 & \text{otherwise} \end{cases} \tag{8.5}$$

where x, A, B, α, and β correspond to the previous level output, boundary between the low and mid subgroups, boundary between the mid and high subgroups, overlap around A, and overlap around B respectively. A graphic illustration is shown in Figure 8.6.

Lastly, the lower-level output and upper-level output of each subject is compared. Significant difference between them may indicate that the lower-level output is computed with incorrect regression models. Thus, the upper-level or bridge-level output is selected instead as the final predicted pressure value. In summary, the pressure metric computation algorithm is illustrated with the flowchart in Figure 8.7.

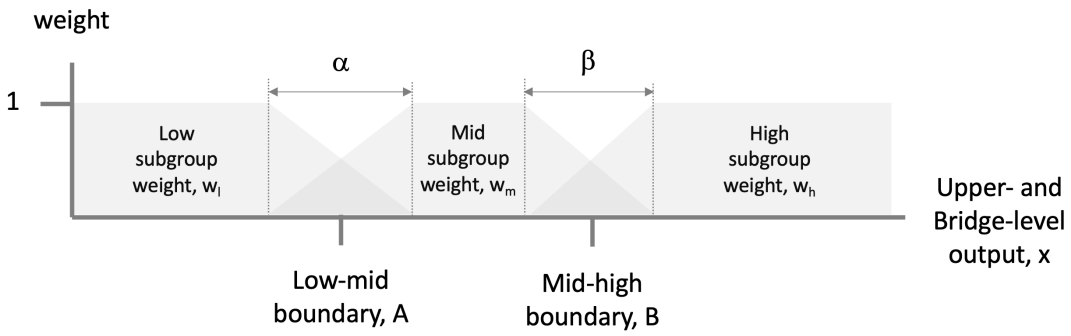

Figure 8.6: Weights on subgroups

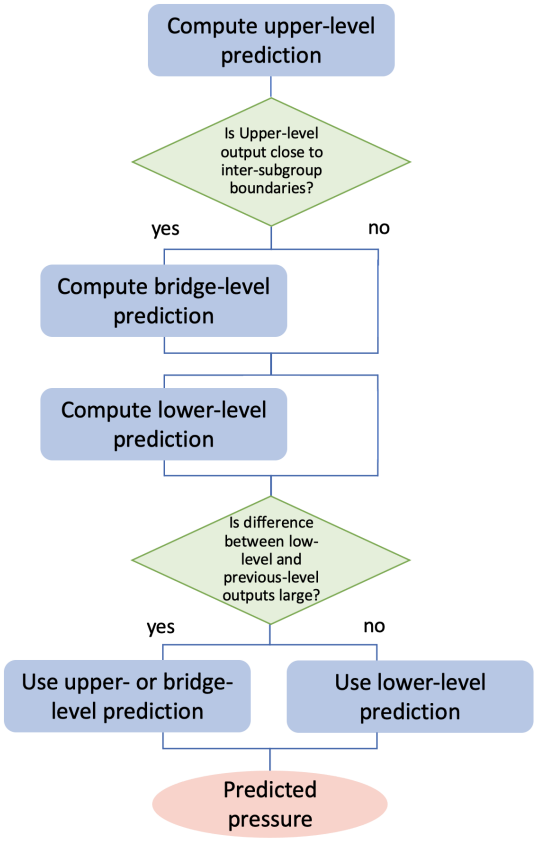

Figure 8.7: Flowchart of pressure metric computation

8.3 Result

The system has been validated via leave-one-out analysis for each of PCWP and mPAP. The predicted pressure values have been linearly transformed to yield a slope of 1 and an intercept

of 0 in the line of fit between the predicted and ground truth values. N=58 subjects from the OHSU trial dataset have been used for validation of the PCWP computation. Figure 8.8 compares the predicted PCWP values at each hierarchical level and the corresponding ground truth values obtained from right heart catheterization.

The plots demonstrate that the prediction accuracy improves as the computation progresses to the lower levels. The upper-level prediction values as shown in Figure 8.8a include clustered values in the mid range and thereby would have led to a substantial number of misclassified subjects if they were directly used for classification. The bridge-level prediction resolves such clustering as shown in Figure 8.8b and improves classification accuracy. Comparison between the final predicted PCWP values shown in Figure 8.8c and the ground truth values yields coefficient of determination (R^2), mean absolute error (MAE), and standard deviation of the difference as summarized in Table 8.2.

R^2	MAE	standard deviation
0.86	1.90 mmHg	2.43 mmHg

Table 8.2: PCWP computation result

Figure 8.9 shows a Bland-Altman plot comparing the predicted PCWP and the ground truth. Proposed in [19], a Bland-Altman plot is a commonly used technique in the biomedicine field to analyze the agreement between two measurement methods such as a new measurement technique and the gold standard. The x-axis is the mean of two measurements while the y-axis is their difference. The plot indicates the bias and 95% limits of agreement. The bias is the mean difference, and the 95% limits of agreements are computed as mean difference $\pm$ 1.96 $\times$ standard deviation of the difference. The predicted and the ground truth PCWP values yield a bias of 0 and the 95% limits of agreement of $\pm$4.76 mmHg. 94.8% of the tested subjects are within the limits of agreement.

The following is the mPAP computation result of leave-one-out validation on N=65 subjects from the OHSU dataset. Figure 8.10 shows the prediction result at each hierarchical level. As observed in the PCWP results, the mPAP prediction accuracy improves as the com-

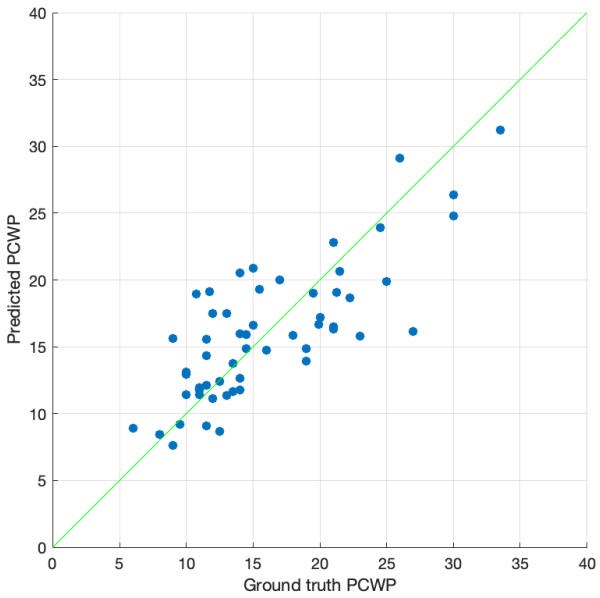

(a) Upper-level prediction vs Ground truth

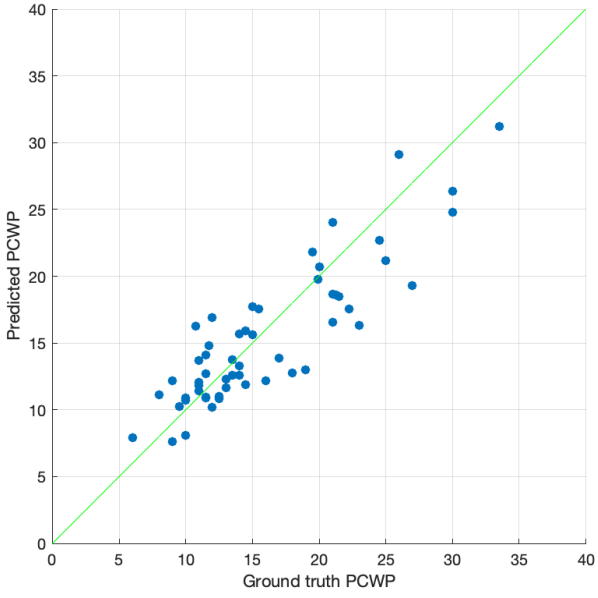

(b) Bridge-level prediction vs Ground truth

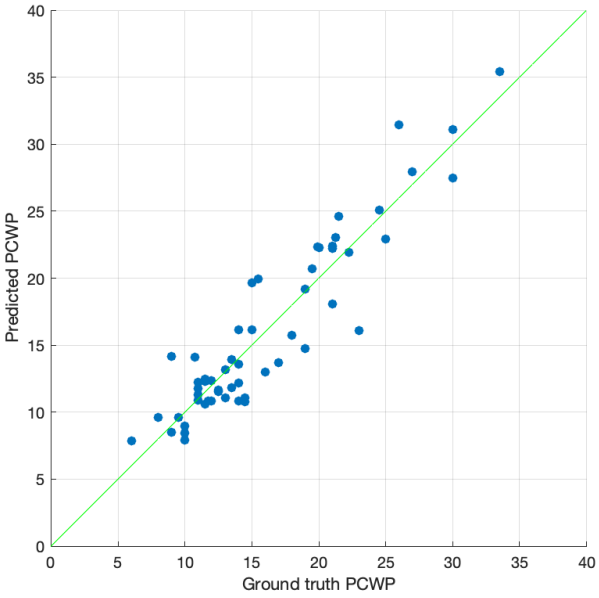

(c) Final prediction vs Ground truth

Figure 8.8: PCWP computation result

putation progresses to the lower levels. The R^2, MAE, and standard deviation of difference are shown in Table 8.3. Figure 8.11 shows a Bland-Altman plot comparing the predicted mPAP and ground truth, yielding a bias of 0 and 95% limits of agreement of ± 11.88 mmHg.

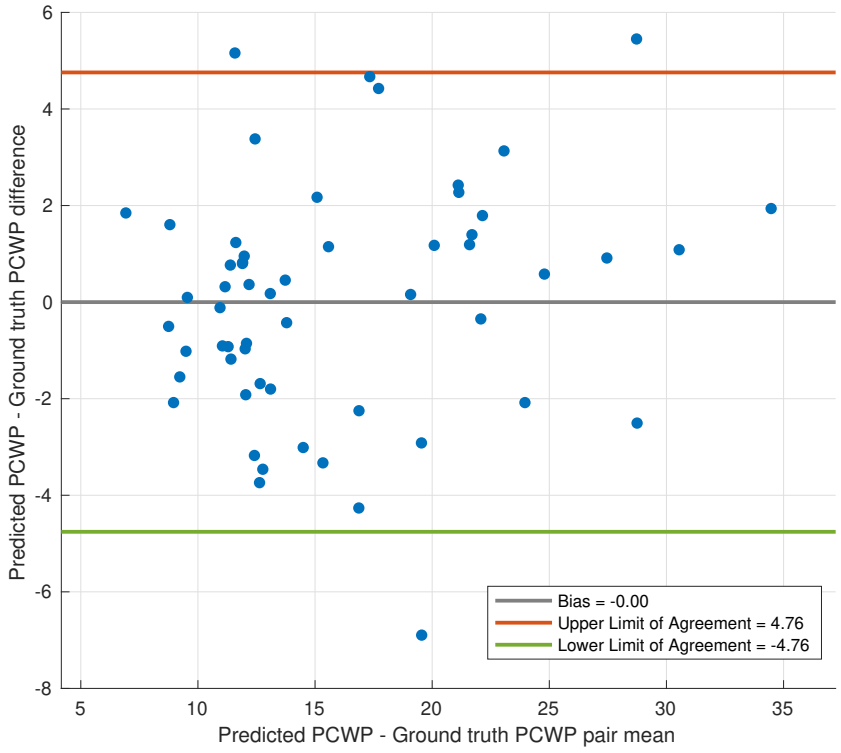

Figure 8.9: Bland-Altman plot of predicted PCWP and ground truth PCWP comparison

90.8% of the tested subjects are within the limits of agreement.

R^2	MAE	standard deviation
0.80	4.11 mmHg	6.06 mmHg

Table 8.3: mPAP computation result

8.4 Summary

In this chapter, we have proposed a hierarchical method for accurate PCWP and mPAP computation. Inspired by hierarchical classification framework, the presented algorithm includes multiple levels to produce more precise prediction as it progresses towards the lower level. The upper level consists of a multiple linear regression model that generates rough

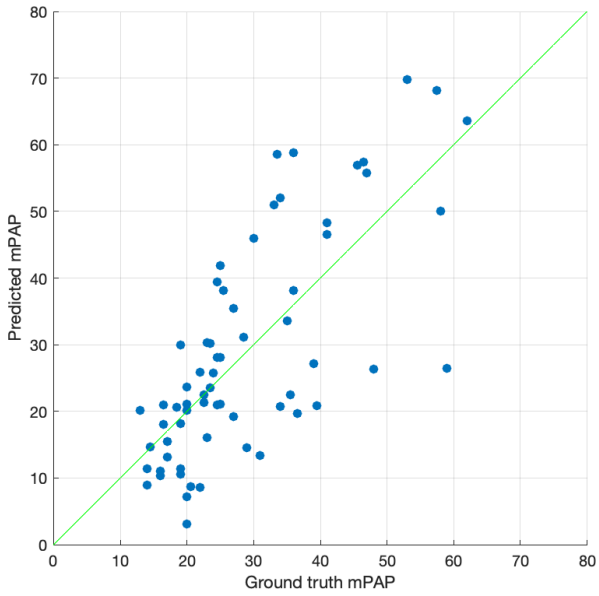

(a) Upper-level prediction vs Ground truth

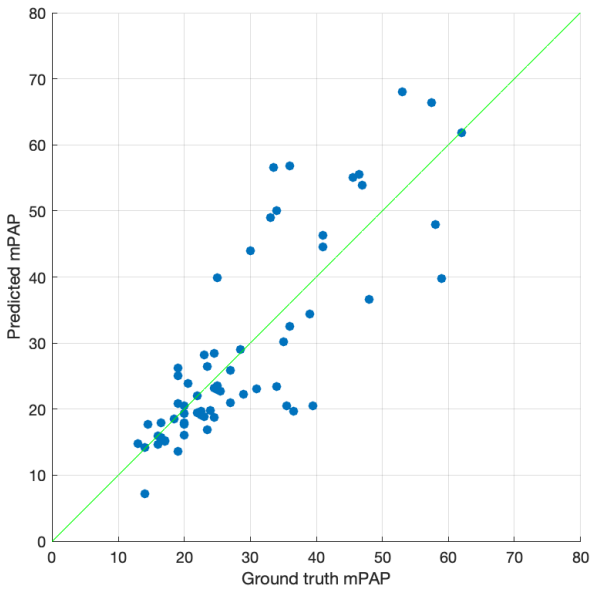

(b) Bridge-level prediction vs Ground truth

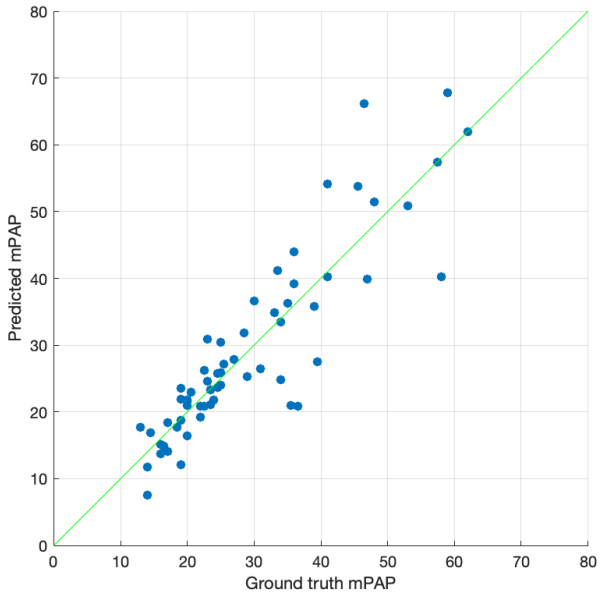

(c) Final prediction vs Ground truth

Figure 8.10: mPAP computation result

estimates of the pressure metric. The upper-level estimate is then used to classify each subject into one of three subgroups of different ranges of pressure: low, mid, and high. The lower level consists of three multiple linear regression models for the subgroups.

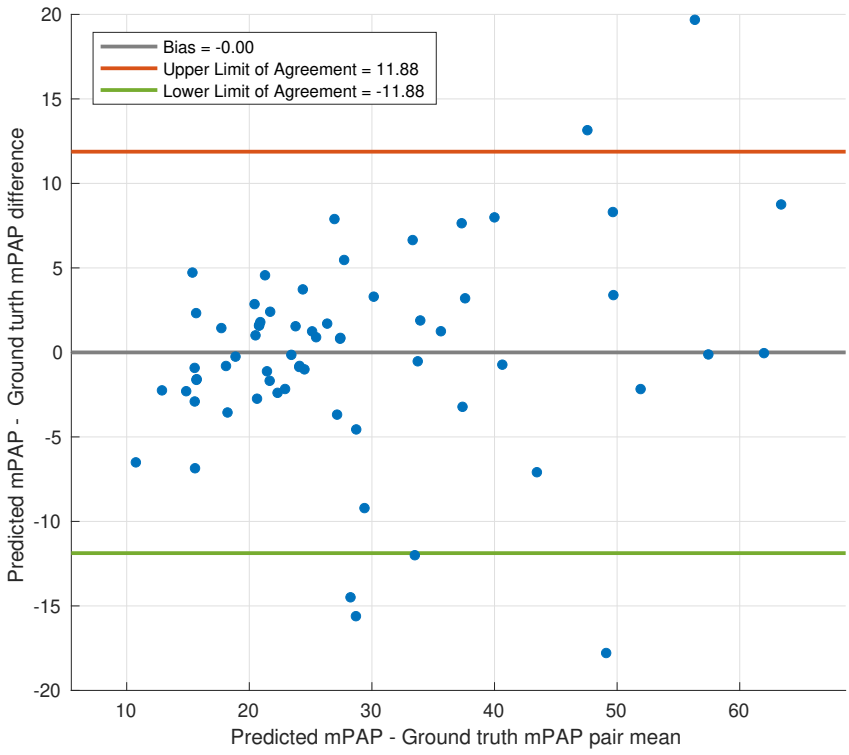

Figure 8.11: Bland-Altman plot of predicted mPAP and ground truth mPAP comparison

Misclassification at the upper level propagates to the lower level and may lead to a large error if not handled properly. Thus, we introduce a novel concept of the bridge level, which handles the subjects whose upper-level estimate is near the boundaries between the subgroups. This additional level demonstrates improvement of classification accuracy. We have also developed further strategies to handle potentially misclassified boundary cases. Firstly, the training data for each lower-level model overlaps with its neighboring subgroup. Secondly, a weighted combination of the outputs of the lower-level models is computed as the final output. Lastly, the upper-level and lower-level predictions are compared. If the difference between them is large, the lower-level prediction is not trusted, and thereby the upper-level prediction is used as the final prediction.

A 2-stage bivariate outlier detection method has been developed for robust training of the multiple linear regression models, which are sensitive to outliers. The first stage detection

is based the Mahalanobis distance and may result in false positives because the data is not normally distributed. The second stage detection is based on the standardized residual computed from linear regression on the data excluding the outliers detected at the first stage. The second stage effectively resolves the false positives from the first stage.

The presented method has been evaluated with the OHSU trial dataset. Bland-Altman analysis on the predicted PCWP and the RHC PCWP yields a bias of 0 and 95% limits of agreement of ± 4.76 mmHg. Same analysis on the predicted mPAP and the RHC mPAP yields a bias of 0 and 95% limits of agreement of ± 11.88 mmHg.

CHAPTER 9

Signal Quality Assurance

ECG and PCG signals are sensitive to noise. Noisy signals may lead to inaccurate feature extraction as the waveform morphology or spectrum may be altered. Thus, high quality signal is crucial to accurate computation of the pressure metrics. In order to acquire high quality signals, it is best to record signals in a quiet controlled environment with the patient remaining still throughout the measurement. However, clinical environments often have substantial amount of noise from various sources including vehicle traffic, conversations, and medical equipment [31]. In addition to these environmental noises, measurement can be also disturbed by body movement, coughing, talking, and heavy respiration. Furthermore, suboptimal application of the sensors may result in deficient signal quality.

During the clinical trials, we have observed several cases of low quality signals due to various reasons. While the subjects were instructed to remain still and silent during the recordings, few subjects tried to use their smartphones. A subject during such an activity may have not only generated movement of tissues that are coupled with the sensors but also contacted the cables that are connected to the sensors, thereby disturbing the sensors. Other noise-inducing activities such as talking have been observed. Besides reduced signal quality due to significant amount of noise, poor sensor coupling has been also observed for some male subjects with a substantial amount of chest hair, which potentially prevents the acoustic sensors from being flush with the skin.

The early clinical trials for data acquisition to initiate the development of this hemodynamics assessment system required a real-time signal quality monitoring by a trained operator who is familiar with the signal characteristics of both ECG and PCG. To enable

the real-time monitoring, a data acquisition software system was developed to display the signals on the patient monitor screen in real time for the operator to monitor the signal quality. Manual monitoring had been feasible for these clinical trials because its purpose was only to ensure enough data with sufficient signal quality was acquired per measurement. However, manual monitoring is unfit for real-time hemodynamics assessment. In order to support such assessment, the signal quality must be continuously monitored, and the low quality segments must be rejected in real time. Moreover, the signal quality assessment must have minimal intra- and inter-operator variability to ensure reproducible computation of the pressure metrics.

We have developed fully automated algorithms for signal quality assessment to reject low quality signal segments. This chapter includes three parts, each describing an algorithm developed for each specific signal type: ECG, audible PCG, and low-frequency PCG. In Section 9.1, we discuss various sources of noise in ECG signals and describe a machine learning method for ECG signal quality assessment. In Section 9.2, we discuss various causes of low quality in PCG signals and describe an algorithm to assess the signal quality of audible PCG. We also describe an additional method to assess the signal quality of the low-frequency components of PCG signals as high signal quality in audible PCG signals does not guarantee high signal quality in the corresponding infrasonic and subliminal components.

9.1 ECG Signal Quality Metric

9.1.1 Introduction

As described in Chapter 5, ECG signals may include various types of noises such as baseline wanders, EMG noises, electrode motion artifacts, and powerline interference. Generally, noise from these sources is sufficiently removed via appropriate filtering. However, the frequency range of the noise overlaps with that of the ECG features [72][51]. Thus, noise removal via filtering may not be effective in some cases where filtered signals retain significantly distorted waveforms due to noise, leading to inaccurate identification of features such

as the QRS complex. In addition to noise, suboptimal application of electrodes may lead to poor signal quality.

Accurate heartbeat segmentation via the algorithm presented in Chapter 5 requires precisely detected reference points in the ECG signal. Therefore, ensuring high quality ECG signals is crucial to accurate heartbeat segmentation and the subsequent signal analysis. Although it is best practice to minimize noise during recordings, such precautions alone cannot prevent noisy signals. Figure 9.1 is an example of noisy ECG signals from our carefully conducted clinical trials. Therefore, it is important to have a capability to automatically

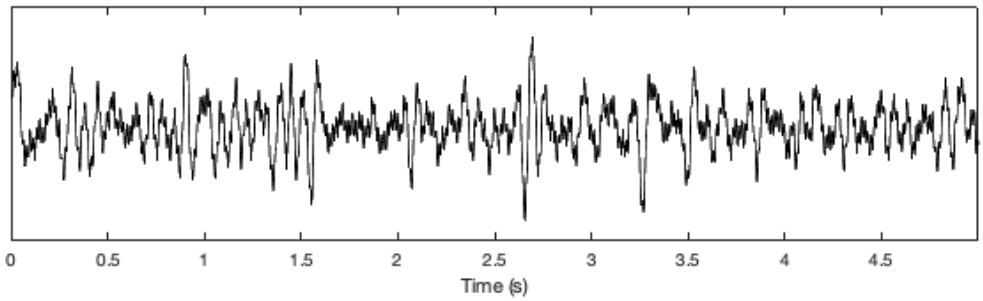

Figure 9.1: Noisy ECG signal from clinical trial

detect and discard low quality signals.

Various methods have been proposed to assess ECG signal quality. In general, there are two stages of ECG signal quality assessment. The first is to develop signal quality indices (SQI) that correlate with ECG signal quality. The second stage incorporates a machine learning algorithm to train a classifier with several signal quality indices as the features to classify the signal quality.

Some of the commonly utilized characteristics of ECG signals reflected in several proposed SQIs are signal complexity, periodicity, energy distribution. [124] and [125] propose and investigate multiscale entropy and Lempel-Ziv complexity [70] as SQIs that measure the complexity of the ECG signal and demonstrated their sensitivity to SNR. [96] investigates autocorrelation function as an SQI to assess the signal periodicity along with several other SQIs. [28] and [71] investigate relative powers in QRS complexes and signal baselines

as SQIs to characterize spectral energy distribution. [36] also investigates energy distribution as SQIs that are derived by joint-time frequency analysis of the raw ECG signal. Other commonly investigated SQIs include moments such as kurtosis and skewness [96][28][71], amplitude features derived from R peaks [36][53], R-R interval variability [84][53], and Shannon entropy [85].

Commonly used classification methods for ECG signal quality include decision rules [96][68] [36], SVM [28][71][85], and ANN [28][123]. In the decision rule approach, a set of conditions with threshold values for SQIs is used to determine whether the ECG signal quality is acceptable. SVMs are supervised learning models commonly used for classification. An SVM constructs a hyperplane that optimally divides different classes of data points in a high dimension feature space. For ECG signal quality assessments, a set of SQIs are used as features to train an SVM model that classifies the signal quality. An ANN is another popular algorithm for ECG signal quality classification. It can also be trained with a set of SQIs as the features. Such approach is investigated in [28]. Another approach is a deep learning technique where the features are not manually designed, but rather they are extracted by an ANN model. Such approach is implemented in [123] wherein a cascaded convolutional neural network model that extracts features from spectrograms of ECG signals and pre-processed signals.

We have developed five SQIs as features and an SVM model to effectively classify ECG signal quality. The SQIs are based on signal characteristics such as periodicity, complexity, segmentability, and spectral information. In the subsequent subsections, we detail the methods for data labeling, SQI development, and classifier design and describe the results of the proposed methods.

9.1.2 Methods

While ECG signal quality assessment is typically used to determine the signal interpretability, the main purpose of our proposed methods is to ensure reliable detection of reference points for the heartbeat segmentation algorithm presented in Chapter 5. Thus, acceptable ECG

signal quality is defined as quality of a signal that has clearly identifiable reference points without noise features that can be falsely identified as reference points. In addition, baseline wander or high-frequency noise that can be removed via filtering does not contribute to the signal quality. In other words, the quality of a clean signal with removable noise is considered to be acceptable. Examples of acceptable signal and unacceptable signal are shown in Figure. As with the other ECG signal processing methods presented in this dissertation, the ECG

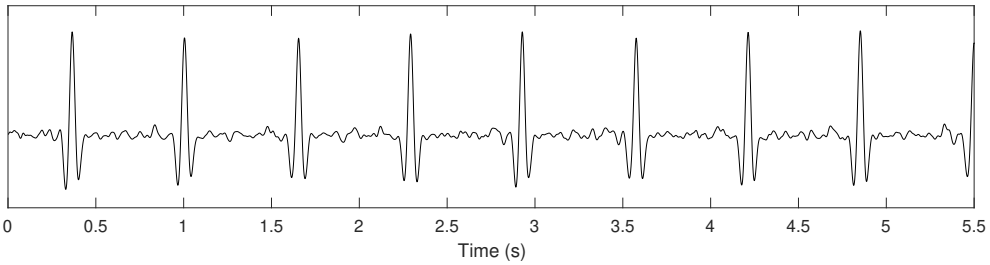

(a) Acceptable

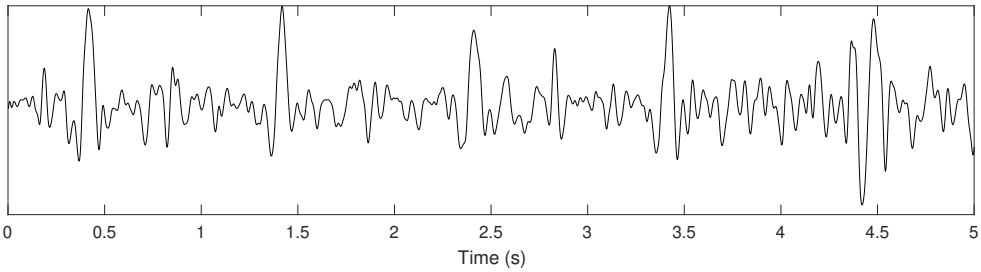

(b) Unacceptable

Figure 9.2: Examples of acceptable and unacceptable ECG signal qualities

signal quality assessment is performed per each 10-second signal segment. We have selected 9281 of 10-second segments from the UCLA and OHSU trial datasets to train and validate our method. Their signal qualities have been manually labeled as acceptable or unacceptable according to the definition of acceptable quality.

Five features have been developed that correlate with the ECG signal quality: *correlation score*, *RMSE score*, *symbolic entropy*, *high-frequency average power*, *ECG reference point consistency*. A summary of these features is provided in Table 9.1, and detailed description of each feature is provided in the following paragraphs. As described above, removable noise

Feature Name	Description
Correlation score	Similarity among heartbeat segments
RMSE score	Difference between each of heartbeat segments and their averaged waveform
Symbolic entropy	Complexity of ECG signal
High-frequency average power	Average power in high frequency range
ECG reference point consistency	Consistency of the detected reference points for heartbeat segmentation

Table 9.1: ECG signal quality features

is not considered for quality assessment. Thus, these features are computed from signals that have been filtered via a bandpass filter with cutoff frequencies at 0.5 and 40 Hz.

The *correlation score* feature is based on the waveform similarity among the heartbeat segments within each 10-second ECG signal. Such similarity indicates the periodicity of the signal. As described above, periodicity is a commonly utilized characteristic of ECG signals for quality assessment. The assumption for this is that morphological features in a clean ECG signal reflect certain cardiac events that repeat every heartbeat. However, noise does not periodically occur per heartbeat. Thus, signals with high SNR are likely to have strong periodicity. The steps to compute this feature are as follows.

1. Heartbeat segmentation is performed on the 10-second filtered ECG signal as described in Chapter 5.

2. The Pearson correlation coefficient between every pair of the heartbeat segments is computed as follows.

$$\rho(x_1, x_2) = \frac{cov(x_1, x_2)}{\sigma_{x_1}\sigma_{x_2}} \tag{9.1}$$

where $\rho(\cdot)$, $cov(\cdot)$, and σ denote correlation coefficient, covariance, and standard deviation respectively.

3. The mean of the correlation coefficients computed in Step 2 is the *correlation score* feature.

Similarly, the *RMSE score* feature quantifies the waveform similarity among the heartbeat segments. The idea behind this feature is that each segment of a periodic feature will not differ from the average of all segments in terms of amplitude. Such amplitude difference is computed as the root means square error (RMSE). The steps to compute this feature is as follows.

1. Heartbeat segmentation is performed on the 10-second filtered ECG signal.
2. The amplitudes of heartbeat segments are normalized by a normalization factor that is computed as the median of the heartbeat segments' maximum magnitudes.
3. The ensemble average of the normalized heartbeat segments is computed.
4. For each segment, the RMSE between it and the ensemble average is computed.
5. The mean of the RMSEs computed in Step 4 is the *RMSE score* feature.

While signal periodicity can generally characterize signal quality, other signal characteristics are needed to assess the signal quality more accurately. For instance, arrhythmic conditions such as bigeminy may lead to less periodic signal waveforms even in the absence of noise.

The *symbolic entropy* feature is derived from [15], which investigated complexity of physiological signals, particularly human gait stride intervals, in comparison to noisy signals via symbolic entropy. The computation of symbolic entropy involves two stages: 1) symbolization and 2) Shannon entropy computation. The procedure for this computation is detailed below.

1. The filtered ECG signal is normalized such that the maximum amplitude equals 1.
2. The normalized signal is converted to a binary sequence as follows.

$$s(i) = \begin{cases} 1 & \text{if } |x(i)| > \overline{|x|} \\ 0 & \text{otherwise} \end{cases} \tag{9.2}$$

where $s(i)$, $x(i)$, and $\overline{|x|}$ denote the i^{th} element of the binary sequence, that of the normalized signal, and the mean of the absolute values of the normalized signal respectively.

3. The binary sequence is converted into a sequence of 4-bit words such that

$$w_j(k) = s(4j + k - 4) \tag{9.3}$$

where $w_j(k)$ denotes the k^{th} bit of the j^{th} word in the sequence.

4. For each word, the probability of its occurrence is computed to construct a sequence of such probability $P(j)$.

5. The symbolic entropy E is then computed as follows.

$$E = -\sum_j P(j) log_2 P(j) \tag{9.4}$$

The *high-frequency average power* feature is based on the average power in high frequency range of the ECG signal. According to the investigation of the spectra of ECG signals and various types of noise in [111], the relative power of ECG features gradually decreases beyond 10 Hz while the relative power of muscle noise is relatively constant beyond 10 Hz. Thus, the average power in the higher frequency may correlate with the level of muscle noise. The steps to compute this feature is as follows.

1. The power spectral density (PSD) is computed for the filtered ECG signal.

2. From the PSD, *high-frequency average power* feature value is computed as the average power between 15 Hz and 40 Hz.

The last feature is *ECG reference point consistency*. The idea behind this feature is that the reference point detection algorithm is likely to have higher accuracy for clean signals than for noisy signals. Accurately detected reference points in clean signals are likely to be consistent. Such consistency is measured by the variability in the R-R intervals computed with the detected reference points as substitutes for the R peaks. While arrhythmic ECG

signals may also exhibit high R-R interval variability, falsely identified reference points may significantly contribute to increased variability. Furthermore, if the detection algorithm fails to identify certain beats, the resulting R-R interval is substantially large. This feature is computed as follows.

1. The reference points are obtained with the detection algorithm presented in 5.
2. The intervals between two consecutive reference points are computed.
3. The standard deviation of the computed intervals is the ECG reference point consistency feature value.

For training and validating a classifier, the features are extracted from the 9281 selected ECG signals. Subsequently, the extracted feature values are standardized by dividing them by their standard deviations and subtracting their means. Equal number of data points from each class, in this case acceptable or unacceptable, are randomly selected as the training data for an SVM model. The remaining data is used to validate the trained classifier.

By definition, an SVM constructs a hyperplane, which is a linear subspace of the feature space, that optimally divides data points of different classes in the feature space. However, scatter plots of the data points with the signal quality features as the axes indicate that a linear hyperplane is not ideal for diving the data points of the different classes. Thus, the kernel trick is employed to enable non-linear classification. For this, an SVM model with the radial basis function kernel is used.

9.1.3 Results

Figure 9.3 demonstrates the effectiveness of each ECG signal quality feature as an SQI. The correlation score tends to be greater for the signals with acceptable qualities. There are several outliers for the acceptable quality signals whose correlation scores are low. Most of these outliers exhibit clear QRS complexes with noisy TP segments. Since reliable heartbeat segmentation depends on the signal quality for the QRS complexes rather than the TP

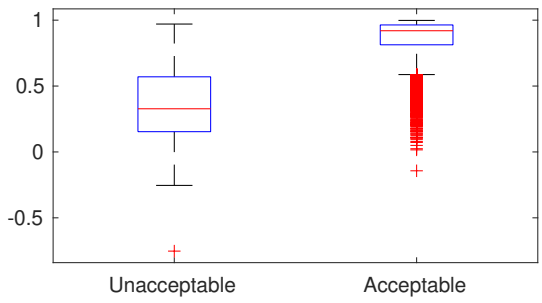

(a) Correlation score

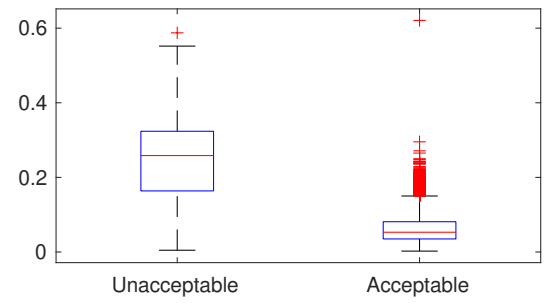

(b) RMSE score

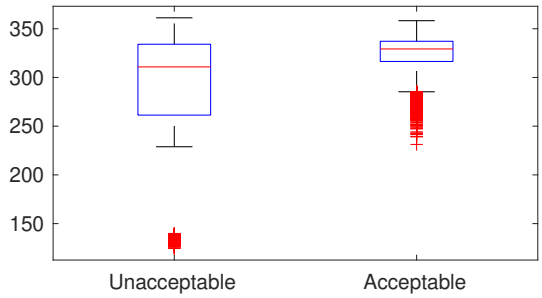

(c) Symbolic entropy

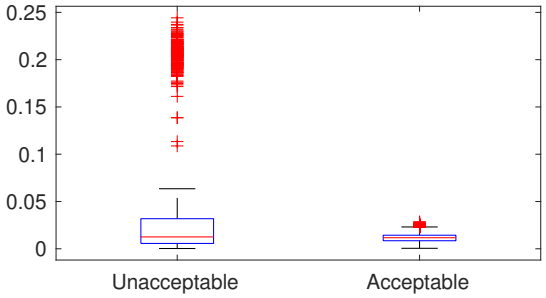

(d) High-frequency average power

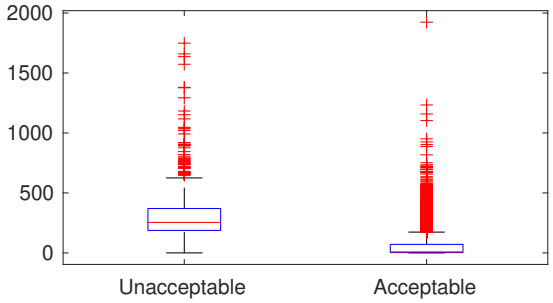

(e) ECG reference point consistency

Figure 9.3: Box plots of ECG signal quality features

segments, these outliers have been labeled as acceptable while the correlation coefficients between the heartbeat segments are deficient due to the less periodic TP segments. Several signals with unacceptable quality have high correlation scores. In such signals, most of the heartbeat segments show highly periodic waveforms with substantial noise during only a short subsegment of the signal. The correlation score reflects the overall similarity among the heartbeat segments, and thereby noise in short duration has an insignificant impact. However, such noise leads to failure in heartbeat segmentation for the heartbeats around the

noise.

The RMSE score tends be greater for signals with unacceptable quality. As with the correlation score, the RMSE score correlates with the similarity between the heartbeat segments. However, unlike the correlation score, the noise in TP segments have less impact on the RMSE score due to its relatively small amplitude and thereby small contribution to the RMSE. The RMSE is mainly affected by the similarity between prominent features such as the QRS complex. The outliers among the acceptable quality signals that have large RMSE scores have few irregular QRS complexes such as PVC, which contributes to large RMSE.

The symbolic entropy tends to be greater for acceptable signals. This result is consistent with the finding in [15] where physiological signals of striding intervals have higher signal complexity quantified by symbolic entropy than random signals.

As described above, the average power in the higher frequency band is expected to increase with presence of muscle noise. The box plot indicates that the unacceptable quality signals tend to have greater high-frequency average power. Unacceptable quality signals with low high-frequency average power typically exhibit characteristics of noise sources other than high-frequency muscle noise.

The last feature, the ECG reference point consistency, tends to be larger in the unacceptable quality signals. There are a number of outliers among the acceptable quality signals. Several of them exhibit arrhythmic patterns while many others are clean normal signals. In the latter case, the ECG reference point detection algorithm either fails to identify certain points or falsely identifies other features as the reference points.

The SVM-based classifier trained with the features above yields an accuracy of 94.9% on the validation data and the confusion matrix in Table 9.2. Given the acceptable quality label is the positive class, the sensitivity and specificity are 94.8% and 96.0% respectively. Among the 24 false positives, 9 cases seem to be borderline cases. On the other hand, among the 389 false negatives, most cases seem to be borderline cases. In the latter cases, the signals have substantial level of noise while the QRS complexes are clear enough for accurate identification. If the signal interpretability was the criterion for quality labeling, most of the

		Actual		
		Unacceptable	Acceptable	Total
Predicted	Unacceptable	579	389	968
	Acceptable	24	7025	7052
	Total	603	7417	8020

Table 9.2: Confusion matrix of ECG signal quality classification result

false negatives would have been labeled unacceptable, making them true negatives. However, the definition of an acceptable quality signal here is a signal where accurate heartbeat segmentation is feasible.

9.2 PCG Signal Quality Metric

9.2.1 Introduction

PCG records vibrations of the chest wall using a microphone, which captures such vibrations with mechanical motion of its diaphragm. As such, it is susceptible to not only undesired non-cardiac sound but also mechanical disturbances. Although the noise suppression via spectral subtraction as described in Chapter 6 has been generally effective, PCG signals with heavy noise corruption may remain in low quality even after denoising. Furthermore, poor sensor coupling may result in low SNR. Low quality PCG signals may result in inaccurate computation of PCWP and mPAP. Thus, it is critical to detect and reject low quality signals.

In this section, we describe an automated algorithm we have developed for assessment of the PCG signal quality. Since the measure of PCG signal quality is subjective, labels from three individuals were combined to generate the ground truth. We developed features that correlate with the signal quality. A classifier based on SVM has been trained with the features to predict the signal quality.

9.2.2 Methods

In order to develop features and subsequently train a signal quality classifier, ground truth labels for the signal quality are required. A large set of 10-second PCG segments with a wide range of signal quality has been selected from the UCLA trial dataset. Using the ECG-based heartbeat segmentation, the selected PCG signals are segmented into each heartbeat. Subsequently, each segment's signal quality has been manually inspected to establish the ground truth. As described above, PCG signal quality measure is subjective. Thus, we have obtained manual labels from three individuals who participated in the clinical trials and monitored the signal quality. Each individual has assigned a numeric value indicating the signal quality to each heartbeat segment: 1 for low, 2 for medium, and 3 for high. The average value of the three numeric labels from three individuals for each segment is computed. Subsequently, the average values are converted into 5 classes of signal quality. Variability in the manual labels among the three individuals is discussed later in Subsection 9.2.4.

Based on the criteria used to determine the PCG signal quality, we developed five numerical features that correlate with the signal quality: *maximum cross-correlation*, *RMS ratio*, *peak-to-noise ratio*, *envelope model error*, and *mean likelihood*. A summary of these features is provided in Table 9.3, and detailed description of each feature is provided below.

Feature Name	Description
maximum cross-correlation	Similarity among consecutive heartbeat segments
RMS ratio	Ratio between RMS of pre-denoised signal and that of denoised counterpart
peak-to-noise ratio	Ratio between heart sound amplitude and noise floor
envelope model error	Similarity to a generic signal model
mean likelihood	Likelihood of signal being a cardiac signal

Table 9.3: PCG signal quality features

The *maximum cross-correlation* feature is based on the similarity between a heartbeat

segment and other segments. High quality signals generally exhibit strong periodicity. As such, a heartbeat segment with low noise level and high-amplitude heart sound events is likely to have a similar waveform to its neighboring segments. Such similarity is characterized by cross-correlation. If two signals are similar, the cross-correlation function results in strong constructive addition and an elevated peak in the cross-correlation. If the segment is characterized by low SNR, the similarity between it and other segments is reduced, resulting in reduced amplitude of such a peak in the cross-correlation. The steps to extract this feature are as follows.

1. The PCG signal is denoised via bandpass filtering and spectral noise suppression as described in Chapter 6.

2. An envelope signal is computed for each heartbeat segment.

3. Cross-correlation is computed for every pair of the per-segment envelope signals.

4. The amplitude of the most prominent peak in every cross-correlation sequence is measured. If there are 10 heartbeats, for example, each heartbeat has 9 cross-correlation peak amplitude values that are computed in combination with the other 9 heartbeats.

5. The *maximum cross-correlation* feature is computed as the maximum of these 9 amplitude values.

The *RMS ratio* feature is based on the noise level. The idea behind this feature is that the overall amplitude of a noisy signal decreases after noise suppression while the change in overall amplitude of a high quality signal is relatively smaller. The steps to compute this feature are as follows.

1. A bandpass filter with cutoff frequencies at 25 Hz and 150 Hz is applied to the raw PCG signal.

2. Subsequently, noise suppression is applied to the filtered signal.

3. The root mean square (RMS) value is computed for each heartbeat segment from a pre-denoised filtered signal

4. Similarly, the RMS value is computed from the denoised signal.

5. For each heartbeat segment, the *RMS ratio* feature is computed as ratio of the corresponding RMS values from steps 3 and 4.

The idea behind the *peak-to-noise ratio* feature is that a high quality PCG signal generally has prominent S1 and S2 relatively to the overall signal noise floor. The steps to compute this feature are as follows.

1. The PCG signal is bandpass-filtered and subsequently denoised via noise suppression.

2. The envelopes are computed for both the pre-denoised bandpass-filtered signal and the corresponding denoised signal.

3. The peak amplitudes of the S1 and S2 in the envelope of the denoised signal are computed. Let us suppose these are denoted by $A1$ and $A2$ respectively.

4. The noise floor is computed as the 20th percentile of the envelope of the pre-denoised bandpass-filtered signal. Let us suppose the noise floor is denoted by n.

5. The peak-to-noise ratio is computed as $\frac{A1+A2}{n}$.

The *envelope model error feature* is based on the difference between the envelope of the signal and a generic model of a high quality signal envelope. In order to generate the envelope model, generic envelopes for high quality S1 and S2 are created and combined. For this, we selected a large number of high quality S1 and S2 segments from the UCLA trial dataset. Subsequently, the envelopes of the selected S1 and S2 segments are generated. The average of the S1 segment envelopes is the generic envelope for high quality S1. The generic high quality S2 envelope is acquired similarly. The following are the steps to generate the model envelope of a signal using the generic S1/S2 envelopes and compute the feature value.

1. The PCG signal is bandpass-filtered and denoised.

2. S1 and S2 are detected from the signal.

3. The envelope of the denoised signal is computed.

4. For each of the detected S1 and S2, its peak amplitude and location are determined.

5. The generic S1 envelope is scaled and shifted according to the peak amplitude and location of each S1. Similarly, the generic S2 envelope is scaled and shifted.

6. The noise floor is computed as it is for the *peak-to-noise ratio* feature.

7. The scaled and shifted generic S1 and S2 envelopes and the noise floor are combined to generate a model envelope for the signal.

8. The *envelope model error* is computed as the mean square error between actual envelope signal and the generated model.

The last feature is the *mean likelihood*, which depends on the likelihood of the signal being a cardiac signal. The signal likelihood is derived from the STSA-log-MMSE noise suppression method presented in [87]. The likelihood is computed for each frequency bin of the signal. The mean of the likelihood values between the 40th percentile and the 90th percentile is computed. The likelihood exponentially increases as the signal quality increases. Therefore, the log of the mean value is computed as the mean likelihood feature value.

An SVM-based classifier is implemented to predict the PCG quality based on these five inputs. Since an SVM is a binary classifier, an error-correcting output codes model is used to implement a multi-class classifier, which codes each class into a unique binary string and trains an SVM for each digit [37].

9.2.3 Low-frequency PCG Signal Quality Metric

The low-frequency components of PCG signals are sensitive to mechanical noises due to motion or sensor disturbance. Significant mechanical noise may not only affect the low-

frequency components but also high-frequency components. In the presence of such noise, the quality of the PCG signal may be classified as low by the PCG quality classifier described above and effectively rejected before the subsequent pressure metric computation. However, there might be low-frequency noise that do not affect the quality of the audible components of the PCG signals. Conversely, there is also high-frequency noise such as speech that may only affect the audible components while the low-frequency components remain in high quality. Furthermore, the energy in low-frequency range is greater as discussed in Chapter 6. Therefore, what appear to be a weak signal in the audible range may have clean low-frequency components.

In other words, PCG signals must be in high quality in both audible and low-frequency range in order to accurately identify cardiac events and extract features. Thus, another layer of quality assurance is needed to reject signals with low frequency noises that are not present in the audible PCG domain. As discussed in Chapter 6, the low-frequency components of PCG signals are highly periodic given sufficient signal quality. Therefore, signal periodicity effectively reflects the signal quality of the low-frequency PCG.

In order to assess the periodicity of the low-frequency PCG signal, a numeric score is computed. The periodicity score is computed similarly to the ECG SQIs that characterize the signal periodicity as follows.

1. The low-frequency components of the PCG signal is acquired via DWT.
2. The resulting signal is segmented using the ECG reference points.
3. Time warping is performed to time synchronize the PCG segments.
4. The correlation score and the RMSE score are computed following the same method for the ECG correlation and RMSE scores.
5. The periodicity score is computed as $score_{correlation} - 0.8 \times score_{RMSE}$.

9.2.4 Results

We have observed high variability among the manual labels from the three annotators. PCG signal quality is subjective, and the borderline cases are often labeled differently. Among the 3672 labeled heartbeat segments, only 794 of them have identical labels from all three annotators. One annotator has more liberal criteria for labeling. Another one has strict criteria. The other one has an intermediate strictness. The distribution of the labels by each annotator is illustrated in Figure 9.4.

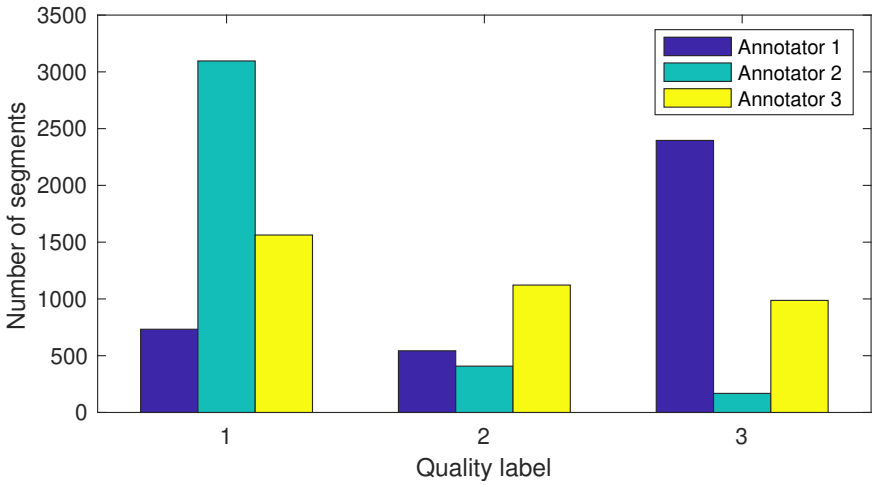

Figure 9.4: Distribution of the annotated quality labels

Figure 9.5 shows box plots of the PCG quality features. Many of these features have large overlaps among the different classes. Thus, using each of these features as a single SQI to determine the PCG signal quality will not be effective. However, combination of these features in higher dimension yields better separation among the classes. For example, Figure 9.6 illustrates the labeled data points in 3-dimensional space with three least effective features as its basis vectors.

The dataset of the labeled heartbeat segments is randomly divided into training and evaluation sets. The training set is balanced by including the equal number of data points from each quality class. The classification result of the trained SVM-based classifier on the evaluation data yields the confusion matrix in Table 9.4. The confusion matrix demonstrates

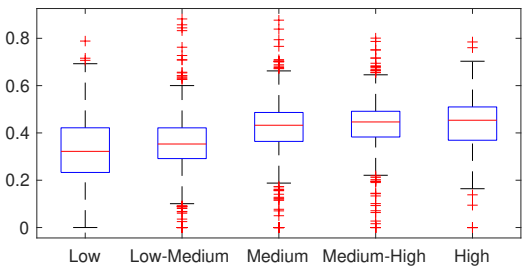

(a) maximum cross-correlation

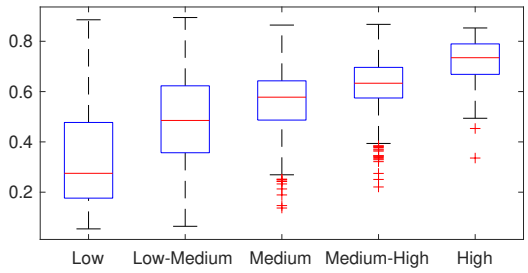

(b) RMS score

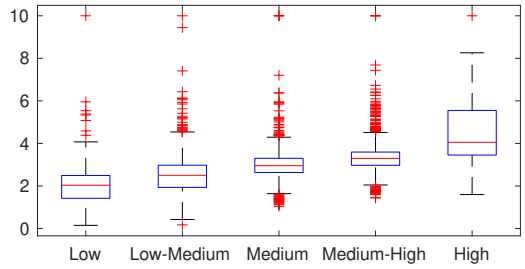

(c) peak-to-noise ratio

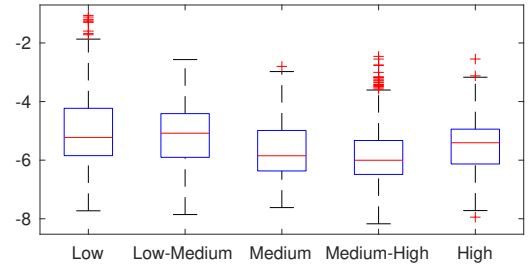

(d) envelope model error

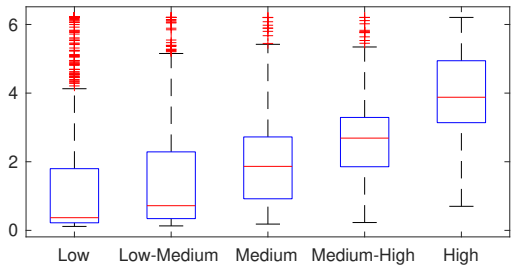

(e) mean likelihood

Figure 9.5: Box plots of PCG signal quality features

the effectiveness of the classifier. Misclassification from low and low-medium to medium-high and high or vice versa is infrequent. Considering the subjective nature of PCG signal quality, misclassification into the neighboring classes is acceptable.

As for the low-frequency PCG signal quality, the periodicity score has demonstrated effective representation of the signal quality. Figure 9.7 shows examples of low-frequency signals with various scores. Each plot shows superimposed heartbeat segments to illustrate the periodicity of the segments. The top plot is a high quality signal that clearly demonstrates highly periodic morphology. The periodicity score is computed to be 0.62 for this signal.

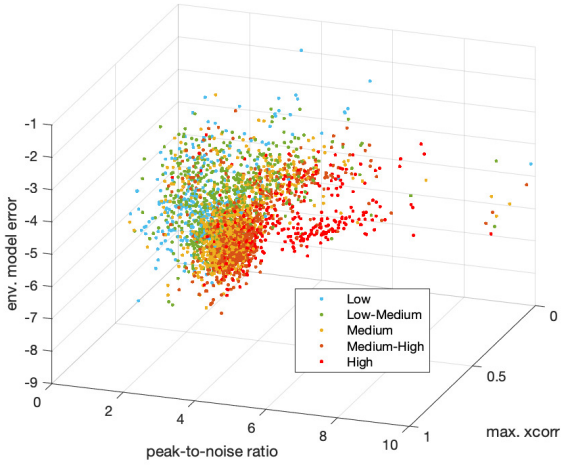

Figure 9.6: Combination of PCG quality features: maximum cross-correlation, peak-to-noise ratio, and envelope model error.

		Actual					
		L	LM	M	MH	H	Total
Predicted	L	336	280	43	10	3	672
	LM	99	275	112	54	12	552
	M	13	105	200	91	12	421
	MH	1	22	129	215	59	426
	H	0	10	8	36	86	140
	Total	449	692	492	406	172	2211

Table 9.4: Confusion matrix of PCG signal quality classification result. L: low, LM: low-medium, M: medium, MH: medium-high, H: high

The middle plot shows a medium quality signal. While periodicity is reduced due to presence of noise, the morphological characteristics are identifiable. We regard signals in this quality acceptable as the ensemble averaging method presented in Chapter 6 is capable of sufficient suppression of moderate noise. The periodicity score for this particular example is computed to be 0.37. The bottom plot shows a low quality signal that is significantly distorted by noise. Only during the S1, the signal demonstrates some periodicity. We regard signals in

this quality unacceptable. The periodicity score for this example is computed to be -0.01. In our system, signals with the periodicity score below 0.1 are considered unacceptable and

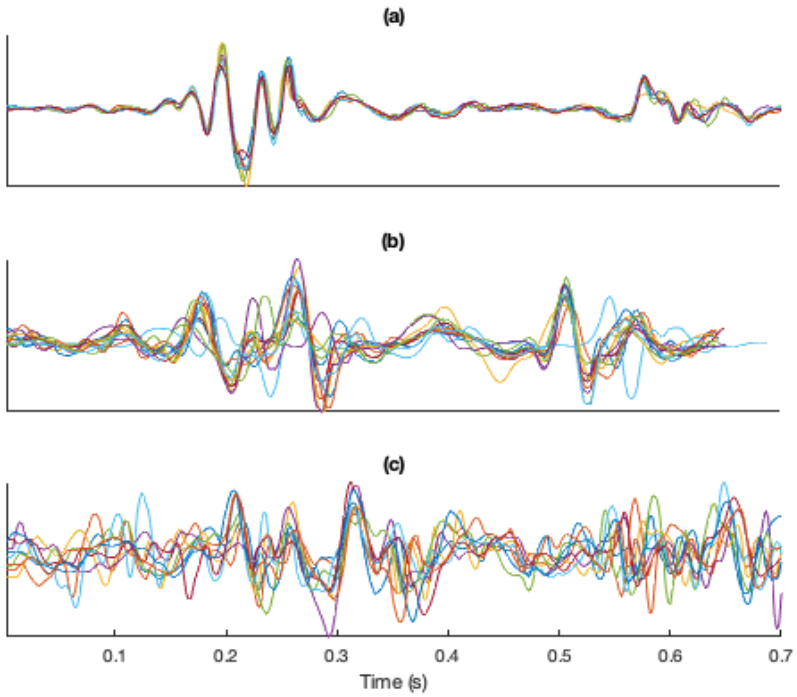

Figure 9.7: Superimposed heartbeat segments of low frequency PCG signals with various periodicity scores. a) periodicity score: 0.62 b) periodicity score: 0.37 c) periodicity score: -0.01

removed from further analysis.

9.3 Summary

In this chapter, new methods for ECG and PCG signal quality assurance are proposed. Signal quality is critical to accuracy of the signal processing methods and feature computation. Thus, we have developed signal quality assessment methods for all signals used in the presented signal processing and feature computation: ECG, audible PCG, and low-frequency PCG.

ECG signal quality is determined according to the segmentability. That is, signals are

considered acceptable if the reference points for heartbeat segmentation are clearly identifiable. We have developed five features that are consistent with signal quality and an SVM classifier. The classifier has been evaluated with 8020 signal segments with annotated signal quality, yielding an accuracy, sensitivity, and specificity of 94.9%, 94.8%, and 96.0% respectively.

PCG signal quality is subjective. Thus, the data has been annotated by three individuals who participated in the clinical trials to monitor the signal quality. High variation in the annotated labels among the annotators is observed. The annotations are combined to form 5-class ground truth labels. Five features have been developed to train an SVM-based classifier. The classifier has been evaluated with 2211 signal segments. The resulting confusion matrix demonstrates effective classification.

Low-frequency PCG signal quality is highly associated with signal periodicity. We have developed a periodicity score based on the correlation among heartbeat segments and the RMSE between each heartbeat segment and the ensemble average of several consecutive heartbeat segments. The periodicity score demonstrates effective assessment of the low-frequency PCG signal quality.

CHAPTER 10

Application for Systolic Time Interval and Ejection Fraction

Left ventricular ejection fraction or simply ejection fraction (EF) is an important metric to assess heart failure. It is the fraction of the blood ejected from the left ventricle per contraction and calculated as $\frac{EDV-ESV}{EDV} \times 100$ where EDV and ESV refer to the end-diastolic volume and end-systolic volume. EF is a critical cardiac function metric that indicates the efficiency of the heart in pumping the blood to the body. According to American Heart Association, normal EF is between 50% and 70%; borderline EF is between 41% and 49% wherein an individual may show symptoms during activities; and reduced EF is less than or equal to 40% wherein symptoms may be shown even at rest [5].

There are several clinical methods to measure EF including echocardiography, magnetic resonance imaging, computerized tomography, and ventriculography. As with RHC for PCWP and PAP measurements, these methods require expensive equipment as well as professionally trained experts to operate. As an extension to our mission of developing a fully automated non-invasive system for PCWP and mPAP assessment, we have investigated an application for EF assessment where we examine non-invasive features from ECG and PCG signals.

The systolic time interval (STI) has been studied as a non-invasive measure of the left ventricle performance, particularly EF. As the name suggests, STI are time intervals observed during the systole. The STI consists of the pre-ejection period (PEP) and left ventricle ejection time (LVET). PEP is defined as the time interval between the onset of ventricular depolarization and the onset of ventricular ejection, and it typically measured as the time

delay between the Q wave in ECG and the subsequent aortic valve opening. LVET is defined as the time interval between the aortic valve opening and the aortic valve closure [86]. In their landmark paper, Weissler et al. show that the failing left ventricle is characterized by prolonged PEP and shortened LVET [118]. Therefore, PEP/LVET has been explored as a feature to predict the EF.

In order to compute STI, methods for detection of the onset of ventricular depolarization, aortic valve opening, and aortic valve closure are required. As for the onset of ventricular depolarization, we have developed a flexible data-driven algorithm using clinical data that includes various morphologies and noise. The aortic valve closure is known to be the source of the S2 along with the tricuspid valve closure [61]. Since the aortic valve closure precedes tricuspid valve closure, we can estimate the timing of the aortic valve closure with the onset of S2. On the other hand, the aortic valve opening is typically not observable in conventional PCG. Drawing inspirations from SCG, we investigate a recurring low-frequency PCG event as a substitute for the aortic valve opening event. The following sections describe these methods in more detail.

From the timings of the detected events, PEP and LVET are computed. The computed STI along with PEP/LVET have been evaluated with the UCLA trial dataset, which includes EF values measured with echocardiography, by investigating their correlation with EF. These STI, particularly PEP/LVET, show high correlation with EF.

10.1 Detection of Onset of Ventricular Depolarization

10.1.1 Introduction

As described in Chapter 5, the ventricular depolarization is an electrophysiological event reflected by the QRS complex in ECG signals. Thus, the onset of ventricular depolarization can be detected in ECG signals as the onset of the QRS complex. The challenge in this is variability in the morphology of the QRS complex.

There have been prior studies such as [89][99][41] that present automated STI computa-

tion based on Q wave detection. Although the onset of the Q wave is typically used as the onset of the ventricular depolarization, this requires an ECG signal where the Q wave in each QRS complex is present. In a pathological ECG signal, it is well-known that the Q wave may be absent due to certain conditions [59]. In such cases, PEP computation from the Q wave is not feasible. In the absence of the Q wave, the R wave indicates the onset of ventricular depolarization. As such, the R wave has been proposed as a more robust alternative [23][76]. However, R waves may also be absent due to a variety of conditions [88].

In order to accommodate highly variable ECG morphologies, we propose a flexible algorithm to measure PEP from the first wave in the QRS complex regardless of the wave type as it infers the first sign of ventricular depolarization. In this algorithm, a nonlinear combination of factors that are consistent with the first wave is computed as a weight function whose maximum indicates the first wave.

The algorithm is tested against a clinical ECG dataset that consists of recordings from 97 subjects of our UCLA trials and 47 subjects from the MIT-BIH Arrhythmia Database. The ground truth for the onset of ventricular depolarization in the dataset has been established by a physician who manually inspected the recordings and identified the onset of the ventricular depolarization

10.1.2 Methods

As described, the onset of the ventricular depolarization is indicated by the onset of the QRS complex. Thus, the first step in the algorithm is to identify the QRS complexes using the QRS detection algorithm presented in Chapter 5. As described, the algorithm estimates the onset and end of each QRS complex based on the width of the corresponding peak in the QRS-enhanced signal envelope. The approximate onset of the QRS complex obtained in this way does not precisely indicate the actual onset of initial depolarization, thus necessitating more precise detection of the first wave within each QRS complex.

Once the QRS complexes are identified, the first wave within each QRS complex can be detected as follows. The approximate boundaries of each QRS complex as determined by

the QRS detection algorithm cannot be directly used to isolate the QRS complex in order to find the first wave in the isolated signal. If the isolated signal is too narrow, the Q wave may not be fully captured. If it is too wide, many noise-induced deflections may be captured. As such, a more flexible way to isolate the QRS complexes is needed.

A bell-shaped window such as a Hamming window with relaxed width may seem to solve the issue associated with the rectangular window to isolate the QRS complexes as describe above. However, it introduces another issue that the first wave is significantly attenuated and thereby potentially undetected. Instead, an adjustable window function named Tukey window that combines a rectangular window and a Hanning window is used to allow flexibility. The Tukey window of length L is a rectangular window of length $L(1-\alpha)$ with halves of a Hanning window of length $\alpha/2$ attached to each side where α is the Hanning window fraction as illustrated in Figure 10.1. A Tukey window with $\alpha = 0$ is a rectangular window while a Tukey window with $\alpha = 1$ is a Hanning window. In our algorithm, the

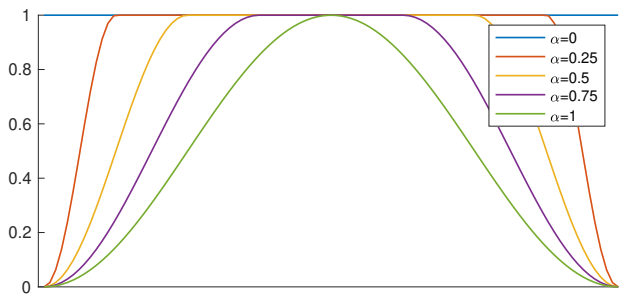

Figure 10.1: Tukey windows with various α

window length is set to 1.3 times the duration of the estimated QRS complex. The value for α is an adjustable parameter that is optimized as described later in this section.

Prior to applying the Tukey window, several operations are performed on the ECG signal to enable more effective detection of the first wave. The first step is to remove potential high-frequency noise and baseline wander with a zero-phase bandpass filter with cutoff frequencies of 0.5 Hz and 40 Hz. Subsequently, two operations are performed in parallel to the resulting filtered ECG signal.

The first operation is amplitude reduction of large waves. Q waves can be substantially smaller in amplitude than the other waves, leading to failed detection of the Q waves. In order to increase the relative significance of the Q wave amplitude, the amplitude of the waves must be normalized. In audio processing, a popular technique called dynamic range compression (DRC) [62] is used to even out the volume level in an audio signal. This technique can be applied to the filtered ECG signal to reduce large amplitude. Figure 10.2a demonstrates an ECG signal before and after DRC.

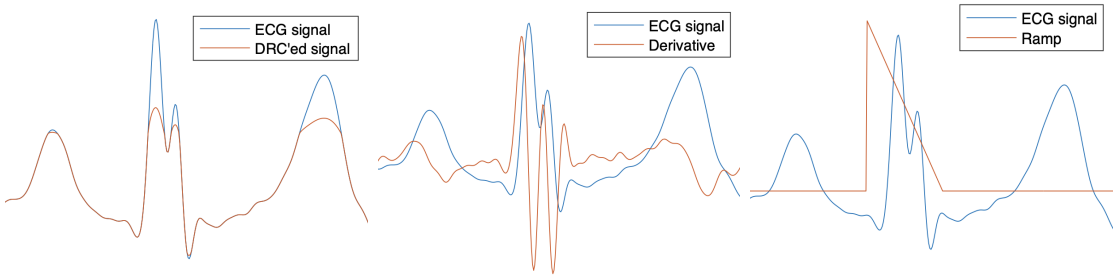

(a) ECG signal before and after DRC

(b) ECG signal and its derivative

(c) ECG signal and descending ramp.

Figure 10.2: Demonstration of operations to enhance the first prominent wave within QRS complex

The other operation is differentiation, which amplifies the QRS complexes as described in Chapter 5. An example of this is shown in Figure 10.2b. Combination of the derivative signal and DRC'ed signal leads to increased relative amplitude of the first wave in the QRS complex. However, direct combination of the two is not feasible as differentiation introduces a phase shift of +90°. Thus, the derivative cannot be directly combined with the DRC'ed signal because these signals are out of phase and may cancel each other when summed. The phase of the derivative is corrected via the Hilbert transform, which produces -90° phase shift for the positive frequency components in the imaginary part of the analytic signal it computes.

Since the algorithm must handle both positive and negative waves, the absolute values of both signals are computed before combining. At each QRS complex, the combined signal

is multiplied by a descending ramp to emphasize earlier peaks within the QRS complex. An exponent is applied to the ramp function to adjust the degree of the emphasis on the earlier deflections. The length of the ramp is set to be identical to that of the Tukey window. Finally, the Tukey window is applied to the resulting signal. The combined signal f can be described in an equation below.

$$f(t) = w(t, \alpha)R^{\beta}(t)(|a(t)| + \gamma|b(t)|)|) \tag{10.1}$$

where w, R, a, and b are the window, ramp, DRC'ed signal, and phase-corrected derivative signal. α, β, and γ are parameters to adjust the Hanning fraction for the Tukey window, impact of the ramp function, and weight on the derivative term. This signal f is a weight function that indicates the location of the first wave such that the time $t*$ that maximizes f indicates the first wave. The deflection whose duration includes $t*$ is detected as the first wave. Figure 10.3 demonstrates the detection of the first wave.

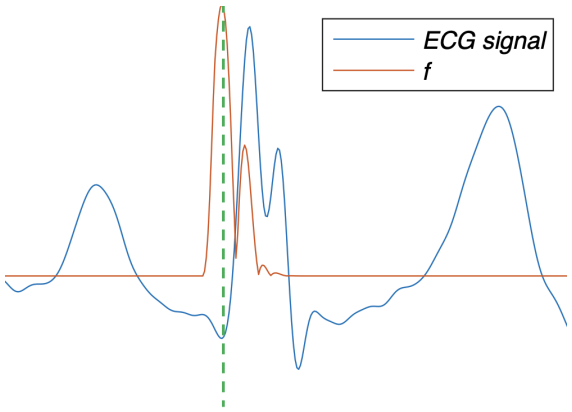

Figure 10.3: The first wave indicated by the maximum of the combined signal

Next, the onset of the first wave is estimated. The first step is to find the peak of the first wave. Subsequently, the second derivative of the signal is computed to introduce +180° phase shift. The peak in this phase-shifted signal that corresponds to the peak of the first wave is approximately at the onset of the first wave in the original signal. A lowpass filter with a cutoff frequency at 20Hz is applied to the ECG signal prior to the second derivative computation in order to avoid undesired extra deflections. Fine search for the onset is

performed in the vicinity of the estimated onset by inspecting the slope and the amplitude of the original signal. Figure 10.4 demonstrates the onset detection.

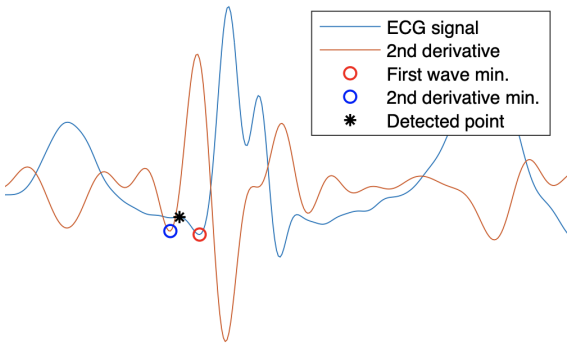

Figure 10.4: The onset of the first wave

The adjustable parameters, α, β, and γ, are optimized to maximize the accuracy of the system. Such optimization was performed using MATLAB's fmincon [2], which is a constrained nonlinear optimization. Given initial values for α, β, and γ to begin the search from and an objective of minimization of the root mean square error between the ground truth and the detected points, the fmincon routine searches for the optimal values for α, β, and γ. Since this is a non-convex problem, fmincon may result in a local minimum. Thus, the fmincon routine is repeated 100 times with a different set of initial parameter values. Figure 10.5 illustrates the parameter optimization.

10.1.3 Results

The method is evaluated with 10-fold cross validation. For the majority of the tested heartbeat segments, the ground truth labels and the automated labels demonstrated nearly perfect agreement. 70.1% of the tested heartbeats yield an error less than or equal to 1.95 ms, which is only one sample time difference in the ECG time series. The distribution of the errors is illustrated in Figure 10.6. The bias, mean absolute error, and standard deviation of error are 1.46 ms, 3.16 ms, and 4.73 ms respectively.

The detection algorithm has demonstrated effective and accurate detection of the onset of

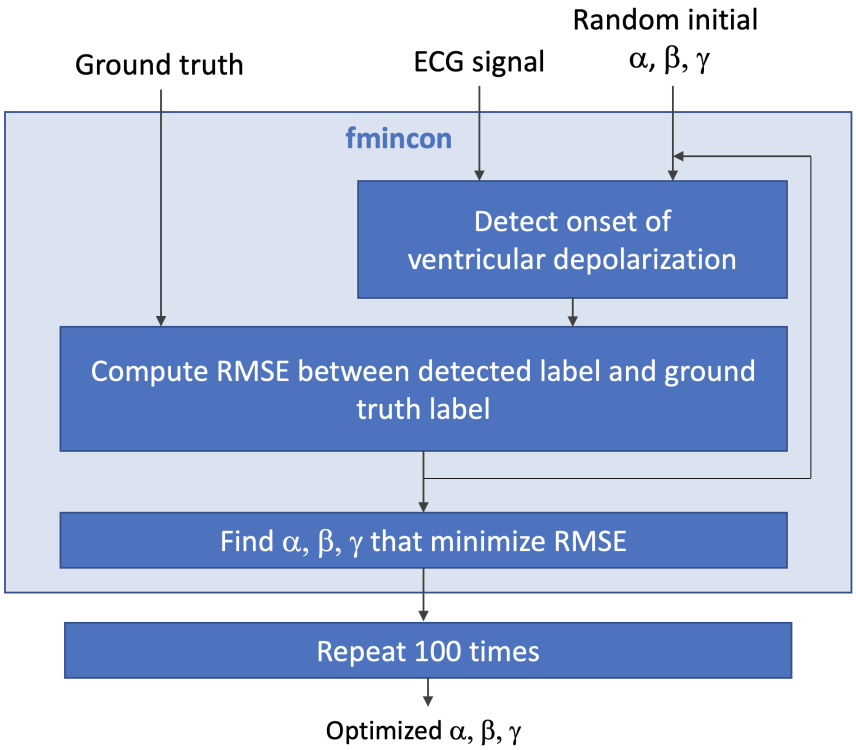

Figure 10.5: Parameter optimization for detection of onset of ventricular depolarization

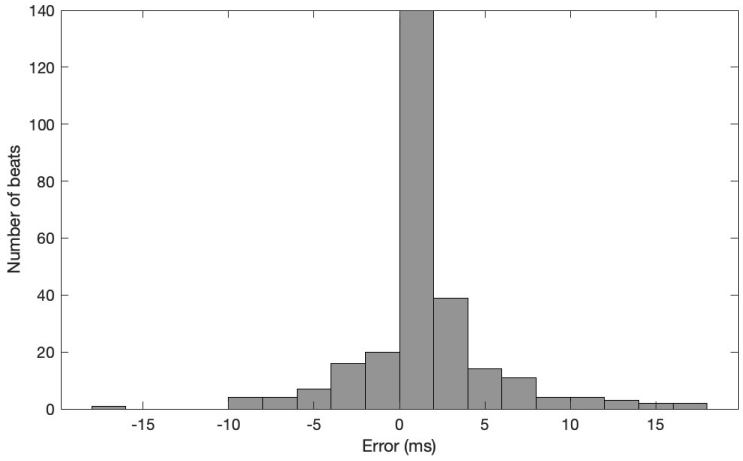

Figure 10.6: Histogram of the errors

each QRS complex in challenging signals with various waveform morphologies and high level of noise. One such example is shown in Figure 10.7. Various QRS complex morphologies and the effectiveness of the combined signal in detecting the first wave are demonstrated in

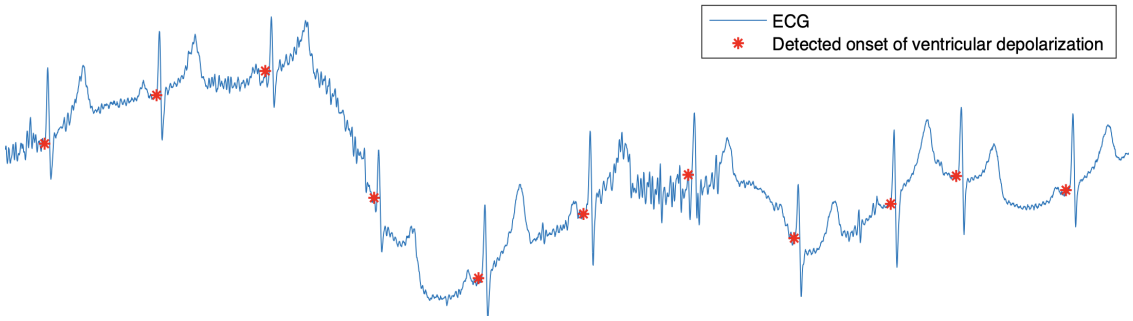

Figure 10.7: Detection of onset of ventricular depolarization in a challenging ECG signal

Figure 10.8. As indicated by the green vertical dashed line in each example, the maximum of the combined signal overlaps with the first wave. The ground truth labels and detected labels are in excellent agreement.

10.2 Detection of Biomechanical Events for Systolic Time Interval

10.2.1 Introduction

Combining with the onset time of ventricular depolarization, STI are computed with the timing of the aortic valve opening and closure events. While ECG is the universal choice of the signal source where the onset of ventricular depolarization is measured, there have been several different methods for detection of the cardiac valve event.

Traditionally, a combination of carotid pulse tracing and PCG has been used for the valve event detection [118][21]. Carotid pulse tracing provides an indirect measurement of the aortic valve opening as the upstroke in the trace correlates with the opening [54]. As discussed earlier, S2 in PCG signals corresponds to aortic and pulmonic valve closures. Because the aortic valve closure normally precedes the pulmonic valve closure, the onset of S2 can be used for the timing of the aortic valve closure. Echocardiography has been also used to measure STI [56][105][89] as it provides more direct measurement of the valve events. Currently, echocardiography in combination with ECG is the gold standard measurement method for STI [106]. However, as discussed earlier, echocardiography requires an expensive

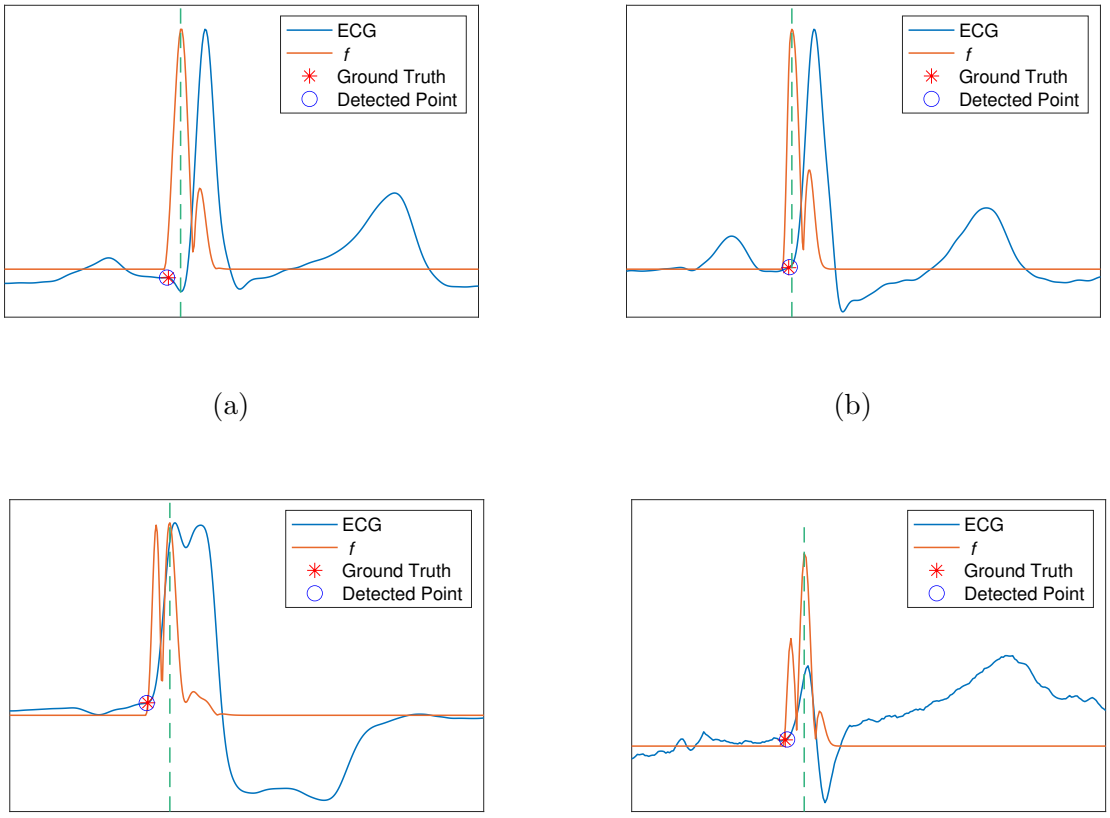

Figure 10.8: Demonstration of the detection algorithm for the onset of ventricular depolarization on signals with various QRS complex morphologies. (a) a QRS complex from a subject with left arteriovenous fistula, hyperlipidemia, and hypertension. (b) an RS complex, i.e. QRS complex without a Q wave, from a subject with acute myocardial infarction, cardiogenic shock, coronary artery disease, and ventricular tachycardia. (c) an RS complex from a subject with a pacemaker, atrioventricular block, bicuspid aortic block, cardiomyopathy, and ventricular septal defect. (d) an RS complex from a signal with heavy baseline wander

equipment and a professionally trained expert. As an alternative method, SCG has been studied for STI measurement [99][65][13]. Simultaneous SCG and echocardiography have demonstrated that valve events including aortic valve opening and closure are reflected in

SCG signals as peaks.

We have explored potentials of PCG in STI computation. The aortic valve opening is generally considered unidentifiable in the conventional PCG as the heart sounds are dominated by the valve closure. Nevertheless, there have been efforts to derive STI from PCG. In [86], a delay between the mitral valve closure and aortic valve opening is assumed and used to estimate the timing of the aortic valve opening following detection of the mitral valve closure. In [23], instantaneous energy and frequency were used to detect the aortic valve opening based on a hypothesis that two high frequency components in S1 correspond to the mitral valve closure and aortic valve opening respectively. In [9], the peak of the envelope signal during S1 is used as a substitute for the aortic valve opening.

Inspired by SCG whose low-frequency characteristics have demonstrated effective STI computation, we have investigated low-frequency PCG to find a feature that can be used to derive STI. In this section, we identify such a feature and compute STI with it in combination with the onset of ventricular depolarization and S2. The computed STI is then evaluated by analyzing its correlation with the EF measured with echocardiography.

10.2.2 Method

Based on our observation, the low-frequency PCG signals from the four sensors tend to exhibit commonly occurring patterns as shown in Figure 10.9. The positive and negative peaks indicated by the vertical dotted lines are some of the common patterns during the S1 and S2. While the magenta lines correspond to the onset of S2 or indirectly aortic valve closure, the features indicated by the other vertical lines are investigated to find the surrogate feature for the aortic valve opening.

The onset of S1 correlates with the mitral valve closure, which precedes the aortic valve opening. We first identify the feature in the low-frequency signal that corresponds to the onset of the S1. Figure 10.10 shows an example that illustrates superimposed waveforms of denoised and bandpass-filtered PCG signals in the audible range and the corresponding low-frequency PCG signals processed from the same raw PCG data. The onset of S1 roughly

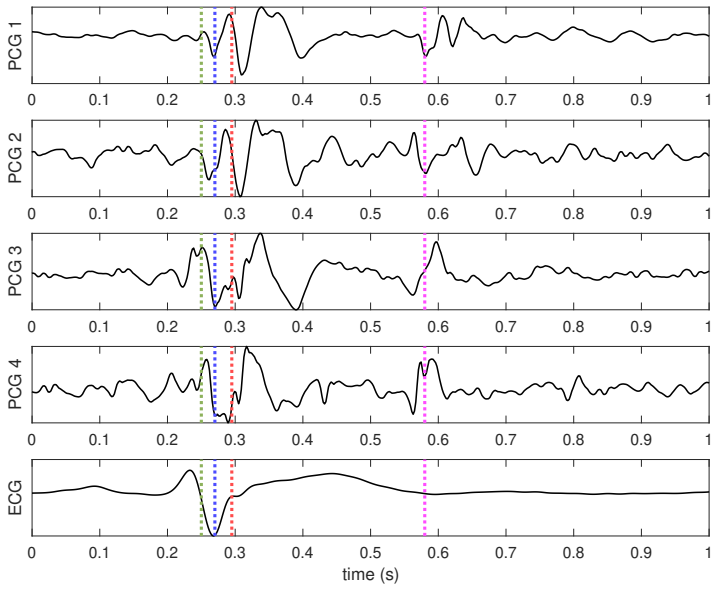

Figure 10.9: Commonly occurring patterns in low-frequency PCG across four sensors

coincides with the first major deflection or point where the slope changes abruptly in the low-frequency PCG signal that commonly appear in most of the PCG sensors as indicated by the green vertical dotted lines in Figure 10.10. From this, we can assume that a surrogate feature for the aortic valve opening must be searched among features after this.

In order to gain more insight on the relative timing of the aortic valve opening within S1, we conducted a brief experiment with four subjects where one of the acoustic sensors is placed on the neck at the carotid artery. The carotid artery pulse begins with the blood flow from the left ventricle into the artery when the aortic valve opens [117]. Thus, simultaneous recording of an acoustic signal on the neck and PCG signals would provide a time reference for the surrogate feature search. The acoustic signal recorded on the neck should not be confused with carotid pulse tracing. Nonetheless, we have observed that the low-frequency vibration on the neck due to carotid pulse can be captured by the acoustic sensor. Figure 10.11 shows examples of simultaneously recorded PCG signal and acoustic signal at the carotid artery. The acoustic signal recorded on the neck is somewhat noisy, and the roughly estimated onset of the pulse should not be used as the ground truth for aortic valve opening. Furthermore, the

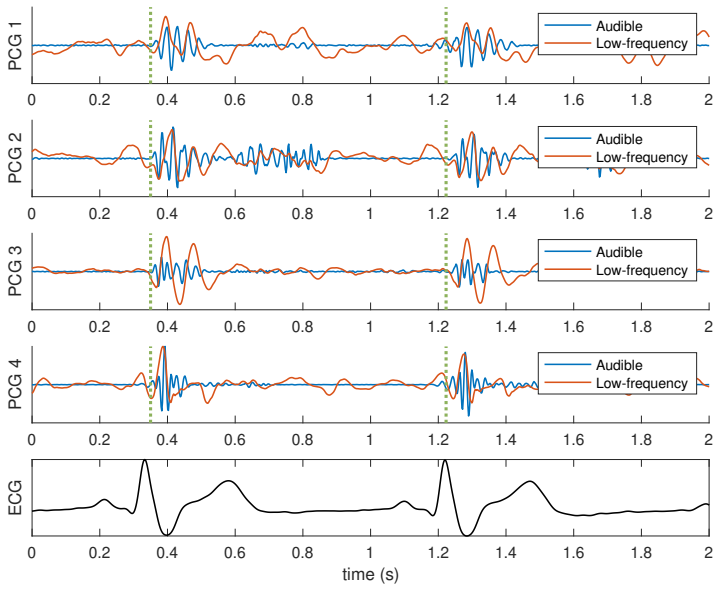

Figure 10.10: Superimposed waveforms of audible and low-frequency components

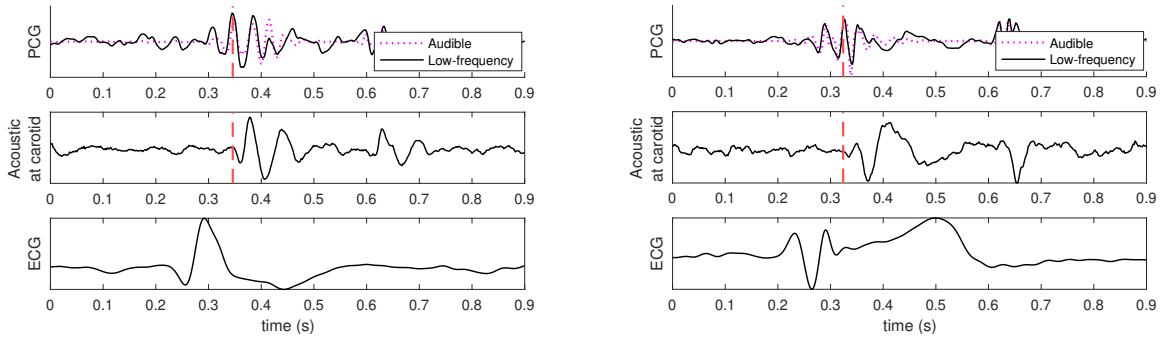

(a) (b)

Figure 10.11: acoustic signal on carotid artery and PCG signal

physiology behind the low-frequency PCG features is not fully understood. However, such rough estimates are observed to roughly coincide with a commonly occurring positive peak feature following the onset of S1. Thus, we have investigated such feature as the surrogate feature for the aortic valve opening.

We have developed a method to detect the first commonly occurring peak following the onset of S1. The proposed method utilizes a flexible weight function similar to that used in

the algorithm for detection of the onset of ventricular depolarization. The weight function includes adjustable parameters that are optimized with annotated data. The low-frequency PCG signals of several subjects from the UCLA trial dataset have been examined, and the surrogate feature for aortic valve opening has been manually annotated.

The detection algorithm for the feature first begins by finding peaks in the low-frequency PCG signals from the four sensors between the onset of ventricular depolarization and end of S1. Subsequently, a Gaussian-shaped curve is generated at each location of the detected peak. The Gaussian-shaped curves allow each peak to have equal contribution to the weight. σ to adjust the width of each curve is a parameter to optimize. A descending ramp function is applied in order to emphasize earlier peaks. The duration of the ramp function is from the onset to the end of the S1. An exponent to the ramp is added as an adjustable parameter that controls the degree of the impact of the ramp function. In summary, the weight function is

$$w(t) = R^{\alpha}(t) \sum_{p_i \in P} e^{-\frac{(t-p_i)^2}{\sigma^2}} \tag{10.2}$$

where P is a set of timing of all detected peaks from all the four per-sensor PCG signals. The parameters α and σ are optimized with fmincon.

As observed in Figure 10.10, peaks from the four per-sensor signals are not perfectly aligned, potentially leading to multiple peaks in the weight function. A lowpass filter is applied to the weight function to merge such close peaks. Subsequently, prominent peaks in the weight function are detected. If time duration between the first prominent peak and the S1 onset is short, it is likely that the peak corresponds to the S1 onset. In this case, the second prominent peak is selected as the surrogate feature for the aortic valve opening. Otherwise, the first prominent peak is selected. Figure 10.12 shows an example of the surrogate feature detected with the weight function.

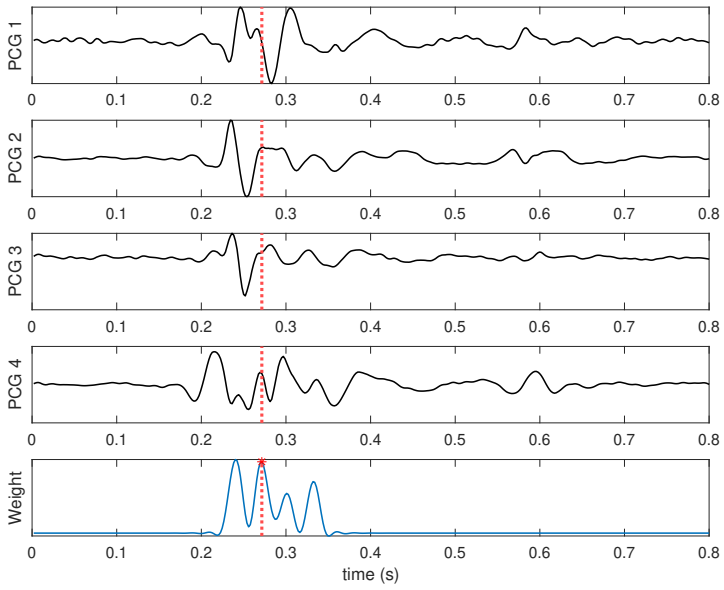

Figure 10.12: Demonstration of weight function for detection of surrogate low-frequency PCG feature

10.2.3 Results

Combined with the detected onset of ventricular depolarization and S2 onset, the detected surrogate feature of the aortic valve opening is used to compute the PEP and LVET for N=50 subjects from the UCLA trial dataset. The subjects have EF ranging from 23% to 80%. For each subject, PEP and LVET values are computed for several consecutive 10-second data. The median values of these are computed as a single PEP and LVET per subject. Subsequently, the PEP/LVET is computed from these median PEP and LVET values per subject.

The method is validated with 5-fold cross validation wherein the parameters for the weight function are re-optimized during each round. The result is illustrated in the scatter plots shown in Figure 10.13. The computed PEP and EF have correlation r of -0.65. The correlation between the LVET and EF is lower at 0.28. PEP/LVET is known have stronger correlation with EF, and our result shows the correlation between the computed PEP/LVET and EF is -0.68.

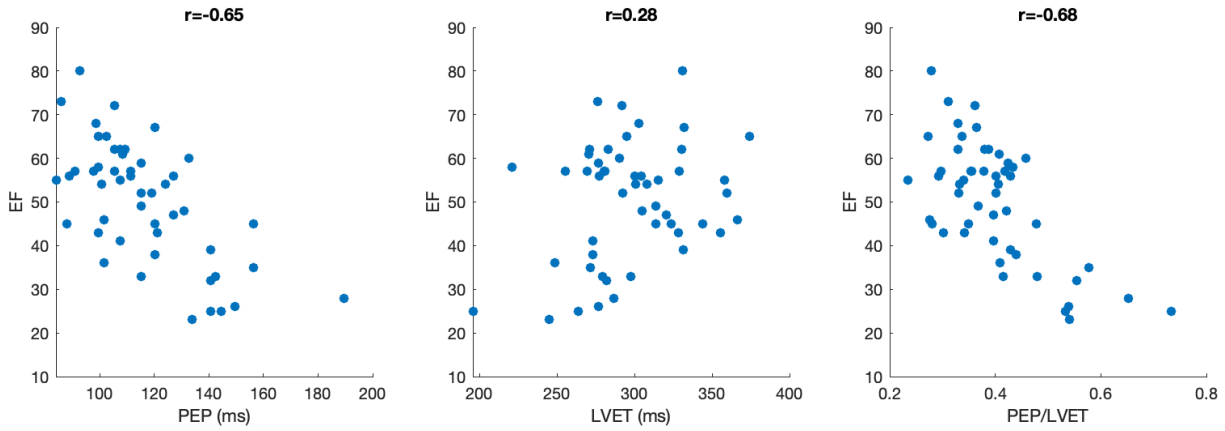

Figure 10.13: PEP, LVET, and PEP/LVET and their correlation with EF (r=-0.65, r=0.28, r=-0.68)

10.3 Summary

In this chapter, we have explored a potential expansion of the system. STI, widely studied non-invasive measurement of EF, are the time intervals between the electrical and mechanical events of the heart. As such, we have investigated STI computation using the already available synchronous ECG and PCG signals.

Data-driven methods have been developed for detection of the events required for STI computation. The electrical event to detect is the onset of ventricular depolarization. We have developed a flexible algorithm that combines factors that are consistent with the onset of ventricular depolarization. The method has been evaluated on a large set of potentially noisy ECG signals with various morphologies. The labels for the onset of ventricular depolarization estimated by the algorithm are compared with the ground truth labels established by a physician, yielding bias, mean absolute error, standard deviation of error of 1.46 ms, 3.16 ms, and 4.73 ms respectively.

The mechanical events required for STI are aortic valve opening and closure. While aortic valve closure can be detected by the onset of S2, its opening is generally not considered observable in the conventional PCG. We have investigated the low-frequency components of PCG signals to find a potential surrogate feature for the aortic valve opening and de-

veloped a detection method for such a surrogate feature by combining low-frequency PCG characteristics that coincide with feature. The STI computed with the onset of ventricular depolarization, S2 onset, and the surrogate feature for aortic valve opening have been evaluated on N=50 subjects whose EF ranges from 23% to 80%. The correlation of the computed PEP, LVET, and PEP/LVET with the EF are -0.65, 0.28, and -0.68 respectively.

CHAPTER 11

Conclusion

HF is a serious condition wherein the heart is unable to supply sufficient amount of blood into circulation to meet the body's demand. HF has been recognized as an emerging epidemic, and its prevalence is still growing. Therefore, an immense need for prevention and treatment of HF has emerged. There are two different types of HF: systolic HF and diastolic HF. The former is due to impaired ventricular contraction while the latter is due to impaired ventricular relaxation. The effectiveness of ventricular relaxation is reflected by the ventricular filling pressure, which is indirectly measured by PCWP. Another critical pressure metric is PAP, the primary indicator of pulmonary hypertension. It has been suggested that elevated PAP is associated with an increased risk of adverse prognosis for HF patients. The current gold standard method for measurement of PCWP and PAP is RHC, which is an invasive procedure and requires expertise. As such, its utility for routine PCWP and PAP monitoring is limited.

We have developed a fully automated system that integrates non-invasive ECG and PCG signals to measure PCWP and mPAP. The system consists of a set of wearable sensors to simultaneously record ECG and PCG signals and a patient monitor that hosts signal processing and machine learning methods to compute the PCWP and mPAP. The non-invasive measurement and fully automated computation enable readily available and safe routine monitoring of PCWP and mPAP.

The signal characteristics are analyzed and extracted as features from which the machine learning methods predict the PCWP and mPAP. To achieve this, cardiac events in the signals must be first identified. As the initial step, the ECG signal is analyzed and its

most prominent feature, QRS complex, is identified. The QRS complex is a highly periodic feature that reflects the ventricular depolarization, making it an ideal reference for heartbeat segmentation. We developed a QRS complex detection algorithm as well as precise heartbeat segmentation based on the low-frequency characteristics of the QRS complex.

Next, the PCG signal is analyzed. We have investigated different frequency bands of PCG signals and observed high periodicity in the low-frequency components. Furthermore, the low-frequency PCG has shown similar waveform morphology to SCG, suggesting its potentials for feature extraction. We have also performed time-frequency analysis of the raw PCG signal.

Minimal level of noise is crucial to accurate computation of PCWP and PAP. The noise suppression for the audible PCG components is performed via an existing spectral subtraction method. As for the low-frequency PCG components, ensemble averaging of several consecutive heartbeat segments is used to suppress noise. The ensemble averaging requires precise alignment of the heartbeat segments. However, heart rate variability may be present, leading to misalignment. Thus, we have investigated DTW methods and developed a robust time alignment method based on cross-correlation to align the segments.

From the processed PCG signals, a set of features that correlate with PCWP or mPAP have been extracted. The considered features are based on amplitude, spectral characteristics, morphology, power, and harmonicity. Then, PCA is applied to reduce dimensionality.

The PCG features are utilized by machine learning algorithms to compute PCWP and mPAP. In order to enhance the accuracy, the algorithms have been designed with a hierarchy of linear models where the top-level model covers the global range of PCWP or mPAP and produces a rough estimate while the lower-level models are trained with subranges to make more accurate and precise prediction. To improve training accuracy, we have developed a 2-stage outlier detection algorithm for outlier removal during training. The system has been validated with trial data by comparing the predicted pressure values with the gold standard RHC values.

Successful operation of the system and accurate prediction of the pressure metrics re-

quire quality signals. The noise reduction method is only effective if the signal strength is sufficient with reasonable amount of noise. Thus, signals with insufficient strength and those that are heavily corrupted by noise must be excluded. We have developed signal quality assurance methods to assess ECG and PCG signal quality. A set of features that correlate with the signal quality have been developed along with SVM-based classifiers. In addition, a periodicity score method has been developed to assess the quality of the low-frequency components of PCG signals. The system can use the computed signal quality to provide user feedback to guide correct application of the sensors as well as automated rejection of signal segments that contain noisy events when computing the pressure metrics.

Finally, we have explored STI as a potential expansion of the system utilizing its synchronous ECG and PCG. To achieve this, we have developed algorithms to detect the onset of ventricular depolarization and a surrogate feature in low-frequency PCG for the aortic valve opening.

There are many opportunities for further system expansion and improvement. In addition to STI, more features can be developed to predict EF and stroke volume, which are other important metrics to assess HF. The patient monitor can be replaced with a lightweight device to make the system completely wearable. This will enable continuous monitoring of a patient's cardiac state not only in a hospital but also at home. Furthermore, a microphone and an accelerometer can be added to monitor the ambient noise level and motion to enable episodic sampling of ECG and PCG signals, making the system more energy-efficient. In combination with the signal quality assurance methods, this will allow the system to compute the metrics only when the noise is minimal. In conclusion, the highly available, safe, and easy-to-use system that accurately predicts important cardiac metrics will have a significant impact on cardiac monitoring.

REFERENCES

[1] EG01000 One Channel ECG Module Datasheet. https://www.medlab.eu/english/modules/ekgmodules/eg01000/index.html, accessed 2021-10-30.

[2] fmincon. https://www.mathworks.com/help/optim/ug/fmincon.html.

[3] Intel Edison Development Platform. https://www.intel.com/content/dam/support/us/en/documents/edison/sb/edison_pb_331179002.pdf, accessed 2021-11-09.

[4] LSM9DS0 Datasheet. https://www.st.com/resource/en/datasheet/lsm9ds0.pdf, accessed 2021-11-09.

[5] Ejection fraction heart failure measurement, May 2017.

[6] Abbas K. Abbas and Rasha Bassam. Phonocardiography signal processing. *Synthesis Lectures on Biomedical Engineering*, 4(1):1–194, 2009.

[7] Philip B. Adamson, William T. Abraham, Robert C. Bourge, Maria Rosa Costanzo, Ayesha Hasan, Chethan Yadav, John Henderson, Pam Cowart, and Lynne Warner Stevenson. Wireless pulmonary artery pressure monitoring guides management to reduce decompensation in heart failure with preserved ejection fraction. *Circulation: Heart Failure*, 7(6):935–944, 2014.

[8] Javier F. Aduen, Ramon Castello, Marcelo M. Lozano, George N. Hepler, Cesar A. Keller, Francisco Alvarez, Robert E. Safford, Julia E. Crook, Michael G. Heckman, and Charles D. Burger. An alternative echocardiographic method to estimate mean pulmonary artery pressure: diagnostic and clinical implications. *Journal of the American Society of Echocardiography*, 22(7):814–819, 2009.

[9] Teemu Ahmaniemi, Satu Rajala, and Harri Lindholm. Estimation of beat-to-beat interval and systolic time intervals using phono- and seismocardiograms. In *2019 41st Annual International Conference of the IEEE Engineering in Medicine and Biology Society (EMBC)*, pages 5650–5656. IEEE, 2019.

[10] Brad G. Angeja and William Grossman. Evaluation and management of diastolic heart failure. *Circulation*, 107(5):659–663, 2003.

[11] P.J. Arnott, G.W. Pfeiffer, and M.E. Tavel. Spectral analysis of heart sounds: relationships between some physical characteristics and frequency spectra of first and second heart sounds in normals and hypertensives. *Journal of Biomedical Engineering*, 6(2):121–128, 1984.

[12] Natalia M. Arzeno, Zhi-De Deng, and Chi-Sang Poon. Analysis of first-derivative based QRS detection algorithms. *IEEE Transactions on Biomedical Engineering*, 55(2):478–484, 2008.

[13] Hazar Ashouri, Sinan Hersek, and Omer T. Inan. Universal pre-ejection period estimation using seismocardiography: Quantifying the effects of sensor placement and regression algorithms. *IEEE Sensors Journal*, 18(4):1665–1674, 2017.

[14] Sumair Aziz, Muhammad Umar Khan, Majed Alhaisoni, Tallha Akram, and Muhammad Altaf. Phonocardiogram signal processing for automatic diagnosis of congenital heart disorders through fusion of temporal and cepstral features. *Sensors*, 20(13):3790, 2020.

[15] Wajid Aziz and Muhammad Arif. Complexity analysis of stride interval time series by threshold dependent symbolic entropy. *European Journal of Applied Physiology*, 98(1):30–40, 2006.

[16] Christopher Baek, Kanav Saraf, Michael Wasko, Xu Zhang, Yi Zheng, Per Borgstrom, Aman Mahajan, and William Kaiser. Automated detection of the onset of ventricular depolarization in challenging clinical ECG data. In *2019 IEEE/ACM International Conference on Connected Health: Applications, Systems and Engineering Technologies (CHASE)*, pages 9–10. IEEE, 2019.

[17] Neeraj Baghel, Malay Kishore Dutta, and Radim Burget. Automatic diagnosis of multiple cardiac diseases from PCG signals using convolutional neural network. *Computer Methods and Programs in Biomedicine*, 197:105750, 2020.

[18] H.L. Baranek, H.C. Lee, G. Cloutier, and L.-G. Durand. Automatic detection of sounds and murmurs in patients with lonescu-Shiley aortic bioprostheses. *Medical and Biological Engineering and Computing*, 27(5):449–455, 1989.

[19] J. Martin Bland and Douglas G. Altman. Statistical methods for assessing agreement between two methods of clinical measurement. *The Lancet*, 327(8476):307–310, 1986.

[20] Nils Peter Borgstrom. *The Integrated CardioRespiratory Heart Function Monitoring System*. PhD thesis, UCLA, 2017.

[21] H. Boudoulas. Systolic time intervals. *European Heart Journal*, 11(suppl_I):93–104, 1990.

[22] Matteo Cameli, Matteo Lisi, Sergio Mondillo, Margherita Padeletti, Piercarlo Ballo, Charilaos Tsioulpas, Sonia Bernazzali, and Massimo Maccherini. Left atrial longitudinal strain by speckle tracking echocardiography correlates well with left ventricular filling pressures in patients with heart failure. *Cardiovascular Ultrasound*, 8(1):1–9, 2010.

[23] P. Carvalho, R. P. Paiva, R. Couceiro, J. Henriques, I. Quintal, J. Muehlsteff, X. L. Aubert, and M. Antunes. Assessing systolic time-intervals from heart sound: a feasibility study. In *2009 Annual International Conference of the IEEE Engineering in Medicine and Biology Society*, pages 3124–3128. IEEE, 2009.

[24] Fabián Andrés Castaño, Alher Mauricio Hernández, and Georges Soto-Romero. Assessment of artifacts reduction and denoising techniques in electrocardiographic signals using ensemble average-based method. *Computer Methods and Programs in Biomedicine*, 182:105034, 2019.

[25] Paolo Castiglioni, Andrea Faini, Gianfranco Parati, and Marco Di Rienzo. Wearable seismocardiography. In *2007 29th Annual International Conference of the IEEE Engineering in Medicine and Biology Society*, pages 3954–3957. IEEE, 2007.

[26] Hunter C. Champion, Evangelos D. Michelakis, and Paul M. Hassoun. Comprehensive invasive and noninvasive approach to the right ventricle–pulmonary circulation unit: state of the art and clinical and research implications. *Circulation*, 120(11):992–1007, 2009.

[27] Samprit Chatterjee and Ali S. Hadi. Influential observations, high leverage points, and outliers in linear regression. *Statistical Science*, pages 379–393, 1986.

[28] G. D. Clifford, J. Behar, Q. Li, and Iead Rezek. Signal quality indices and data fusion for determining clinical acceptability of electrocardiograms. *Physiological Measurement*, 33(9):1419, 2012.

[29] Richard S. Crow, Peter Hannan, David Jacobs, Lowell Hedquist, and David M. Salerno. Relationship between seismocardiogram and echocardiogram for events in the cardiac cycle. *American Journal of Noninvasive Cardiology*, 8:39–46, 1994.

[30] Michele D'Alto, Emanuele Romeo, Paola Argiento, Antonello D'Andrea, Rebecca Vanderpool, Anna Correra, Eduardo Bossone, Berardo Sarubbi, Raffaele Calabrò, Maria Giovanna Russo, et al. Accuracy and precision of echocardiography versus right heart catheterization for the assessment of pulmonary hypertension. *International Journal of Cardiology*, 168(4):4058–4062, 2013.

[31] Erik de Lima Andrade, Darllan Collins da Cunha e Silva, Eligelcy Augusta de Lima, Renan Angrizani de Oliveira, Paulo Henrique Trombetta Zannin, and Antônio Cesar Germano Martins. Environmental noise in hospitals: a systematic review. *Environmental Science and Pollution Research*, pages 1–14, 2021.

[32] Roy De Maesschalck, Delphine Jouan-Rimbaud, and Désiré L Massart. The Mahalanobis distance. *Chemometrics and Intelligent Laboratory Systems*, 50(1):1–18, 2000.

[33] S.M. Debbal and Fethi Bereksi-Reguig. Time-frequency analysis of the first and the second heartbeat sounds. *Applied Mathematics and Computation*, 184(2):1041–1052, 2007.

[34] M. Danida Deborah, J. Prasad, A. Aamina, and A. Renuga Devi. Phonocardiogram signal processing using LMS adaptive algorithm. *International Journal of Multidisciplinary Approach and Studies*, 3(2):66–73, 2016.

[35] Naveen Dewangan and R.M. Potdar. Noise cancellation using adaptive filter for PCG signal. *International Journal of Emerging Trends Technology in Computer Science*, 3(4), 2014.

[36] Luigi Yuri Di Marco, Wenfeng Duan, Marjan Bojarnejad, Dingchang Zheng, Susan King, Alan Murray, and Philip Langley. Evaluation of an algorithm based on single-condition decision rules for binary classification of 12-lead ambulatory ECG recording quality. *Physiological Measurement*, 33(9):1435, 2012.

[37] Thomas G. Dietterich and Ghulum Bakiri. Solving multiclass learning problems via error-correcting output codes. *Journal of Artificial Intelligence Research*, 2:263–286, 1994.

[38] Ashok Kumar Dohare, Vinod Kumar, and Ritesh Kumar. An efficient new method for the detection of QRS in electrocardiogram. *Computers & Electrical Engineering*, 40(5):1717–1730, 2014.

[39] Barbara J. Drew, Robert M. Califf, Marjorie Funk, Elizabeth S. Kaufman, Mitchell W. Krucoff, Michael M. Laks, Peter W. Macfarlane, Claire Sommargren, Steven Swiryn, and George F. Van Hare. Practice standards for electrocardiographic monitoring in hospital settings: an american heart association scientific statement from the councils on cardiovascular nursing, clinical cardiology, and cardiovascular disease in the young: endorsed by the International Society of Computerized Electrocardiology and the American Association of Critical-Care Nurses. *Circulation*, 110(17):2721–2746, 2004.

[40] James Dugundji. Envelopes and pre-envelopes of real waveforms. *IRE Transactions on Information Theory*, 4(1):53–57, 1958.

[41] E. E. Eddleman Jr, Roy H. Swatzell Jr, William H. Bancroft Jr, James C. Baldone Jr, and Marjorie S. Tucker. The use of the systolic time intervals for predicting left ventricular ejection fraction in ischemic heart disease. *American Heart Journal*, 93(4):450–454, 1977.

[42] Babatunde S. Emmanuel. Discrete wavelet mathematical transformation method for non-stationary heart sounds signal analysis. *ARPN Journal of Engineering and Applied Sciences*, 7(8):1–8, 2012.

[43] Mozziyar Etemadi, Omer T. Inan, J. Alex Heller, Sinan Hersek, Liviu Klein, and Shuvo Roy. A wearable patch to enable long-term monitoring of environmental, activity and hemodynamics variables. *IEEE Transactions on Biomedical Circuits and Systems*, 10(2):280–288, 2015.

[44] Gary M. Friesen, Thomas C. Jannett, Manal Afify Jadallah, Stanford L. Yates, Stephen R. Quint, and H. Troy Nagle. A comparison of the noise sensitivity of nine QRS detection algorithms. *IEEE Transactions on Biomedical Engineering*, 37(1):85–98, 1990.

[45] Girish Gautam and Deepesh Kumar. Biometric system from heart sound using wavelet based feature set. In *2013 International Conference on Communication and Signal Processing*, pages 551–555. IEEE, 2013.

[46] Tomasz Górecki and Maciej Łuczak. Multivariate time series classification with parametric derivative dynamic time warping. *Expert Systems with Applications*, 42(5):2305–2312, 2015.

[47] Dawid Gradolewski and Grzegorz Redlarski. Wavelet-based denoising method for real phonocardiography signal recorded by mobile devices in noisy environment. *Computers in Biology and Medicine*, 52:119–129, 2014.

[48] Amy Groenewegen, Frans H. Rutten, Arend Mosterd, and Arno W. Hoes. Epidemiology of heart failure. *European Journal of Heart Failure*, 22(8):1342–1356, 2020.

[49] Zhenhua Guo, Lei Zhang, and David Zhang. A completed modeling of local binary pattern operator for texture classification. *IEEE Transactions on Image Processing*, 19(6):1657–1663, 2010.

[50] Cecilia Gutierrez and Daniel G. Blanchard. Diastolic heart failure: The challenges of diagnosis and treatment. *American Family Physician*, 69(11):2609–2616, 2004.

[51] SaifEddine Hadji, Mazleena Salleh, MohdFoad Rohani, and Maznah Kamat. Wavelet-based performance in denoising ECG signal. In *Proceedings of the 8th International Conference on Signal Processing Systems*, pages 148–153, 2016.

[52] Patrick S. Hamilton and Willis J. Tompkins. Quantitative investigation of QRS detection rules using the MIT/BIH Arrhythmia Database. *IEEE Transactions on Biomedical Engineering*, BME-33(12):1157–1165, 1986.

[53] Dieter Hayn, Bernhard Jammerbund, and Günter Schreier. QRS detection based ECG quality assessment. *Physiological Measurement*, 33(9):1449, 2012.

[54] Lars Hegrenaes. Left ventricular systolic time intervals. A comparison between the conventional carotid pulse curve method and the Doppler ultrasound method. *European Heart Journal*, 4(5):313–319, 1983.

[55] Paul A. Heidenreich, Nancy M. Albert, Larry A. Allen, David A. Bluemke, Javed Butler, Gregg C. Fonarow, John S. Ikonomidis, Olga Khavjou, Marvin A. Konstam, Thomas M. Maddox, et al. Forecasting the impact of heart failure in the United States: a policy statement from the American Heart Association. *Circulation: Heart Failure*, 6(3):606–619, 2013.

[56] Stephen Hirschfeld, Richard Meyer, David C. Schwartz, Joan Korfhagen, and Samuel Kaplan. Measurement of right and left ventricular systolic time intervals by echocardiography. *Circulation*, 51(2):304–309, 1975.

[57] Victoria Hodge and Jim Austin. A survey of outlier detection methodologies. *Artificial Intelligence Review*, 22(2):85–126, 2004.

[58] Arthur E. Hoerl and Robert W. Kennard. Ridge regression: Biased estimation for nonorthogonal problems. *Technometrics*, 12(1):55–67, 1970.

[59] Leo G. Horan, Nancy C. Flowers, and Jennifer C. Johnson. Significance of the diagnostic Q wave of myocardial infarction. *Circulation*, 43(3):428–436, 1971.

[60] Andreas P. Kalogeropoulos, Sarawut Siwamogsatham, Salim Hayek, Song Li, Anjan Deka, Catherine N. Marti, Vasiliki V. Georgiopoulou, and Javed Butler. Echocardiographic assessment of pulmonary artery systolic pressure and outcomes in ambulatory heart failure patients. *Journal of the American Heart Association*, 3(1):e000363, 2014.

[61] Bernard Karnath and William Thornton. Auscultation of the heart. *Hospital Physician*, 38(9):39–45, 2002.

[62] James M. Kates. Principles of digital dynamic-range compression. *Trends in Amplification*, 9(2):45–76, 2005.

[63] Yoshiaki Kawase, Masanori Kawasaki, Ryuhei Tanaka, Nozomi Nomura, Yoshie Fujii, Keiko Ogawa, Hidemaro Sato, Taiji Miyake, Takayoshi Kato, Tomohiro Tsunekawa, et al. Noninvasive estimation of pulmonary capillary wedge pressure in patients with mitral regurgitation: a speckle tracking echocardiography study. *Journal of Cardiology*, 67(2):192–198, 2016.

[64] Eamonn J. Keogh and Michael J. Pazzani. Derivative dynamic time warping. In *Proceedings of the 2001 SIAM International Conference on Data Mining*, pages 1–11. SIAM, 2001.

[65] Farzad Khosrow-Khavar, Kouhyar Tavakolian, Andrew Blaber, and Carlo Menon. Automatic and robust delineation of the fiducial points of the seismocardiogram signal for noninvasive estimation of cardiac time intervals. *IEEE Transactions on Biomedical Engineering*, 64(8):1701–1710, 2016.

[66] Hyoung-Gook Kim, Nicolas Moreau, and Thomas Sikora. *MPEG-7 audio and beyond: Audio content indexing and retrieval*. John Wiley & Sons, 2006.

[67] Gabor Kovacs, Alexander Avian, Michael Pienn, Robert Naeije, and Horst Olschewski. Reading pulmonary vascular pressure tracings. how to handle the problems of zero leveling and respiratory swings. *American Journal of Respiratory and Critical Care Medicine*, 190(3):252–257, 2014.

[68] Jakub Kužílek, Michal Huptych, Václav Chudáček, Jiří Spilka, and Lenka Lhotská. Data driven approach to ECG signal quality assessment using multistep SVM classification. In *2011 Computing in Cardiology*, pages 453–455. IEEE, 2011.

[69] Rida Laeeq, Mark Pollet, Nadeen Faza, and Yochai Birnbaum. Varying morphology of QRS complexes: A possible explanation. *Texas Heart Institute Journal*, 44(6):429–430, 2017.

[70] Abraham Lempel and Jacob Ziv. On the complexity of finite sequences. *IEEE Transactions on information theory*, 22(1):75–81, 1976.

[71] Qiao Li, Cadathur Rajagopalan, and Gari D. Clifford. A machine learning approach to multi-level ECG signal quality classification. *Computer Methods and Programs in Biomedicine*, 117(3):435–447, 2014.

[72] Hrishikesh Limaye and V. V. Deshmukh. ECG noise sources and various noise removal techniques: a survey. *International Journal of Application or Innovation in Engineering & Management*, 5(2):86–92, 2016.

[73] David J. Lin, Jacob P. Kimball, Jonathan Zia, Venu G. Ganti, and Omer T. Inan. Reducing the impact of external vibrations on fiducial point detection in seismocardiogram signals. *IEEE Transactions on Biomedical Engineering*, 69(1):176–185, 2021.

[74] Aldo A. Luisada. The expanding horizon of phonocardiography. *Archiv für Kreislaufforschung*, 33(1):38–62, 1960.

[75] M. Sabarimalai Manikandan and K.P. Soman. A novel method for detecting R-peaks in electrocardiogram (ECG) signal. *Biomedical Signal Processing and Control*, 7(2):118–128, 2012.

[76] Jan H. Meijer, Sanne Boesveldt, Eskeline Elbertse, and H. W. Berendse. Method to measure autonomic control of cardiac function using time interval parameters from impedance cardiography. *Physiological Measurement*, 29(6):S383, 2008.

[77] Sheila R. Messer, John Agzarian, and Derek Abbott. Optimal wavelet denoising for phonocardiograms. *Microelectronics Journal*, 32(12):931–941, 2001.

[78] David L. Mills. Internet time synchronization: the network time protocol. *IEEE Transactions on Communications*, 39(10):1482–1493, 1991.

[79] George B. Moody and Roger G. Mark. The impact of the MIT-BIH Arrhythmia Database. *IEEE Engineering in Medicine and Biology Magazine*, 20(3):45–50, 2001.

[80] Arend Mosterd and Arno W. Hoes. Clinical epidemiology of heart failure. *heart*, 93(9):1137–1146, 2007.

[81] Sherif F. Nagueh, Katherine J. Middleton, Helen A. Kopelen, William A. Zoghbi, and Miguel A. Quiñones. Doppler tissue imaging: a noninvasive technique for evaluation of left ventricular relaxation and estimation of filling pressures. *Journal of the American College of Cardiology*, 30(6):1527–1533, 1997.

[82] Amir-Homayoon Najmi and John Sadowsky. The continuous wavelet transform and variable resolution time-frequency analysis. *Johns Hopkins APL Technical Digest*, 18(1):134–140, 1997.

[83] David J. Olive. A resistant estimator of multivariate location and dispersion. *Computational Statistics & Data Analysis*, 46(1):93–102, 2004.

[84] Christina Orphanidou, Timothy Bonnici, Peter Charlton, David Clifton, David Vallance, and Lionel Tarassenko. Signal-quality indices for the electrocardiogram and photoplethysmogram: Derivation and applications to wireless monitoring. *IEEE Journal of Biomedical and Health Informatics*, 19(3):832–838, 2014.

[85] Christina Orphanidou and Ivana Drobnjak. Quality assessment of ambulatory ECG using wavelet entropy of the HRV signal. *IEEE Journal of Biomedical and Health Informatics*, 21(5):1216–1223, 2016.

[86] R. P. Paiva, P. Carvalho, R. Couceiro, J. Henriques, M. Antunes, I. Quintal, and J. Muehlsteff. Beat-to-beat systolic time-interval measurement from heart sounds and ECG. *Physiological Measurement*, 33(2):177, 2012.

[87] Anindya S. Paul, Eric A. Wan, and Alex T. Nelson. Noise reduction for heart sounds using a modified minimum-mean squared error estimator with ECG gating. In *2006 International Conference of the IEEE Engineering in Medicine and Biology Society*, pages 3385–3390. IEEE, 2006.

[88] J.-J. Perrenoud. Q waves and QS complexes. *European Geriatric Medicine*, 1(6):360–368, 2010.

[89] Patricia Reant, Marina Dijos, Erwan Donal, Aude Mignot, Philippe Ritter, Pierre Bordachar, Pierre Dos Santos, Christophe Leclercq, Raymond Roudaut, Gilbert Habib, et al. Systolic time intervals as simple echocardiographic parameters of left ventricular systolic performance: correlation with ejection fraction and longitudinal two-dimensional strain. *European Journal of Echocardiography*, 11(10):834–844, 2010.

[90] Leslie Michael Rosa and Aldo A. Luisada. Low frequency tracings of precordial displacement and acceleration: Technical comparison of various systems. *The American Journal of Cardiology*, 4(5):669–674, 1959.

[91] Stephan Rosenkranz and Ioana R. Preston. Right heart catheterisation: best practice and pitfalls in pulmonary hypertension. *European Respiratory Review*, 24(138):642–652, 2015.

[92] Peter J. Rousseeuw. Least median of squares regression. *Journal of the American Statistical Association*, 79(388):871–880, 1984.

[93] Tsuguya Sakamoto, Reizo Kusukawa, Donald M. MacCanon, Aldo A. Luisada, and Ivan Harvey. Hemodynamic determinants of the amplitude of the first heart sound. *Circulation Research*, 16(1):45–57, 1965.

[94] Hiroaki Sakoe and Seibi Chiba. Dynamic programming algorithm optimization for spoken word recognition. *IEEE Transactions on Acoustics, Speech, and Signal Processing*, 26(1):43–49, 1978.

[95] Kanav Saraf, Christopher I. Baek, Michael H. Wasko, Xu Zhang, Yi Zheng, Per H. Borgstrom, Aman Mahajan, and William J. Kaiser. Fully-automated diagnosis of aortic stenosis using phonocardiogram-based features. In *2019 41st Annual International Conference of the IEEE Engineering in Medicine and Biology Society (EMBC)*, pages 6673–6676. IEEE, 2019.

[96] Udit Satija, Barathram Ramkumar, and M. Sabarimalai Manikandan. An automated ECG signal quality assessment method for unsupervised diagnostic systems. *Biocybernetics and Biomedical Engineering*, 38(1):54–70, 2018.

[97] Samuel E. Schmidt, Claus Holst-Hansen, John Hansen, Egon Toft, and Johannes J. Struijk. Acoustic features for the identification of coronary artery disease. *IEEE Transactions on Biomedical Engineering*, 62(11):2611–2619, 2015.

[98] Pranab Kumar Sen. Estimates of the regression coefficient based on Kendall's tau. *Journal of the American Statistical Association*, 63(324):1379–1389, 1968.

[99] Ghufran Shafiq, Sivanagaraja Tatinati, and Kalyana C. Veluvolu. Automatic annotation of peaks in seismocardiogram for systolic time intervals. In *2016 38th Annual International Conference of the IEEE Engineering in Medicine and Biology Society (EMBC)*, pages 2672–2675. IEEE, 2016.

[100] P.M. Shah, M. Mori, D.M. MacCanon, and A.A. Luisada. Hemodynamic correlates of the various components of the first heart sound. *Circulation Research*, 12(4):386–392, 1963.

[101] Stephen Sidney, Alan S. Go, Marc G. Jaffe, Matthew D. Solomon, Andrew P. Ambrosy, and Jamal S. Rana. Association between aging of the US population and heart disease mortality from 2011 to 2017. *JAMA Cardiology*, 4(12):1280–1286, 2019.

[102] M. Sifuzzaman, M. Rafiq Islam, and M.Z. Ali. Application of wavelet transform and its advantages compared to Fourier transform. *Journal of Physical Science*, 13:121–134, 2009.

[103] Michael P. Somers, William J. Brady, Andrew D. Perron, and Amal Mattu. The prominant T wave: electrocardiographic differential diagnosis. *The American Journal of Emergency Medicine*, 20(3):243–251, 2002.

[104] Gui-Young Son, Soonil Kwon, et al. Classification of heart sound signal using multiple features. *Applied Sciences*, 8(12):2344, 2018.

[105] Miltiadis A. Stefadouros and A. Calhoun Witham. Systolic time intervals by echocardiography. *Circulation*, 51(1):114–117, 1975.

[106] Kouhyar Tavakolian. Systolic time intervals and new measurement methods. *Cardiovascular Engineering and Technology*, 7(2):118–125, 2016.

[107] Kouhyar Tavakolian, Andrew P. Blaber, Brandon Ngai, and Bozena Kaminska. Estimation of hemodynamic parameters from seismocardiogram. In *2010 Computing in Cardiology*, pages 1055–1058. IEEE, 2010.

[108] Kouhyar Tavakolian, Gonzalo Portacio, Niloufar R. Tamddondoust, Graeme Jahns, Brandon Ngai, Guy A. Dumont, and Andrew P. Blaber. Myocardial contractility: A seismocardiography approach. In *2012 Annual International Conference of the IEEE Engineering in Medicine and Biology Society*, pages 3801–3804. IEEE, 2012.

[109] Morton E. Tavel. Cardiac auscultation: a glorious past—but does it have a future? *Circulation*, 93(6):1250–1253, 1996.

[110] Morton E. Tavel and Hart Katz. Usefulness of a new sound spectral averaging technique to distinguish an innocent systolic murmur from that of aortic stenosis. *The American Journal of Cardiology*, 95(7):902–904, 2005.

[111] Nitish V. Thakor, John G. Webster, and Willis J. Tompkins. Estimation of QRS complex power spectra for design of a QRS filter. *IEEE Transactions on Biomedical Engineering*, (11):702–706, 1984.

[112] Henri Theil. A rank-invariant method of linear and polynomial regression analysis. *Indagationes Mathematicae*, 12(85):173, 1950.

[113] Robert Tibshirani. Regression shrinkage and selection via the lasso. *Journal of the Royal Statistical Society: Series B (Methodological)*, 58(1):267–288, 1996.

[114] Navneet Upadhyay and Abhijit Karmakar. Speech enhancement using spectral subtraction-type algorithms: A comparison and simulation study. *Procedia Computer Science*, 54:574–584, 2015.

[115] Salim S. Virani, Alvaro Alonso, Emelia J. Benjamin, Marcio S. Bittencourt, Clifton W. Callaway, April P. Carson, Alanna M. Chamberlain, Alexander R. Chang, Susan Cheng, Francesca N. Delling, Luc Djousse, Mitchell S.V. Elkind, Jane F. Ferguson, Myriam Fornage, Sadiya S. Khan, Brett M. Kissela, Kristen L. Knutson, Tak W. Kwan, Daniel T. Lackland, Tené T. Lewis, Judith H. Lichtman, Chris T. Longenecker, Matthew Shane Loop, Pamela L. Lutsey, Seth S. Martin, Kunihiro Matsushita, Andrew E. Moran, Michael E. Mussolino, Amanda Marma Perak, Wayne D. Rosamond, Gregory A. Roth, Uchechukwu K.A. Sampson, Gary M. Satou, Emily B. Schroeder, Svati H. Shah, Christina M. Shay, Nicole L. Spartano, Andrew Stokes, David L. Tirschwell, Lisa B. VanWagner, Connie W. Tsao, American Heart Association Council on Epidemiology, Prevention Statistics Committee, and Stroke Statistics Subcommittee. Heart disease and stroke statistics-2020 update: A report from the American Heart Association. *Circulation*, 141(9):e139–e596, 2020.

[116] Andreas Voss, Andrea Mix, and Thomas Hübner. Diagnosing aortic valve stenosis by parameter extraction of heart sound signals. *Annals of Biomedical Engineering*, 33(9):1167–1174, 2005.

[117] H. Kenneth Walker, W. Dallas Hall, and J. Willis Hurst. Clinical methods: the history, physical, and laboratory examinations. 1990.

[118] Arnold M. Weissler, Willard S. Harris, and Clyde D. Schoenfeld. Systolic time intervals in heart failure in man. *Circulation*, 37(2):149–159, 1968.

[119] Heather Woltman, Andrea Feldstain, J. Christine MacKay, and Meredith Rocchi. An introduction to hierarchical linear modeling. *Tutorials in Quantitative Methods for Psychology*, 8(1):52–69, 2012.

[120] Yun-Chi Yeh and Wen-June Wang. QRS complexes detection for ECG signal: The difference operation method. *Computer Methods and Programs in Biomedicine*, 91(3):245–254, 2008.

[121] John M. Zanetti and David M. Salerno. Seismocardiography: a technique for recording precordial acceleration. In *Computer-Based Medical Systems-Proceedings of the Fourth Annual IEEE Symposium*, pages 4–5. IEEE Computer Society, 1991.

[122] John M. Zanetti and Kouhyar Tavakolian. Seismocardiography: Past, present and future. In *2013 35th Annual International Conference of the IEEE Engineering in Medicine and Biology Society (EMBC)*, pages 7004–7007. IEEE, 2013.

[123] Qifei Zhang, Lingjian Fu, and Linyue Gu. A cascaded convolutional neural network for assessing signal quality of dynamic ECG. *Computational and Mathematical Methods in Medicine*, 2019, 2019.

[124] Yatao Zhang, Shoushui Wei, Costanzo Di Maria, and Chengyu Liu. Using Lempel-Ziv complexity to assess ECG signal quality. *Journal of Medical and Biological Engineering*, 36(5):625–634, 2016.

[125] Yatao Zhang, Shoushui Wei, Yutao Long, and Chengyu Liu. Performance analysis of multiscale entropy for the assessment of ECG signal quality. *Journal of Electrical and Computer Engineering*, 2015, 2015.

[126] Zahia Zidelmal, Ahmed Amirou, D. Ould-Abdeslam, Ali Moukadem, and Alain Dieterlen. QRS detection using S-transform and Shannon energy. *Computer Methods and Programs in Biomedicine*, 116(1):1–9, 2014.

[127] Zamri Mohd Zin, Sheikh Hussain Salleh, Shaparas Daliman, and M. Daud Sulaiman. Analysis of heart sounds based on continuous wavelet transform. In *Proceedings. Student Conference on Research and Development, 2003. SCORED 2003.*, pages 19–22. IEEE, 2003.